



**UNIVERSIDADE FEDERAL DO CEARÁ
CENTRO DE CIÊNCIAS
DEPARTAMENTO DE QUÍMICA ANALÍTICA E FÍSICO-QUÍMICA
PROGRAMA DE PÓS-GRADUAÇÃO EM QUÍMICA**

DAVINO MACHADO ANDRADE NETO

**MAGNETIC RESSONANCE IMAGING CONTRAST AGENTS OBTAINED BY FAST
SONOCHEMISTRY APPROACH**

FORTALEZA

2016

DAVINO MACHADO ANDRADE NETO

MAGNETIC RESSONANCE IMAGING CONTRAST AGENTS OBTAINED BY FAST
SONOCHEMISTRY APPROACH

Dissertação apresentada ao Programa de Pós-Graduação em Química da Universidade Federal do Ceará, como requisito parcial à obtenção do título de mestre em química. Área de concentração: química.

Orientador: Prof. Dr. Pierre Basílio Almeida Fachine.

FORTALEZA

2016

Dados Internacionais de Catalogação na Publicação
Universidade Federal do Ceará
Biblioteca Universitária
Gerada automaticamente pelo módulo Catalog, mediante os dados fornecidos pelo(a) autor(a)

A566m Andrade Neto, Davino Machado.

Magnetic resonance imaging contrast agents obtained by fast sonochemistry approach / Davino Machado Andrade Neto. – 2016.
84 f. : il. color.

Dissertação (mestrado) – Universidade Federal do Ceará, Centro de Ciências, Programa de Pós-Graduação em Química, Fortaleza, 2016.

Orientação: Prof. Dr. Pierre Basílio Almeida Fechine.

1. Sonochemistry. 2. Magnetic nanoparticles. 3. Functionalization of nanomaterials. 4. Magnetic resonance imaging. I. Título.

CDD 540


Esta Dissertação foi aprovada como parte dos requisitos necessários à obtenção do Grau de Mestre em Química, área de concentração química, outorgada pela Universidade Federal do Ceará, em cuja Biblioteca de Ciências e Tecnologia/UFC encontra-se à disposição dos interessados.




Davino Machado Andrade Neto

DISSERTAÇÃO APROVADA EM: 18/02/2016.

EXAMINADORES:



Prof. Dr. Pierre Basilio Almeida Fachine,
Universidade Federal do Ceará – UFC



Prof. Dr. Amauri Jardim de Paula
Universidade Federal do Ceará – UFC



Prof. Dr. Igor Frota de Vasconcelos
Universidade Federal do Ceará – UFC

A todas as pessoas que me ajudaram a
construir esse trabalho.

AGRADECIMENTOS

À Capes, pelo apoio financeiro com a manutenção da bolsa.

À Universidade Federal do Ceará pela infraestrutura oferecida para que o trabalho fosse realizado.

Aos membros participantes da Banca examinadora, Profs. Amauri Jardim e Igor Frota.

A todos os professores que contribuíram para a minha formação profissional desde a graduação. Destaque à professora Izaura Cirino, Ronaldo Nascimento, Francisco Belmino, Nágila Ricardo, Nádja Ricardo e Otília Deusdênio.

À professora Selma Mazzeto por todo o apoio que foi dado, principalmente nos momentos de maior dificuldade e necessidade.

A meu amigo Wanderson Moreira, pelas análises termogravimetria.

Ao Laboratório de Raios-X da UFC pelas análises de difração de raio-X. Agradecimento especial à aluna Ana Cláudia Abreu pelas análises feitas em momentos de maior necessidade.

Ao professor Giuseppe Mele, pelas análises de microscopia eletrônica de transmissão.

Ao professor Igor Frota, pelas análises Mössbauer feitas de forma bastante rápidas e em momentos de grande necessidade.

Ao Danilo Queiroz e Carol Moura pelas análises de relaxatividade.

Ao Manuel Banobre, pela tremenda ajuda nas análises magnéticas e de relaxatividade e pela contribuição científica ao trabalho.

Ao Laboratório Internacional Ibérico de Nanotecnologia, pelas análises de relaxatividade e medidas magnéticas.

Ao Laboratório de Espectroscopia Vibracional e Microscopia, pelas análises de espectroscopia na região do infravermelho. Agradecimento especial aos colegas, Juliene Toméh e Antonio César Honorato, pela ajuda na realização dos experimentos.

Ao professor Odair Pastor, pela disponibilização do equipamento para realizar as medidas de espalhamento dinâmico de luz. Especialmente à colega Laís Helena, pelo treinamento de utilização no referido equipamento.

A todos os membros do Grupo de Química de Materiais Avançados (GQMat) por todo o apoio prestado nos dois últimos anos.

Agradecimento especial ao meu orientador/amigo, Pierre Fachine, por todos os ensinamentos compartilhados durante os seis em que trabalhamos juntos.

A todos os amigos, familiares e padrasto, Luciano Fernandes, que sempre me ajudaram e entenderam os momentos de ausência devido ao desenvolvimento desta pesquisa.

A minha namorada, Dayany Barros, pelo apoio e compreensão.

Agradecimento muito especial a minha mãe, Ana Veiga, meu pai Iraldo Machado; por terem disponibilizado tudo que tenho em minha vida e, principalmente, por nunca hesitarem em investir nos meus estudos.

“Se você quer os acertos, esteja preparado
para os erros.” (Carl Yastrzemski)

RESUMO

Nanopartículas (NPs) funcionalizadas emergiram como promissores candidatos para serem aplicadas como agente de contraste para imagem por ressonância magnética nuclear e sua metodologia de síntese e funcionalização afetam fortemente sua performance *in vivo*. A metodologia mais utilizada para a produção dessas NPs funcionalizadas é a decomposição térmica, a qual tem provado ser financeiramente desfavorável, laboriosa além de requisitar longos tempos de execução. Portanto, este trabalho tem como objetivo descrever uma metodologia fácil e rápida, através do método sonoquímico, para a síntese e funcionalização de NPs de Fe_3O_4 com excelentes propriedades físico-químicas com objetivo de serem aplicadas como agente de contraste para imagem por ressonância magnética nuclear. Neste trabalho, o método sonoquímico foi usado para produzir, em 12 min, NPs de Fe_3O_4 funcionalizadas com policrilato de sódio, citrato de sódio, polietilenamina ramificada e oleato de sódio. Difração de raios-X e microscopia eletrônica de transmissão demonstraram que as NPs produzidas são compostas de uma única fase de espinélio inverso de 9-11 nm de diâmetro e uma distribuição de tamanho estreita. Foi confirmado por meio da espectroscopia Mössbauer e medidas magnéticas que as NPs sintetizadas estão em transição para o regime superparamagnético e que possuem excelente valor de magnetização de saturação (59-77 emu/g) para aplicações biomédicas. Espectroscopia de infravermelho por transformada de Fourier provou que a radiação sonoquímica forneceu condições adequadas para que acontecesse uma interação forte entre o núcleo magnéticos e os agentes funcionalizantes. Além disso, experimentos de espalhamento dinâmico de luz confirmaram que as amostras recobertas com moléculas orgânicas hidrofílicas possuem estabilidade coloidal em solventes aquosos. Destaque deve ser dado a nanopartícula magnética recoberta com poliacrilato de sódio, que demonstrou excelente estabilidade coloidal em condições fisiológicas simuladas. Finalmente, as NPs obtidas se mostraram serem promissores candidatos a agentes de contraste. Uma vez que seus valores de relaxatividade transversal foram maiores que os agentes de contraste comerciais e daqueles preparados por outras metodologias sintéticas. Portanto, este trabalho trás um grande avanço no que se refere a preparação de NPs de Fe_3O_4 funcionalizadas para aplicações biológicas, uma vez que materiais de alta qualidade foram preparados de forma rápida e fácil.

Palavras-chave: Sonoquímica; Nanopartículas magnéticas, funcionalização de nanomateriais; Imagem por ressonância magnética nuclear.

ABSTRACT

Functionalized Fe₃O₄ nanoparticles (NPs) have emerged as a promising contrast agent for magnetic resonance imaging (MRI). Their synthesis and functionalization methodology strongly affects their performance *in vivo*. Although thermal decomposition is the most commonly used growth methodology reported in the literature, it has proven to be time-consuming, expensive, and laborious. Therefore, this work describes a rapid and facile sonochemical methodology to synthesize and functionalize Fe₃O₄ NPs with excellent physico-chemical properties for MRI. In this work, a sonochemistry approach was used to produce, in 12 min, Fe₃O₄ NPs functionalized with polysodium acrylate (PAANa), trisodium citrate (CIT), branched polyethylenimine (BPEI), and sodium oleate. X-ray diffraction and transmission electron microscopy demonstrated that the NPs were composed of a single inverse spinel phase with an average diameter of 9–11 nm and a narrow size distribution. It was confirmed by Mössbauer spectroscopy and magnetic measurements that the obtained NPs were transitioning to the superparamagnetic regime and possessed excellent magnetization saturation values (59–77 emu/g). Fourier transform infrared spectroscopy proved that the sonochemistry approach provided conditions that induced a strong interaction between Fe₃O₄ and the capping agents. Furthermore, dynamic light scattering experiments evidenced that samples coated with PAANa, CIT, and BPEI possess colloidal stability in aqueous solvents. Emphasis must be placed on PAANa-coated NPs, which also presented remarkable colloidal stability under simulated physiological conditions. Finally, the obtained NPs exhibited great potential to be applied as an MRI contrast agent. The transverse relaxativity values of the NPs synthesized in this work (277–439 mM⁻¹s⁻¹) were greater than those of commercial NPs and those prepared using other methodologies. Therefore, this work represents significant progress in the preparation of Fe₃O₄ NPs, providing a method to prepare high-quality materials in a rapid, cost-effective, and facile manner.

Keywords: Sonochemistry; Magnetic Nanoparticles; Functionalization of nanomaterials; Magnetic Resonance Imaging.

LIST OF FIGURES

Figure 1 - Representative structure of Fe ₃ O ₄	17
Figure 2 - Magnetic behavior in (A) Ferromagnetic, (B) Ferrimagnetic and (C) Antiferromagnetic.....	18
Figure 3 - Schematic illustration of the particle size effect on: (A) on the domain state and (B) in Hysteresis loops of spinel ferrite materials. Blue and red lines are the first and the second runs, respectively.....	20
Figure 4 - (A) Schematic representation of magnetic drug delivery system acting at cancer infected tissue. (B) Illustration of the synthesis mechanism for a pH-sensitive drug delivery system. (C) TEM images showing the structure before and after the insertion of a CaP shell. (D) Drug profiles realized in solutions with different pH values.	22
Figure 5 - (A) TEM image of extremely small Fe ₃ O ₄ NPs. (B) T1-weighted MR image of cell pellets after 24 h of incubation with ultra-small MNPs. (C) High-resolution blood pool MR image after intravenous injection of ESIONs (JV = jugular vein, AV = axillary vein, SVC = superior vena cava, IVC = inferior vena cava, CA = carotid artery, SV = subclavian vein, and AA = aortic arch).....	24
Figure 6 - (A) External magnetic field varied in region of interest. (B) Using an infrared camera, it is possible to see that the heat is concentrated in the extracranial tumor. (C) Animal trial data on hyperthermia treatments in rabbits, showing preferential heating of a tumor using intra-vascularly infused ferromagnetic microspheres: (■) tumor edge, (◆) tumor centre, (▲) normal liver 1–2 cm from tumor, (×) alternative lobe, and (◇) core body temperature.	25
Figure 7 - Schematic showing <i>in situ</i> co-precipitation synthesis process for MNPs in polymer chains.	27
Figure 8 - Schematic illustration of shape evolution of hematite nanostructures at different reaction times and different ferric concentrations.	29
Figure 9 - Schematic illustration of LaMer model.	30
Figure 10 - (A) Individual methods used in chemistry as function of time, pressure, and energy, and (B) schematic representation of transient acoustic cavitation.....	32

Figure 11 – (A) Experimental apparatus used in synthesis and functionalization of MNPs. (B) Structures of CAs used in this work.	40
Figure 12– (A) Timeline of synthesis and functionalization of MNPs, sequence for addition of reactants, and proposed mechanism of sonochemical synthesis and functionalization of MNPs. (B) Magneto-fluid response of the samples herein synthesized.....	46
Figure 13 – XRD patterns of obtained NPs. The black dots and red line show the experimental and calculated data, respectively. The green line shows the difference between these two parameters.....	47
Figure 14 – TEM micrographs and size-distribution curves of (A) Fe ₃ O ₄ @PAANa, (B) Fe ₃ O ₄ @BPEI, (C) Fe ₃ O ₄ @CIT, and (D) Fe ₃ O ₄ @OLNa samples.....	49
Figure 15 – (A) MS spectra of synthesized samples. The black dots and red lines represent the experimental and calculated data, respectively. Furthermore, for the Fe ₃ O ₄ @OLNa sample, the green and blue lines are the site distributions for the populations of NPs under ferri- and superparamagnetic regimes, respectively. (B) The image shows the hyperfine field distribution curves of each sample. The table at the top of the image summarizes the data extracted from the site distribution. Duple: doublet; sex: sextet; IS: isomer shift; B: magnetic hyperfine field; wid: line width.	51
Figure 16 – ZFC and FC magnetization curves for functionalized NPs prepared in this work.	52
Figure 17 – VSM curves of (A) Fe ₃ O ₄ @PAANa, (B) Fe ₃ O ₄ @BPEI, (C) Fe ₃ O ₄ @CIT, and (D) Fe ₃ O ₄ @OLNa samples; insets: expanded views of low-field regions.	53
Figure 18 – FT-IR spectra of (A) Fe ₃ O ₄ @PAANa, (B) Fe ₃ O ₄ @CIT, (C) Fe ₃ O ₄ @OLNa, and (D) Fe ₃ O ₄ @BPEI samples. For each sample, the spectra of the functionalized NPs and free CA molecules are shown.	55
Figure 19 – Model of interactions between CA molecules and Fe ions of IONPs in (A) Fe ₃ O ₄ @PAANa, (B) Fe ₃ O ₄ @CIT, (C) Fe ₃ O ₄ @OLNa, and (D) Fe ₃ O ₄ @BPEI samples.....	57
Figure 20 – TGA and DTG data for (A) Fe ₃ O ₄ @PAANa, (B) Fe ₃ O ₄ @CIT, (C) Fe ₃ O ₄ @OLNa, and (D) Fe ₃ O ₄ @BPEI samples.	59

Figure 21 – Magnetic R_2 relaxativity of (A) $\text{Fe}_3\text{O}_4@PAANa$, (B) $\text{Fe}_3\text{O}_4@CIT$, (C) $\text{Fe}_3\text{O}_4@BPEI$ samples. T_2 weighted images of aqueous suspensions of the (D) $\text{Fe}_3\text{O}_4@PAANa$, (E) $\text{Fe}_3\text{O}_4@CIT$, and (F) $\text{Fe}_3\text{O}_4@BPEI$ samples.62

LIST DE TABLES

Table 1 - Use of ultrasound method to synthesize Fe ₃ O ₄ NPs.....	34
Table 2 – Parameters extracted from the Rietveld refinement and average size of the NPs calculated through TEM.	48
Table 3 – Results from DLS experiments.	60
Table 4 - Summary of the already reported MRI contrast agents based on Fe ₃ O ₄ NPs prepared by the most traditional synthetic methodologies.	63

SUMMARY

1. BIBLIOGRAPHIC REVIEW	16
1.1. Magnetite (Fe ₃ O ₄): structure and magnetic properties	16
1.1.1 Structure	16
1.1.2 Magnetic Properties.....	18
1.2. In Vivo Applications of Fe ₃ O ₄	21
1.2.1 Drug delivery.....	21
1.2.2 Magnetic resonance imaging (MRI).....	22
1.2.3 Magnetic hyperthermia.....	24
1.3. Main Methodologies for Synthesis and Functionalization of MNPs.....	26
1.3.1 Co-precipitation.....	26
1.3.2 Hydrothermal or solvothermal method	28
1.3.3 Thermal decomposition	29
1.4. Ultrasound: Theory and Application in Synthesis of Fe ₃ O ₄	31
2. JUSTIFICATION FOR RESEARCH.....	36
3. OBJECTIVES	39
3.1 General Objective	39
3.2 Specific Objectives	39
4. MATERIALS AND METHODS.....	40
4.1 Chemicals.....	40
4.2 Synthesis and Functionalization of Fe ₃ O ₄ with PAANa, BPEI, and CIT	40
4.3 Functionalization of Fe ₃ O ₄ NPs with OLN _a	41
4.4 Characterizations of NPs	42
5. RESULTS AND DISCUSSION	45
5.2.1 XRD.....	47
5.2.2 TEM.....	49
5.2.3 Mössbauer spectroscopy.....	50
5.2.4 Magnetic measurements	52
5.3 Coating.....	55
5.3.1 FTIR	55
5.3.2 TGA.....	58
5.4 Colloidal Properties	60
5.5 MRI Properties.....	61

6. CONCLUSIONS	66
7. REFERENCES	67

1. BIBLIOGRAPHIC REVIEW

1.1 Magnetite (Fe₃O₄): structure and magnetic properties

1.1.1 Structure

Fe₃O₄ belongs to a huge class of ceramics materials called spinel ferrites. All oxides of this class possess the same structure of the natural spinel MgAl₂O₄. According to the literature(1), over 140 oxides and 80 sulphides were already synthesized and their physicochemical properties studied. This large variety of spinels is due to their capacity to incorporate cations with different charges into the structure. However, the total positive charge should not be higher than 8 to balance to the charge of the anions. Another requirement is about the cation radii. The values must be in the range of 0.4-0.9 Å. Magnetic spinels usually have the general formula of M²⁺Fe₂O₄ (or MO.Fe₂O₃), where the divalent cation can be Mn, Ni, Fe, Co, Zn, Mg, etc. Fe₃O₄ is the most important and abundant among other oxides of this class (2).

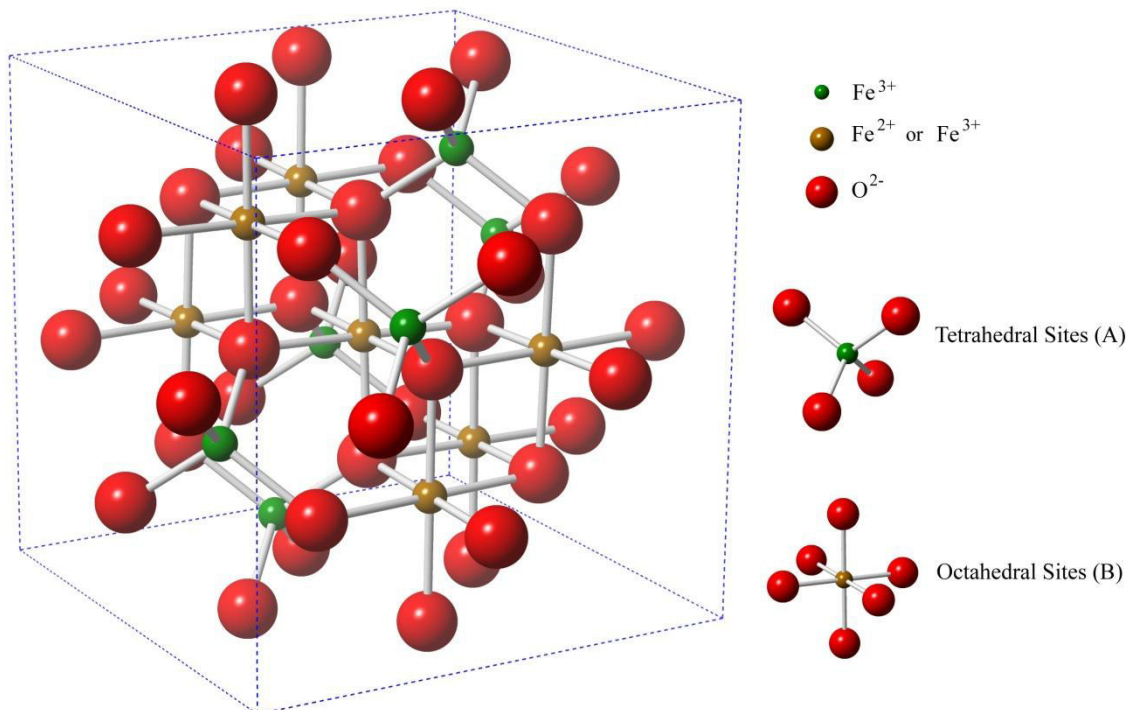
The crystalline structure of spinel ferrites was firstly determined by Bragg (3) in 1915. In the spinel structure, the metallic ions are coordinated to oxygen with two different ways, which generate two coordination sites. The first one is called A site and the cation is coordinated in tetrahedral symmetry. The second one, namely B sites, is coordinated in octahedral symmetry as it can be seen in the Figure 1. Spinel space group is Fd3m and the unit cell contains eight units AB₂O₄ counting 56 ions per unit cell (16 cations in A sites, 32 cations in B sites and 32 oxygen directly bonded to the cations).

According to distribution of trivalent and divalent cations, spinels can be classified as:

- a) *Normal Spinel* – Divalent cations are present in A sites, while the trivalent cations are in B sites. For instance, zinc ferrite (ZnFe₂O₄) presents Zn²⁺ in tetrahedral sites (A) and Fe³⁺ in octahedral sites (B). The general formula for normal spinels is (M¹²⁺)[Fe³⁺]₂O₄, where the square brackets indicate B sites occupancy and parentheses denote the cation in A sites;
- b) *Inverse Spinel* – Divalent cations are in B sites, while the trivalent cations are in A and B sites. Fe₃O₄ is an example of inverse spinel. Half of its Fe³⁺ is located in A sites and all Fe²⁺ occupy the B sites. The general formula of inverse spinel is (Fe³⁺)[M¹²⁺Fe³⁺]₂O₄;

c) *Mixed Spinel* –In some cases, the divalent cation has no defined preference between A or B site. Then, it distributes in both sites leading to a formation of *mixed spinel*. Its general formula is $(M1^{2+}_{1-\delta} Fe^{3+}_{\delta})[M1^{2+}_{\delta} Fe^{3+}_{2-\delta}]O_4$, where δ is the degree of inversion. The degree of inversion depends mainly on the preparation technique and synthetic conditions (4). For instance, Galvão et al. (5) evidenced the migration of Fe^{3+} cations among tetrahedral and octahedral sites increasing the microwave heating time.

Figure 1 - Representative structure of Fe_3O_4



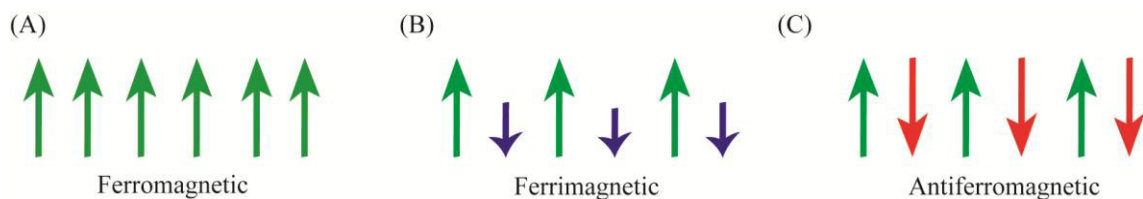
Source: Super-paramagnetic Nanoparticles with Spinel Structure: A Review of Synthesis and Biomedical Applications (6)

Once the distribution of divalent and trivalent cations plays an important role in the magnetic properties of spinel materials, each one of these of spinels posses distinct magnetic properties. For example, inverse spinels tend to be ferrimagnetic, whereas normal spinels paramagnetic (7). Indeed, this peculiar distribution of the cations among A and B sites lead Néel to conclude about the ferrimagnetism of the spinel ferrites(8).

1.1.2 Magnetic Properties

Ferrimagnetic materials exhibit a net magnetization similar to the ferromagnetism. The difference between them is the alignment of the spins. For ferromagnetic materials, all spin moments are aligned parallel to each other. Unlike, ferrimagnetic materials display spin moments aligned anti-parallel. However, they are not completely canceled keeping a net magnetic moment. Figure 2. A and B illustrate the alignment of the spins as well as the interactions achieved for ferromagnetism and ferrimagnetism, respectively (1). The remaining magnetism of the ferromagnetic materials can be explained by exchange interactions, which emerge from the presence of oxygen between the cations. In spinel ferrites, the magnetic interactions can occur between the cations occupying A and B sites (A-B), B sites (B-B) and A sites (A-A). It is worth to mention that when these interactions occur the spins for each site become anti-parallel.

Figure 2 - Magnetic behavior in (A) Ferromagnetic, (B) Ferrimagnetic and (C) Antiferromagnetic



Source: Super-paramagnetic Nanoparticles with Spinel Structure: A Review of Synthesis and Biomedical Applications (6)

Usually, net magnetic moment happens with inverse or mixed spinel ferrites where the A-B sites interactions predominate. To illustrate this situation, we can consider inverse spinel Fe_3O_4 . All Fe^{2+} ions are in B sites and Fe^{3+} are divided among A and B sites. Thus, the magnetic moment of Fe^{3+} ions situated in A and B sites are anti-parallel cancelling each other. The magnetization found for this ferrite is due to the five unpaired electrons of Fe^{2+} ions. On the other hand, normal spinels are quite different. The cations in A sites do not present net magnetization and the absence of A-B interactions is observed. As a consequence, B-B interactions dominate. Therefore, the spinel will not present net magnetic moment owing to the moments in B sites. Since an anti-parallel alignment is achieved, therefore, no magnetism is observed. For instance, ZnFe_2O_4 is a normal spinel and the non-magnetic Zn is located in A sites. The spin moments of Fe^{3+} turn out anti-parallel and no magnetic moment can be found. Figure 3 (C) exhibits the behavior of the spins for antiferromagnetic materials

(4). Besides the organization of di- and trivalent cation, the magnetic behavior of the spinel ferrites is also size- and temperature-dependent. These parameters play a very important role. For instance, when size of particles of some inverse-spinel reach a critical value, its magnetic properties at room temperature exhibit the superparamagnetism (SPM). Which brought new possible applications for magnetic nanoparticles (MNPs), especially for the low-toxic Fe_3O_4 .

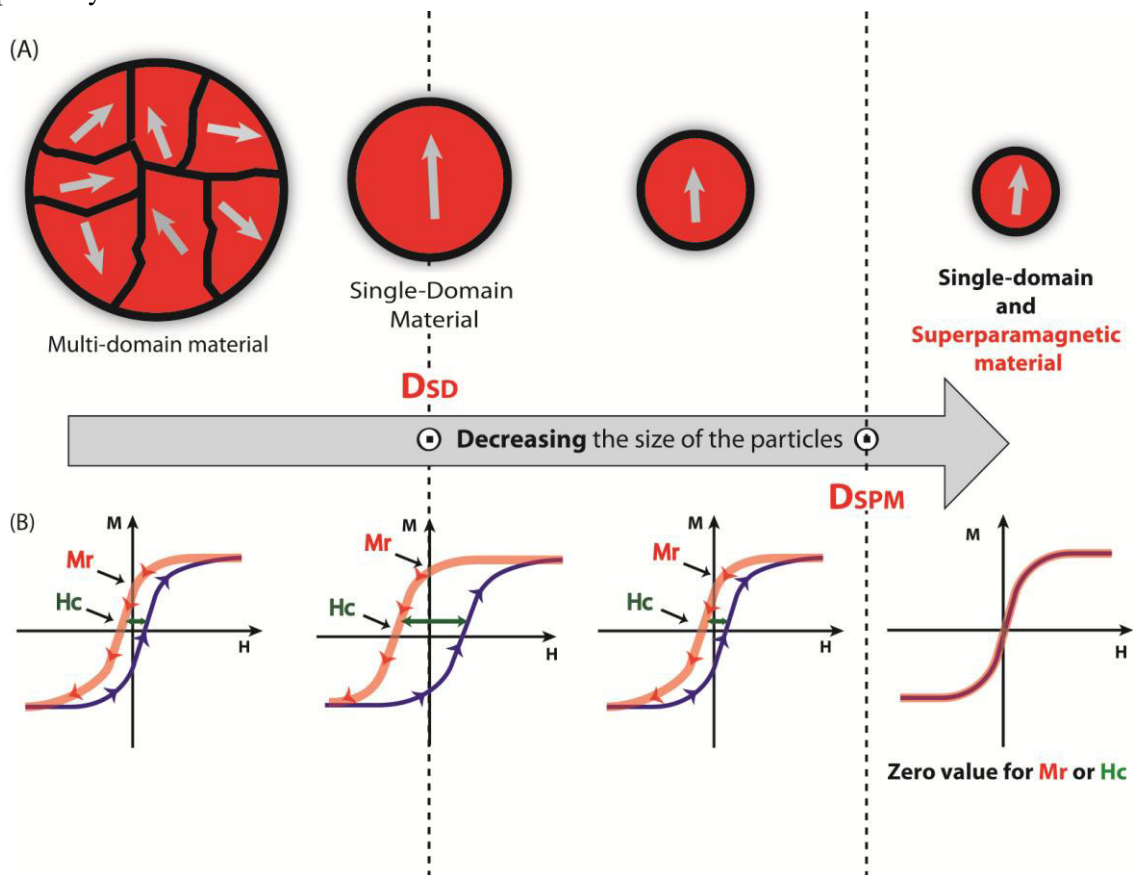
The difference between of SPM for ferri- and ferromagnetism is that, SPM materials do not display remnant magnetization (M_r). This means that Materials with this remarkable property exhibit no magnetization upon removal of the external magnetic field (6). Thus, no aggregation due to the remained magnetic field can be found, which enables applications in the biological environment.

The SPM is strongly related to the NPs size. Therefore, the understanding about this phenomenon is necessary to know what magnetically happens for bigger and smaller NPs. There will be few regions of uniform magnetization separated by boundaries (domain walls, Figure 3 (A)) when the NPs with a certain size have multi-domain state. However, more energy is required to create a domain wall when NPs size starts to decrease. Therefore, if a material is reduced below the so-called critical size to single-domain (D_{SD}), the energy required to hold a domain-wall is greater than support the magnetostatic energy. In this case, it is more energetically favourable for the material to become single-domain (SD) (9). This means that the magnetic moment of each particle will point to the same direction, that is determined by magnetocrystalline anisotropy (Figure 3 (A)) (10). In other words, for a particle to reach the SD state, the size should be greater than the thickness of the domain wall and SD materials differ from each other in relation to the coercive field (H_c), which must be applied in the negative direction to bring the magnetization of the sample back to zero (9). In SD particles, the magnetization/demagnetization processes are dominated by magnetization rotation which requires relatively high external field. Unlike, in multi-domain state, lower external fields are necessary, once magnetization/demagnetization process is dominated by domain-wall motion (11,12). As a consequence of this fact, materials with single-domain display a larger hysteresis. Therefore, it is possible to observe bigger M_r and H_c values (Figure 3 (B)). However, continuously decreasing the NPs size below the D_{SD} , there is a decreasing of the H_c and thermal energy starts to play an important role over relaxation processes of the spins. A further decrease of the NPs size leads to the formation of a SPM material. This kind of MNPs exhibit H_c and M_r value equal to zero. Thus, no hysteresis is found (Figure 3 (B)). In this case, the thermal energy is higher enough to overcome the energy

barrier (anisotropy forces) and the relaxation of the spins happens even in the absence of a magnetic field.

In summary, the SPM behaviour displayed by Fe_3O_4 NPs brought the possibility to solve problems in the field of biomedicine, mainly in the treatment of cancer. Besides the SPM, magnetic properties of NPs can be used *in vivo* in three main ways. The first is incorporate some anti-cancer drug on the NPs and use an external magnetic field to orientate directly to the infected tissue. Second, it is as magnetic contrast agent in magnetic resonance imaging. Last, as hyperthermia or thermoblation agents, where MNPs, through varying of the magnetic field, heat and kill selectively cancer cells. Thus, scientists around the world start to intensively study which structural and magnetic features of the NPs affects the their *in vivo* performance (13).

Figure 3 - Schematic illustration of the particle size effect on: (A) on the domain state and (B) in Hysteresis loops of spinel ferrite materials. Blue and red lines are the first and the second runs, respectively



Source: Super-paramagnetic Nanoparticles with Spinel Structure: A Review of Synthesis and Biomedical Applications (6)

1.2 In Vivo Applications of Fe₃O₄

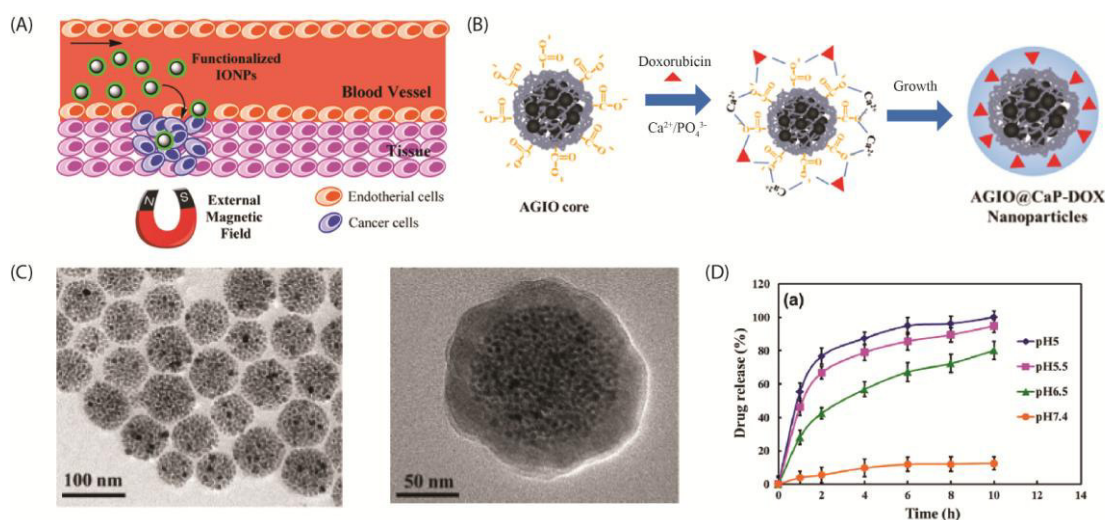
1.2.1 Drug delivery

In traditional drug delivery methods such as oral ingestion and intravascular injection, the drug is distributed throughout the body by the systemic bloodstream. Thus, the drug loading must be higher than the required dosage to reach the affected tissue at a sufficient concentration to treat the disease (13). However, using Fe₃O₄ NPs as a carrier for some neoplastic agents, along with an external magnetic field, would make it possible to concentrate the medication in the tissue of interest. This would decrease the concentration of the medication in healthy tissues, which would decrease the side effects (Figure 4 (A)). Therefore, magnetic drug delivery systems are promising candidates for the treatment of cancer. The use of this method will prevent the side effects caused by conventional chemotherapy by reducing the systemic distribution of drugs and the doses of cytotoxic compounds (14). Generally, magnetic drug delivery systems are composed of a magnetic core covered by a biocompatible component that acts as a shell. The drugs are usually bound or encapsulated within this shell. In a drug carrier system, the sizes, surface properties, and colloidal stability are crucial features that determine the usefulness of the carrier (15). Therefore, the synthetic methodology for the synthesis of the core, composition of the shell, and appropriate strategy for incorporating the drug play key roles in obtaining a good performance from a magnetic drug carrier.

When the carrier reaches the target site, the drug is released to the cells via an enzymatic activity or a change in a physiological condition such as the pH, osmolality, or temperature. This has allowed the development of smart control release systems that respond to changes in physiological conditions and deliver drugs with a higher specificity. For instance, Li *et al.* developed a pH-responsive amphiphilic gelatin–iron oxide core/calcium phosphate shell drug carrier to deliver an anticancer drug, doxorubicin (DOX) (16) (Figure 4 (B and C)). Based on the fact that the pH of extracellular tumor tissue is lower than that of normal tissue (17), they fabricated the shell of the carrier based on calcium phosphate (CaP), which rapidly dissolves in an acidic environment but remains stable in a neutral environment (16). In drug release tests, the authors found that at a neutral pH, the DOX release was relatively slow, <20% over a period of 24 h. They suggested that the CaP shell acted as effective barrier for DOX diffusion. On the other hand, the rapid release of the DOX

molecules was clearly observed at acidic pH levels. For example, at pH 5.0, 100% of the DOX was eluted when immersed for 10 h (Figure 4 (D)).

Figure 4 - (A) Schematic representation of magnetic drug delivery system acting at cancer infected tissue. (B) Illustration of the synthesis mechanism for a pH-sensitive drug delivery system. (C) TEM images showing the structure before and after the insertion of a CaP shell. (D) Drug profiles realized in solutions with different pH values.



Source: Recent progress on magnetic iron oxide nanoparticles: synthesis, surface functional strategies, and biomedical applications (13), and In situ doxorubicin–CaP shell formation on amphiphilic gelatin–iron oxide core as a multifunctional drug delivery system with improved cytocompatibility, pH-responsive drug release, and MR imaging (18)

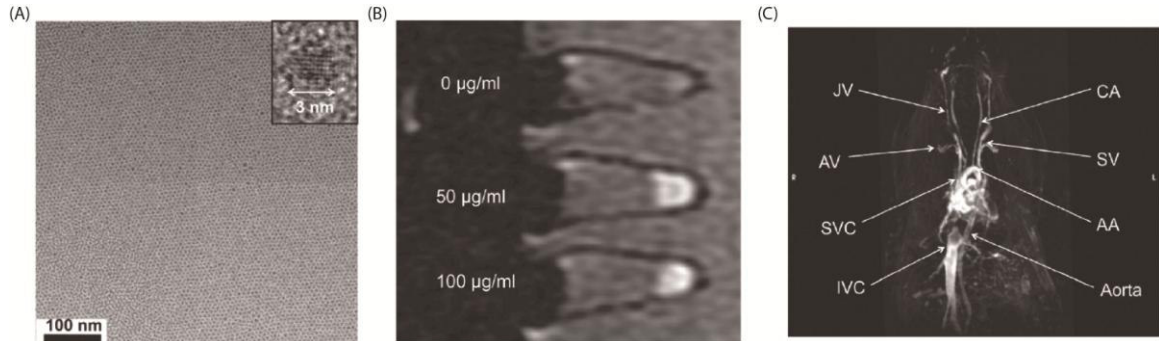
1.2.2 Magnetic resonance imaging (MRI)

MRI is a non-invasive imaging technique used to produce high-quality images of the human body. This technique has been used to make diagnoses for clinical purposes. It is based on the principle of nuclear magnetic resonance. Briefly, ¹H, ¹¹B, ¹³C, ¹⁹F, or ³¹P can be used as the signal source for MRI. However, the water proton (¹H) is the most commonly used source for clinical purposes because of its sensitivity and abundance in biological tissues (19). The image formation process begins with spin excitation caused by the application of radiofrequency pulses. When the pulse is removed, the spin returns to its ground state, emitting energy. This process is called relaxation and the MRI time of the process. There are two signals recorded: longitudinal (T₁) and transverse (T₂). The measured discrepancy between these times produces the contrast observed in the image (20). It is worth mentioning that the relaxation time is an environment-dependent parameter. Therefore, the discrepancies between the two times will be different for healthy and unhealthy tissues. As a consequence, a

tumor can be easily detected, allowing the patient to be treated. However, in many cases, the contrast difference between the target and normal tissues is negligible, making it harder to obtain the correct diagnosis. To solve this problem, contrast agents were developed to increase the signal difference by improving the contrast between pathological lesions and normal tissues (21). However, the lack of specificity is still a problem for MRI contrast agents. Their poor sensitivity makes their use unfeasible for accurately detecting small targets such as tumors in an early stage of cancer (22). Therefore, MNPs appear to be an excellent alternative because they can be easily functionalized with molecules that selectively bind with cancer cells and can be delivered to the targeted site using an external magnetic field (13). Additionally, their unique superparamagnetic properties generate significant susceptibility effects, which result in strong T_2 and T_1 values at very low concentrations for MRI (23–25). Therefore, MRI is one of the most promising applications of magnetic MNPs.

Because the relaxation process is an environment-dependent parameter, the accumulation of MNPs in the target tissue can change the local physiochemical properties and enable the detection of a pathological lesion. Furthermore, the MRI properties of MNPs are dependent on their shape and size. For instance, Young-wook *et al.* (26) synthesized water-soluble MNPs with diameters ranging from 4 nm to 12 nm (Figure 5(A)). They found that 4, 6, 9, and 12 nm NPs had values of 25, 43, 80, and 120 $\text{emu g}^{-1} \text{Fe}$, respectively. Size-dependent magnetization leads to a significant effect under T_2 contrast, which enhances the MRI signal. However, sometimes an extreme enhancement of the T_2 signal produces intrinsic dark signals that can be confused with other hypointense areas such as those containing bleeding, calcification, or metal deposition, which makes diagnosis difficult (19). This problem was solved by preparing extremely small Fe_3O_4 NPs less than 4 nm in size, with a value of 35 emu g^{-1} at 3 T. Because the ultra-small MNPs exhibited a very weak T_2 contrast effect, cell pellets labeled with the NPs showed significant signal enhancement in a T_1 -weighted MR image, even though the nanoparticles were clustered in the endosomes (Figure 5 (B)). Furthermore, these NPs had a long circulating time in the bodies of mice, enabling high-resolution MRI, which made it possible to perform a detailed analysis of blood vessels as small as 200 μm in size (Figure 5 (C)).

Figure 5 - (A) TEM image of extremely small Fe_3O_4 NPs. (B) T1-weighted MR image of cell pellets after 24 h of incubation with ultra-small MNPs. (C) High-resolution blood pool MR image after intravenous injection of ESIONs (JV = jugular vein, AV = axillary vein, SVC = superior vena cava, IVC = inferior vena cava, CA = carotid artery, SV = subclavian vein, and AA = aortic arch).



Source: Large-scale synthesis of uniform and extremely small-sized iron oxide nanoparticles for high-resolution t_1 magnetic resonance imaging contrast agents (27)

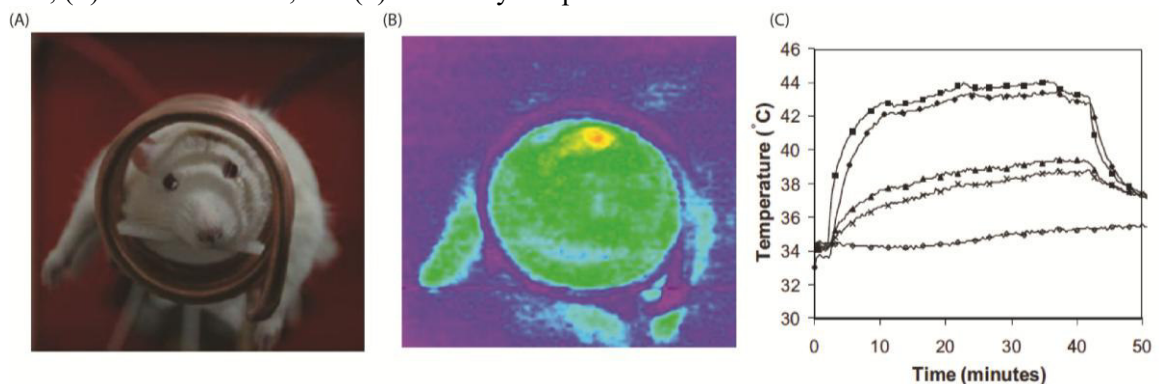
1.2.3 Magnetic hyperthermia

Essentially, hyperthermia treatment is based on the local generation of heat using an external device to transfer energy into the tissue to raise the temperature of the local environment. This idea emerged when an unusual reduction or the complete destruction of cancer cells was observed in patients with a high fever. Later, scientists found that cancer cells are preferably killed when heated at 41–47 °C (28). However, it is necessary to heat the cancer cells selectively to prevent the normal cells from being affected. MNPs are a good agent to transfer heat to cancer cells for this purpose. However, the MNPs must be functionalized in order to possess good colloidal stability in water. In hyperthermia treatment, an aqueous suspension of functionalized MNPs is injected directly into the tumor. Then, the injured area containing the NPs is subjected to an alternating magnetic field (Figure 6 (A)). Heat is generated as a result of the presence of the MNPs, and the cancer is treated with few side effects (Figure 6 (B)). The capacity of the MNPs to generate heat is based on a combination of the internal Néel fluctuations of the particles' magnetic moment, hysteresis, and external Brownian fluctuations (13). To destroy the cancer, the temperature must be maintained above the threshold of 42 °C for 30 min or more (29). The great advantage of magnetic hyperthermia is the specificity of the heating. After the MNPs penetrate and accumulate in cancer cells, the heating will proceed in the majority of the target tissue (29)(Figure 6 (C)).

The most active companies involved in hyperthermia treatment involving MNPs are MagForce Nanotechnologies AG (Berlin, Germany; www.magforce.de) and Dr. Sennewald Medizintechnik GmbH (Munich, Germany; www.sennewald.de) (30). Both companies have developed very useful software platforms for planning the thermal therapy (see each company's website). For example, NanoPlan® (the software developed by MagForce Nanotechnologies AG) makes it possible to define some parameters such as the estimation time, along with an assessment of the risks during the temperature elevation stage (6).

Recently, Riccardo *et al.* made great progress in understanding how the cellular environment affects the magnetic properties of NPs and, as consequence, the hyperthermia efficiency (31). They synthesized a wide range of different types of MNPs, including nanocubes, nanoflowers, nanoparticles in liposomes, Au@ γ -Fe₂O₃ dimmers, and CoFe₂O₄ (in or close to the ferromagnetic regime). They measured their hysteresis loops and specific power losses in water, on cell membranes, and inside the cells. The authors found that the heating power began to fall as soon as the NPs attached to the cell membranes. However, the amplitude of this fall was dependent on the magnetic behavior of the material. For instance, superparamagnetic materials were minimally affected by the cellular environment, in contrast to materials in the ferromagnetic regime. This demonstrated the essential importance of the superparamagnetic behavior.

Figure 6 - (A) External magnetic field varied in region of interest. (B) Using an infrared camera, it is possible to see that the heat is concentrated in the extracranial tumor. (C) Animal trial data on hyperthermia treatments in rabbits, showing preferential heating of a tumor using intra-vascularly infused ferromagnetic microspheres: (■) tumor edge, (◆) tumor centre, (▲) normal liver 1–2 cm from tumor, (×) alternative lobe, and (◇) core body temperature.



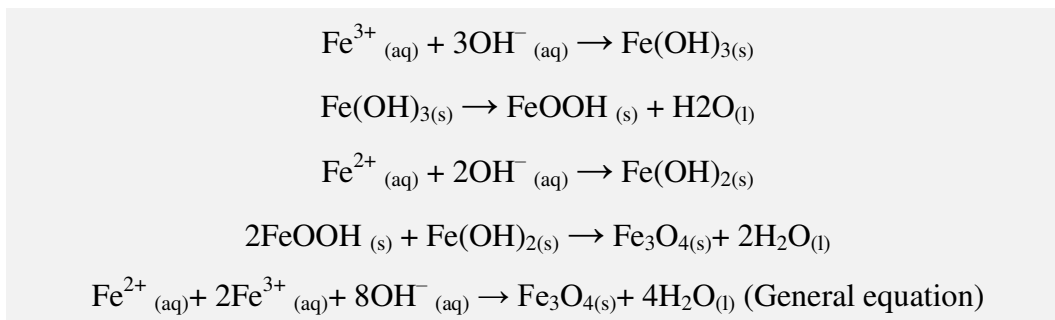
Source: Rapid magnetic heating treatment by highly charged maghemite nanoparticles on Wistar rats exocranial glioma tumors at microliter volume (32) and Applications of magnetic nanoparticles in biomedicine (29)

1.3. Main Methodologies for Synthesis and Functionalization of MNPs

As mentioned in the previous sections, the size and composition play important roles in the magnetic properties of NPs, which consequently affect their performance in *in vivo* applications. All of these properties are a result of the type of synthetic methodology selected to prepare them. Therefore, the selection of the synthetic methodology is of fundamental importance. However, it is not enough to simply synthesize uncoated MNPs for biomedical applications because if they are not functionalized they tend to agglomerate in order to reduce their surface energy, which can lead to serious problems for patients. Therefore, colloidal stability is an absolute requirement for NPs in a physiological medium (33). To solve this problem, it is necessary to coat NPs with a suitable biocompatible compound to suppress the aggregation of iron oxide NPs by suppressing their magnetic interactions and, additionally, provide functional groups for the attachment of a bioactive compound (e.g., drug) (34). In order to achieve efficient functionalization, it is preferable to perform the synthesis and coating of MNPs in a single step, because an irreversible agglomeration occurs after Fe₃O₄ NPs are completely dried, making it impossible to achieve good dispersibility. Therefore, this section focuses on the most important established methodologies to synthesize and functionalize MNPs.

1.3.1 Co-precipitation

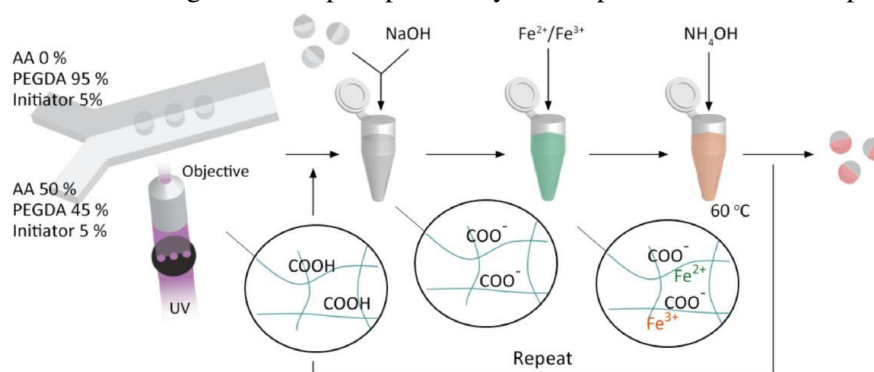
Co-precipitation is one of the oldest synthetic methodology to obtain spinel ferrites (35). This process uses a mixture of metallic salts containing (cation I)²⁺ and (cation II)³⁺ ions. Under vigorous stirring, the metallic mixture is heated, and the precipitant agent (usually an alkaline chemical like sodium hydroxide (NaOH)) is added. Then, the formation of the precipitate should be observed. Basically, this process consists of condensation reactions where the species in solution bond together through oxygenated bridges. Initially, the concentration of the metal hydroxide species (M-OH) quickly increases with the addition of the base. Subsequently, the M-OH is converted into metal oxides (M-O) through the replacement of the hydroxide bridges by oxygen bonds (36). For some spinel ferrites such as Fe₃O₄, this is the process that is needed to obtain a crystalline phase, as well as magnetic properties. In this case, the chemical equations to obtain Fe₃O₄ are as follows:



The size, shape, and composition of the MNPs depend on the experimental parameters, including the types of iron salts (chlorides, perchlorates, sulfates, nitrates, etc), concentrations of these salts, Fe(II)/Fe(III) ratio, final pH value, and ionic strength of the medium (13). Recently, Hans *et al.* conducted a study that focused on the impact of the synthesis parameters on the co-precipitation process for superparamagnetic iron oxide NPs (37). The authors performed an experimental design study and found that the magnetization saturation (M_s) of the particles could be enhanced by employing high iron salt concentrations and a molar $\text{Fe}^{3+}/\text{Fe}^{2+}$ ratio of less than 2:1. Furthermore, the particle size could be increased using a higher iron salt concentration and hyperstoichiometric normal ratio of hydroxide ions to iron ions of 1.4:1.

After the first reported co-precipitation synthesis performed by Massart (38), this methodology was widely studied for the preparation of Fe_3O_4 NPs because of its extraordinary advantages, which include gram-scale production capacity (13). Additionally, Suh *et al.* reported the *in situ* synthesis of nonspherical MNPs in a carboxyl functionalized polymer matrix, in which iron ions were diffused into polymer particles. They then chelated with the deprotonated carboxyl groups, nucleated, and finally grew into the MNPs in the polymer particles (39) (Figure 7).

Figure 7 - Schematic showing *in situ* co-precipitation synthesis process for MNPs in polymer chains.



Source: Synthesis of nonspherical superparamagnetic particles: *in situ* coprecipitation of magnetic nanoparticles in microgels prepared by stop-flow lithography (39).

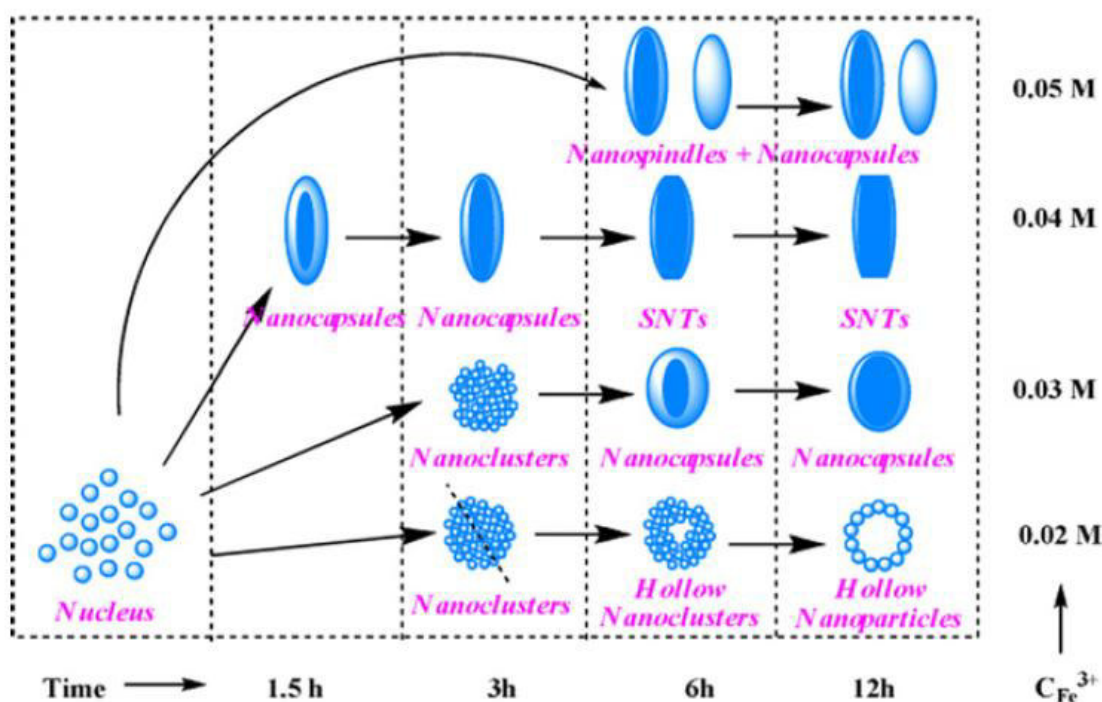
Although co-precipitation is a successful and classic technique for synthesizing MNPs, it still has the great drawback of poor size distribution control, which results in the generation of polydispersed NPs (40).

1.3.2 Hydrothermal or solvothermal method

In the mid-19th century, geologists and analytical chemists needed to dissolve substances with poor solubility under natural conditions. They accomplished this using the hydrothermal/solvothermal method (41), where a substrate was placed in a closed reactor and heated to a temperature higher than the boiling point of the solvent. As a result, the analyte was dissolved and analyzed. This approach later became one of the most important methods for fabricating MNPs with improved properties. The essential difference between the hydrothermal and solvothermal processes is the solvent. In the hydrothermal method, the solvent used is water, whereas the solvothermal method utilizes other chemicals such as methanol, ethanol, ethylene glycol, and glycerol. Freire *et al.* (42) prepared mixed ferrite $\text{Mn}_{0.5}\text{Zn}_{0.5}\text{Fe}_2\text{O}_4$ NPs using different solvent compositions of water and/or ethylene glycol. Under hydro/solvothermal conditions, the results showed the strong correspondence between the MNPs properties and the composition of the reaction environment.

One great advantage of the hydro/solvothermal method is the ability to control the shape of the NPs. For instance, Wu *et al.* presented a facile approach for producing magnetic short nanotubes and other shapes using an anion-assisted hydrothermal route with phosphate and sulfate ions (43). The size, morphology, shape, and surface architecture of the iron oxide were controlled using simple adjustments of the ferric ion concentration. An investigation of the formation mechanism revealed that the ferric ion concentration, amount of anion additive, and reaction time significantly contributed to the growth of the short nanotubes (see Figure 8).

Figure 8 - Schematic illustration of shape evolution of hematite nanostructures at different reaction times and different ferric concentrations.

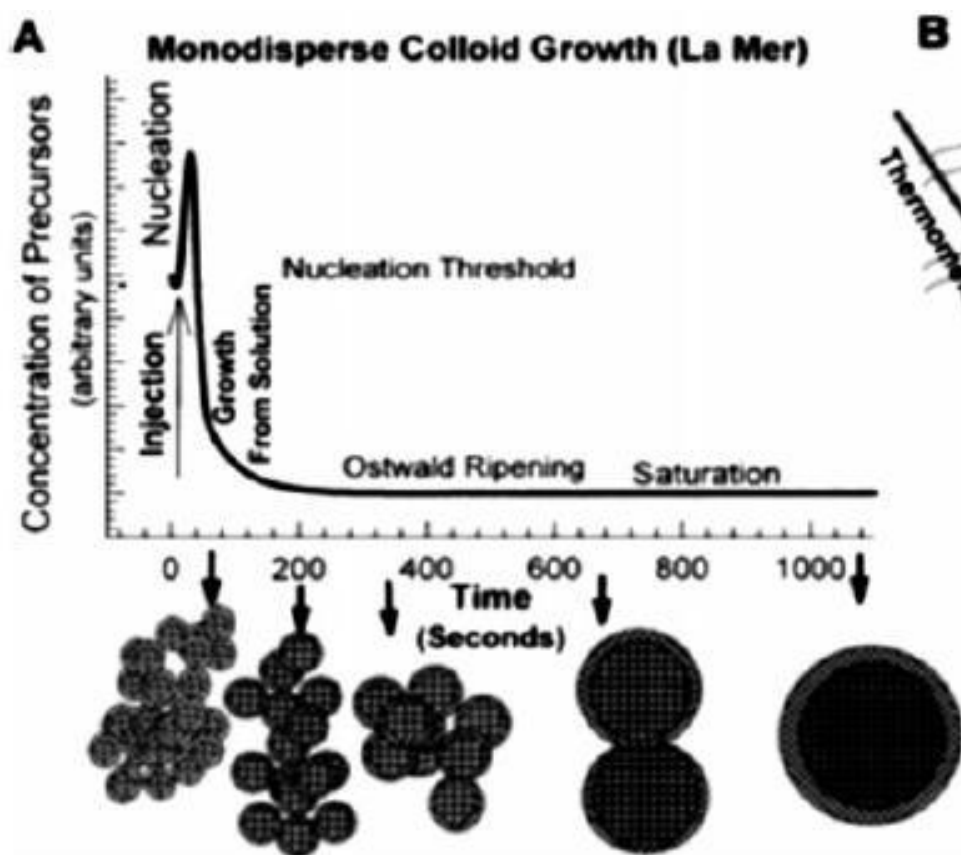


Source: Large-scale and controlled synthesis of iron oxide magnetic short nanotubes: shape evolution, growth mechanism, and magnetic properties (43).

1.3.3 Thermal decomposition

One problem of the two previously mentioned methodologies is that the obtained NPs are not monodispersed. The thermal decomposition methodology solves this problem. For this reason, this methodology has become the most commonly used method to synthesize MNPs (41). The separation of the nucleation and growth steps during the synthesis is the key to obtaining monodispersed NPs. In the theory developed by LaMer (44), burst nucleation occurs when the monomers quickly increase to more than the critical supersaturation level, with no further formation of nuclei afterward (45). The produced nuclei then grow at the same rate, giving monodisperse particles. The process is illustrated in Figure 8. However, small NPs have an extremely high surface area to volume ratio and easily agglomerate to minimize their surface energy. To prevent this agglomeration from occurring, surfactant molecules must be used to coat the particle surface. The repulsive forces introduced by these surfactant molecules between any two NPs prevent the agglomeration of the NPs (46).

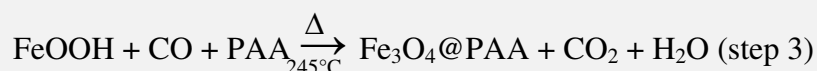
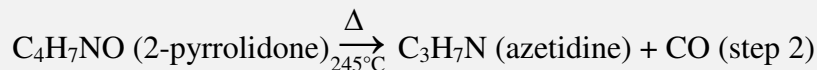
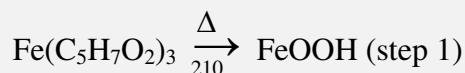
Figure 9 - Schematic illustration of LaMer model.



Source: Synthesis and characterization of monodisperse nanocrystals and close-packed nanocrystal assemblies (45)

In addition to monodispersed NPs, thermal decomposition provides highly crystalline and isolated NPs (40). Generally, thermal decomposition is performed at a high temperature (>200 °C) using metal-organic precursors in nonpolar solvents (47). The most commonly used ferric organometallic compounds are $\text{Fe}(\text{CO})_5$ (48), $\text{Fe}(\text{acac})_3$ (acac = acetylacetonate) (49), iron oleate (50), $\text{Fe}(\text{Cup})_3$ (Cup = N-nitrosophenylhydroxylamine) (51,52), Prussian blue ($\text{Fe}_4[\text{Fe}(\text{CN})_6 \cdot 14\text{H}_2\text{O}]$) (53,54), Fe-urea complex ($[\text{Fe}(\text{CON}_2\text{H}_4)_6](\text{NO}_3)_3$) (55), ferrocene ($\text{Fe}(\text{C}_5\text{H}_5)_2$) (56), and $\text{Fe}_3(\text{CO})_{12}$ (57).

As previously mentioned, a stabilizing agent must be used to prevent the agglomeration and formation of polydispersed NPs. In some cases, this stabilizing agent can act as an organometallic precursor, like an iron oleate complex. However, it is also possible to obtain NPs covered with a hydrophilic coating, like poly-acrylic acid (PAA), as reported by Li *et al.* (58). The mechanism for the formation of MNPs using this method is presented below:



In step 1, iron(III) acetyl acetonate decomposes at 210 °C to the intermediate FeOOH. As expected, the FeOOH particles obtained in this step are nonmagnetic. In step 2, after increasing the reaction temperature to 245 °C, 2-pyrrolidone decomposes to form azetidine and carbon monoxide (CO). Simultaneously, the FeOOH will be partially reduced by the CO, leading to the formation of Fe₃O₄ (containing Fe²⁺ and Fe³⁺) nanoparticles (step 3). These Fe₃O₄ nanoparticles then diffuse through the reaction medium and adsorb on the PAA polymer chains, through the coordination of the COO⁻ groups of PAA with Fe²⁺ cations on the Fe₃O₄ nanoparticle surface (40).

It is worth mentioning that this methodology also has great disadvantages, including a large synthesis time (>1 h), higher temperature (>200 °C), operational difficulty, high cost, and the use of toxic organic precursors (22).

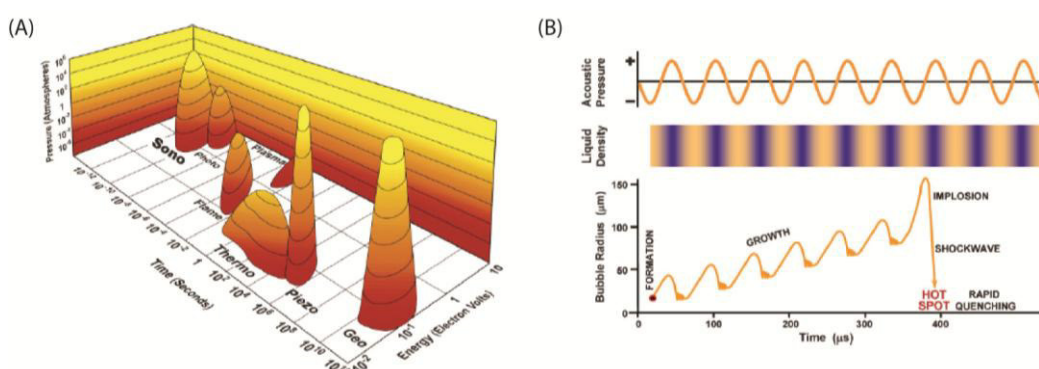
1.4 Ultrasound: Theory and Application in Synthesis of Fe₃O₄

Some form of energy (e.g., heat, light, radiation, electric potential, etc.) is required for the occurrence of a chemical reaction. Each type of energy has its own specific reaction condition features, which are determined by its inherent reaction parameters, as demonstrated in Figure 10 (A) (59). For example, ultrasonic irradiation provides high temperatures and pressures in a short period of time (60), which cannot be provided by other methods. This makes ultrasound radiation a very interesting approach to synthesize a wide range of chemical compounds.

Surprisingly, such extraordinary conditions are not derived directly from the ultrasound itself once the acoustic wavelengths are much larger than the molecular dimensions. Therefore, there is no direct interaction between the ultrasound and the chemical species (61). When a liquid is subjected to ultrasonic irradiation, the acoustic waves create

bubbles and make these bubbles oscillate (see Figure 10 (B)). The energy of the ultrasound method comes from this oscillation, with the ultrasonic energy accumulating as the bubbles grow to a certain size (typically tens of micrometers). When the bubbles grow too large and subsequently collapse, this concentrated energy is released within a very short time. This cavitation is very localized and transient, with a temperature of ~ 5000 K and pressure of ~ 1000 bar (62). For these reasons, ultrasound radiation has been applied to synthesize a wide range of different materials from different sources (59), including Fe_3O_4 NPs.

Figure 10 - (A) Individual methods used in chemistry as function of time, pressure, and energy, and (B) schematic representation of transient acoustic cavitation.



Source: Applications of ultrasound to the synthesis of nanostructures materials (59)

Table 1 lists all of the studies (to the best of our knowledge) that used an ultrasound methodology to synthesize non-functionalized and functionalized Fe_3O_4 NPs. It is easy to note that several studies employed a large synthesis time (60–180 min; see Table 1 entries 1, 2, 3, 8, 10, 12, and 13), which was not expected because sonochemistry makes it possible to reach a high energy level within a very short reaction time.

Functionalized MNPs were also prepared using an ultrasound methodology (Table 1 entries 2, 3, 5, 10, 12, and 14). Thus, based on an analysis of the reported results, it is possible to state that the ultrasound methodology has great potential for use in the preparation of these kinds of materials. The obtained NPs are well dispersed, with good colloidal stability. However, there is no easy and rapid general protocol for the synthesis and subsequent functionalization of a variety of capping agents (CAs). Only two recent papers have reported the coating of MNPs with chitosan (Table 1 entries 15 and 16), one of which was produced by our group (63). In addition, special attention must be given to the evaluation of the chemical interaction between the CA and magnetic core, as well as the manner in which the CA is distributed on the surface of the core. Furthermore, just one of the cited publications reported the potential of using the prepared NPs in biological applications (Table 1 entry 15).

Therefore, the aim of this work was to fill these knowledge gaps regarding the synthesis, functionalization, and biological application of MNPs prepared using the ultrasound methodology.

Table 1 - Use of ultrasound method to synthesize Fe₃O₄ NPs

Entry	Ref.	Brief description	Time required for synthesis (min)	Features of the NPs
1	(64)	Fe ₃ O ₄ NPs were obtained by the sonochemical oxidation of an aqueous solution of iron(II) acetate.	180	The NPs were 10 nm in size, as calculated by XRD.
2	(65)	Functionalized Fe ₃ O ₄ NPs were obtained through the sonolysis of an aqueous solution of Fe(CO) ₅ in the presence of sodium dodecyl sulfate.	180	Highly dispersed 9 nm NPs were obtained. The zeta potential of the NPs was -49.2 mV. An FTIR analysis suggested a chemical bond between the surfactant and Fe ₃ O ₄ NPs.
3	(66)	Fe ₃ O ₄ NPs were coated with SiO ₂ using the alkaline hydrolysis of tetraethyl orthosilicate in ethanol-water under an ultrasonic field.	60–180	A hydrodynamic size of 49–53 nm and PDI of 0.01–0.012 were obtained for Fe ₃ O ₄ @SiO ₂ NPs. The <i>M_s</i> value of the NPs was 48 emu g ⁻¹ .
4	(67)	Magnetic iron oxide NPs were prepared by reverse precipitation under ultrasound radiation.	30	NPs with a diameter of 10 nm and <i>M_s</i> value of 32 emu g ⁻¹ were obtained. The mechanisms of sonochemical oxidation were also discussed.
5	(68)	The binding of a semi-essential amino acid, L-arginine, onto the surface of nano-magnetite was reported, creating a stable aqueous suspension in an <i>in situ</i> one-step method using sonochemical synthesis.	10–60	The initial amino acid concentration was found to play an important role in controlling the particle size and binding motif. Dynamic light scattering and zeta potential measurements indicated that the synthesized NPs were monodispersed and colloidally stable.
6	(69)	Two-dimensional plate-like Fe ₃ O ₄ nanocrystals were synthesized by ultrasonic irradiation in an aqueous solution at a low temperature without protection from oxygen.	30	Nanoplates with thicknesses in the range of 10–20 nm and lateral sizes of 50–90 nm were prepared. These NPs had an <i>M_s</i> value of 54 emu g ⁻¹ .
7	(70)	Magnetic Fe ₃ O ₄ nano-powder was synthesized by ultrasonic-assisted chemical coprecipitation utilizing high purity iron separated from iron ore tailings by an acidic leaching method.	30	The prepared NPs had a diameter of 15 nm and an <i>M_s</i> value of 74.8 emu g ⁻¹ .
8	(71)	A sonochemical approach was proposed for the large-scale synthesis of iron oxide NPs.	105	The synthesized NPs had a diameter of 11 nm and an <i>M_s</i> value of 80 emu g ⁻¹ .
9	(72)	MNPs were prepared through the ultrasonic irradiation of Fe(OH) ₂ in di- and tri-ethylene glycol/water solutions with the volume ratio varying between 7:3 and 3:7.	5–20	The size of the NPs ranged from 10 to 30 nm. The NPs could easily be transferred in hydrophobic solvents.

Table 1 – Continuation

10	(73)	Ionic liquid (IL)-stabilized iron oxide (Fe ₂ O ₃) nanoparticles were synthesized by the ultrasonic decomposition of iron carbonyl precursors in [EMIm][BF ₄] without any stabilizing or capping agents.	90	It was found that the size distribution of the maghemite nanoparticles was 2–6 nm and the <i>M_s</i> value was 14.5 emu g ⁻¹ . The physicochemical properties of ILs containing magnetic Fe ₂ O ₃ nanoparticles (denoted as Fe ₂ O ₃ @[EMIm][BF ₄]), including the surface properties, density, viscosity, and stability, were investigated in detail.
11	(74)	Fe ₃ O ₄ NPs were synthesized in a single reaction sonochemical method using inexpensive and nontoxic metal salt (FeSO ₄ ·7H ₂ O). Subsequently, the crystallinity of the magnetite nanocubes was enhanced by annealing treatment at a temperature of up to 600 °C.	75	Monodisperse magnetite nanocubes with a uniform particle size of about 80 nm were synthesized. The <i>M_s</i> value of the calcined NPs was 90.2 emu g ⁻¹ .
12	(75)	The incorporation of iron cations in graphene oxide was achieved using ultrasonic radiation. Fe ₃ O ₄ NPs were synthesized using calcination at 450 °C for 3 h. Further, the synthesized NPs were used for an H ₂ O ₂ sensor.	180	The Fe ₃ O ₄ crystals at the graphene oxide had a diameter of 25 nm, and the whole composite displayed an <i>M_s</i> value of 30 emu g ⁻¹ .
13	(76)	Fe ₃ O ₄ NPs were synthesized by ultrasonic waves from the chemical reaction and precipitation of ferrous and ferric iron chloride (FeCl ₃ ·6H ₂ O y FeCl ₂ ·4H ₂ O) in a basic medium.	105	The prepared NPs had a diameter of 11 nm and an <i>M_s</i> value of 80.0 emu g ⁻¹ .
14	(77)	In this work, the sonosynthesis of Fe ₃ O ₄ NPs coated with foleate and cisplatin was performed.	15	The NPs had a size range of 21–31 nm, and an <i>M_s</i> range of 60–93 emu g ⁻¹ . The role of the frequency in the absorption of the molecules was evaluated.
15	(78)	Fe ₃ O ₄ NPs coated with chitosan were prepared using an ultrasound bath. The Gd complex was attached to the coated NPs via electrostatic interaction and covalent bonding for MRI applications.	40	The authors obtained NPs with excellent magnetic properties (<i>M_s</i> = 75 emu g ⁻¹) and relaxativity properties (<i>r</i> ₂ = 361.4 mM ⁻¹ s ⁻¹).
16	(63)	Chitosan-coated NPs were produced <i>in situ</i> in a very short time. The NPs produced in this work were shown to be promising candidates for applications in electroanalytical chemistry.	2	The spheroidal NPs had a diameter range of 10–24 nm and an <i>M_s</i> range of 32–57 emu g ⁻¹ . An exceptional electrochemical signal was obtained using the NPs as a modifier for a glassy carbon electrode.

Source: Present author

2. JUSTIFICATION FOR RESEARCH

MNPs have brought new possibilities in the treatment and diagnosis of cancer diseases, overcoming the drawbacks of conventional treatment (79). These MNPs can be used in drug/gene delivery (80), magnetic separation (81), magnetic hyperthermia (82), and stem cell tracking (83). Another application is as a contrast agent for MRI (84), which is a powerful platform for the real-time visualization of cancer-related, cardiovascular, liver, and neurodegenerative diseases (85). Furthermore, MRI is also used to detect diseases associated with the central nervous system, like Alzheimer's (86). MNPs have been extensively applied as a contrast agent for MRI, as summarized in several reviews (19,84,85,87–90). This is mainly attributed to their low toxicity and strong T_2 effects (84), which make MNPs promising candidates for use in the early detection and diagnosis of atherosclerosis, cancer, and many other human diseases (91–93). When using as a T_2 contrast agent, which is the common use for MNPs, the efficiency of the magnetic material is measured in terms of the transverse relaxativity (r_2). This parameter is determined by calculating the slope of the plot of $1/T_2$ versus the concentration of the contrast agent (89), with a higher r_2 value associated with a more effective MRI contrast agent (22).

However, the successful achievement of a medical diagnosis using an MRI contrast agent is directly related to the structural properties of the contrast agent, including the size, surface coating, and shape (79). As consequence, the saturation magnetization, colloidal stability, interaction with water molecules, and inhomogeneous induced magnetic field also affect the performance of the contrast agent(19,94,95). The effects of all these variables on r_2 were evaluated in terms of the quantum-mechanical outer-sphere theory(96,97).

When the size of the MNPs is in the motional average regime, which is the case with superparaMNPs, an increase in their dimensions leads to higher r_2 values, as a result of the enhancement of the M_s value (22,89). The surface coating is another crucial factor that influences r_2 . First, the surface coating provides the NPs with colloidal stability, which is a circumstantial requirement for *in vivo* applications. Second, the CA attached to the surface of the NPs can hinder water diffusion, or immobilize nearby water molecules by hydrogen bonds (95). This causes the water molecules to be more significantly influenced by the induced magnetic field, which affects the nuclear proton relaxation and consequently increasing r_2 (95).

Therefore, the synthesis and functionalization steps play a key role in the performance of MRI contrast agents, allowing their physical-chemical properties to be tailored by selecting a favorable methodology. Moreover, the desired implementation of MNPs in clinical usage will require the development of a simplified and fast process that produces NPs with significant physical and chemical properties(98). The most commonly used approach to synthesize and functionalize MNPs is thermal decomposition(85). This method produces crystalline and size monodispersed MNPs. Nevertheless, the process is laborious and time-consuming, with two days sometimes needed because of the preparation and purification requirements(98). For instance, the Fe-oleate complex is prepared on the first day of the procedure, and the second day is used to thermally decompose the Fe-oleate complex and obtain hydrophobic coated MNPs. A third day may even be necessary to perform ligand exchange in order to obtain MNPs with colloidal stability in aqueous solvents(98). Therefore, it is desirable to develop a methodology to overcome these drawbacks of thermal decomposition while simultaneously generating NPs with excellent physical and chemical properties.

Sonochemistry has received a tremendous amount of attention in relation to the synthesis of materials because of its ability to achieve unique hot spots with temperatures greater than 5000 K and a pressure of 1000 atm(59,60,99). Such conditions make this technique distinctive from other conventional methods, and thus make this approach a satisfactory option to the laborious thermal decomposition method. Sonochemistry has already been used to synthesize Fe₃O₄ NPs(64–77). However, in most of the published papers, the process time was still large (60–180 min)(63–66,71,73,75,76,100). Furthermore, although sonochemistry has already been used to functionalize MNPs, there is still a lack of information about its effects in the functionalization of Fe₃O₄ NPs. Moreover, no paper has reported an easy and fast functionalization protocol that can be used with a wide range of CAs. To date, this approach has mainly been used to coat Fe₃O₄ NPs with chitosan, as reported by Szpak *et al.* (100) and, recently, by our group (63).

In the work reported here, we proposed a new, straightforward, and fast methodology to produce functionalized Fe₃O₄ NPs with outstanding physico-chemical properties and the potential to be applied as an MRI contrast agent. It is important to emphasize that the proposed method provides, in just 12 min, Fe₃O₄ NPs exhibiting significant magnetic properties, colloidal stability, and high r_2 values. The CAs used in this work were sodium poly-acrylate (PAANa), trisodium citrate (CIT), sodium oleate (OLNa),

and branched-polyethylenimine (BPEI). Moreover, several characterization techniques were employed to evaluate the structure and magnetic properties of the core, interaction between the CA and Fe_3O_4 , and colloidal stability of the synthesized NPs. Finally, we demonstrated that the synthesized MNPs possessed a high potential to be employed as an MRI contrast agent. Therefore, our results represent a new prospect for obtaining superior-quality functionalized Fe_3O_4 NPs in a simple and rapid manner.

3. OBJECTIVES

3.1 General Objective

- To prove that ultrasound irradiation is a facile, rapid, and efficient approach to synthesize and functionalize Fe₃O₄ NPs with potential biomedical applications.

3.2 Specific Objectives

- To synthesize and functionalize Fe₃O₄ NPs with PAANa, BPEI, OLN_a, and CIT;
- To characterize the obtained NPs using X-ray diffraction (XRD), Mössbauer spectroscopy (MS), transmission electron microscopy (TEM), a vibrating sample magnetometer (VSM), field-cooled (FC) and zero-field-cooled (ZFC) magnetization curves, thermo-gravimetric analysis (TG), Fourier transform infrared spectroscopy (FTIR), and dynamic light scattering (DLS) techniques.
- To evaluate the potential of the functionalized NPs as a contrast agent for MRI.

4. MATERIALS AND METHODS

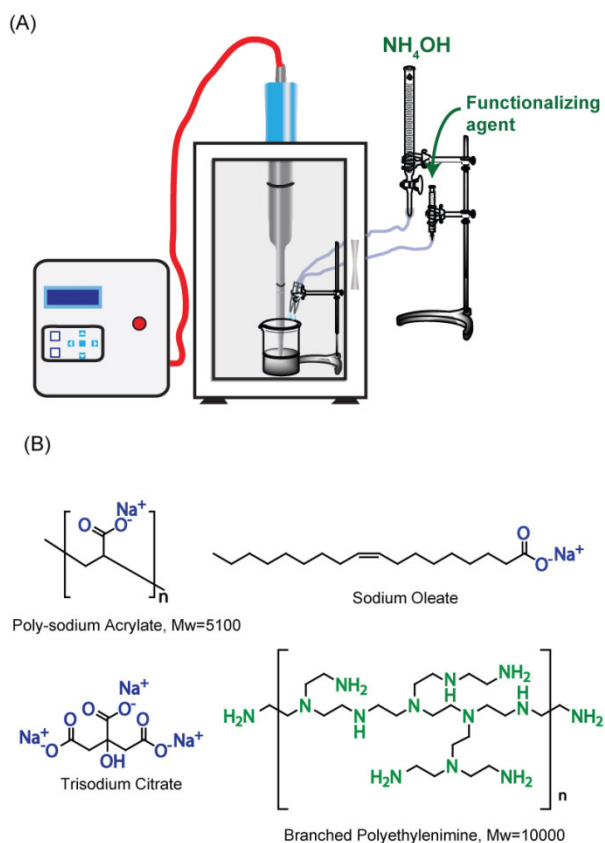
4.1 Chemicals

Iron chloride (III) hexahydrate ($\text{FeCl}_3 \cdot 6\text{H}_2\text{O}$) and iron sulfate heptahydrate ($\text{FeSO}_4 \cdot 7\text{H}_2\text{O}$) were purchased from Vetec Química. PAANa ($M_w = 5100$), BPEI ($M_w = 25000$), CIT, and OLNa (82%) were purchased from Sigma-Aldrich. Ammonium hydroxide (29%) was purchased from Dinâmica Química.

4.2 Synthesis and Functionalization of Fe_3O_4 with PAANa, BPEI, and CIT

The synthesis and functionalization of Fe_3O_4 NPs were performed in a two-step synthesis, using an ultrasound probe (Ultrasonique Desruptor) with a frequency of 20 KHz and 750 W of power. The experimental apparatus is shown in Figure 11 (A). The structures of the CAs used in this work are presented in Figure 11 (B).

Figure 11 – (A) Experimental apparatus used in synthesis and functionalization of MNPs. (B) Structures of CAs used in this work.



Initially, two solutions were prepared, an iron salt solution (solution A) and a CA solution (solution B). Solution (A) contained 1.16 g (4 mmol) of $\text{FeSO}_4 \cdot 7\text{H}_2\text{O}$ and 1.85 g (7 mmol) of $\text{FeCl}_3 \cdot 6\text{H}_2\text{O}$ dissolved in 15 mL of deionized water. Solution B contained 1.0 g of CA in 4.0 mL of deionized water.

First, solution A was sonicated for 4 min until it reached a temperature of 60 °C. Then, 7.0 mL of concentrated NH_4OH was added under sonication using a burette. Thereafter, the color of solution A changed from orange to black, evidencing the formation of Fe_3O_4 NPs, and the reaction medium were sonicated for more 4 min. Finally, solution B was added to the reaction medium, which was kept under sonication for another 4 min. Thus, the ultrasound-assisted synthesis and functionalization of Fe_3O_4 NPs occurred in just 12 min.

To remove the excess NH_4OH and unbounded CA, the resultant NPs were washed several times with distilled water and precipitated with acetone. Finally, the NPs were dispersed in water and centrifuged for 10 min at 3000 rpm to remove the less stable NPs. The remaining functionalized NPs showed colloidal stability in water. Thus, they were stored in deionized water and de-aerated with argon to remove the dissolved oxygen. This procedure was used to generate three samples labeled as $\text{Fe}_3\text{O}_4@PAANa$, $\text{Fe}_3\text{O}_4@BPEI$, and $\text{Fe}_3\text{O}_4@CIT$.

4.3 Functionalization of Fe_3O_4 NPs with OLN_a

The difference between this procedure and the former one is that the CA was dissolved with the iron salt solution. The reactant amounts remained the same. In this procedure, 1.0 g of OLN_a was dissolved in 10.0 mL of deionized water under 60 °C. This solution was added to the iron salt solution (solution A) and sonicated for 4 min. At this point, the reaction medium reached a temperature of 60 °C. Then, 7.0 mL of concentrated NH_4OH was added under sonication, and the reaction medium was sonicated for an additional 8 min.

The NPs were washed with distilled water to remove the excess NH_4OH . Afterward, n-hexane and ethanol were used to wash and precipitate the hydrophobic coated NPs, respectively. This procedure was performed to remove the unbounded OLN_a molecules. Finally, the NPs were dispersed in hexane and centrifuged for 10 min at 3000 rpm to remove the less stable NPs. The NPs were stored in cyclohexane. The ferrofluid generated in this procedure was labeled as $\text{Fe}_3\text{O}_4@OLNa$.

4.4 Characterizations of NPs

The core structure of the obtained NPs was evaluated by XRD using an X'Pert MPD X-ray powder diffractometer (PANalytical, Westborough, USA) with 40 kV and a 30 mA in a scanning range of $2\theta = 20\text{--}80^\circ$. A $\text{CuK}\alpha$ tube was used for the $\text{Fe}_3\text{O}_4\text{@PAANa}$, $\text{Fe}_3\text{O}_4\text{@BPEI}$, and $\text{Fe}_3\text{O}_4\text{@OLNa}$ samples, while a $\text{CoK}\alpha$ tube was employed in the analysis of the $\text{Fe}_3\text{O}_4\text{@CIT}$ sample. The diffraction patterns were obtained using a Bragg–Brentano geometry in the continuous mode with a speed of $0.5^\circ/\text{min}$ and step size of 0.02° (2θ). The Rietveld structure refinement was used to interpret and analyze the diffraction data using the program DBWstools 2.4 (101). The full-width at half maximum (FWHM) of the instrument was calculated with the standard hexaboride lanthanum. The crystallite size of each sample was calculated using Scherrer's equation.

A TEM analysis of the synthesized nanoparticles was performed using a JEOL JEM 1011 (JEOL, Tokyo, Japan) operating at 100 kV and equipped with a CCD camera (Gatan Orius 831). A drop of each aqueous NP suspension was deposited onto a carbon coated Cu grid. Subsequently, the specimens were dried at 60°C overnight before being analyzed. The size distribution curves were obtained by manually measuring the sizes of 200 particles (102), using the software Image J (US National Institutes of Health, Bethesda, Maryland, USA). The polydispersity index for the TEM analysis (PDI_{TEM}) was calculated as reported in the literature (103).

The Mössbauer spectroscopy (MS) data were recorded at room temperature (300 K) with a FAST (ConTec) Mössbauer system spectrometer using the transmission geometry. A ^{57}Co radioactive source was used. The data analysis was performed using the NORMOS program written by R. A. Brand (distributed by Wissenschaftliche Elektronik GmbH, Germany). The isomer shifts (δ) relative to $\alpha\text{-Fe}$ were found at room temperature.

Magnetic measurements were carried out on powder samples using the superconducting quantum interference device (SQUID) magnetometer SQUID-VSM and vibrating sample magnetometer (VSM) EV9 manufactured by Quantum Design and Lot-Oriel, respectively. Before making these measurements, the particles were dried overnight in vacuum at room temperature, ground using an agate mortar and pestle, and finally placed in gelatin capsules for the measurements. Hysteresis loops were obtained at 300 K by applying a magnetic field of up to $\pm 20,000$ Oe.

The presence of the CAs on the surface of the NPs was confirmed by FTIR. The samples were ground in an agate mortar and pressed into discs of KBr at a ratio of 1:10 (sample:KBr). The spectra were recorded in vacuum to avoid interference from water and carbon dioxide using a Vertex 70v. The range used was 4000–400 cm^{-1} , with a resolution of 2 cm^{-1} and 128 scans.

The number of CAs and how they were organized on the surface of the NPs were evaluated using a thermogravimetric analysis (TGA). The measurements were performed using a Mettler Toledo TGA/simultaneous differential thermal analysis (TGA/SDTA) 851e machine. A nitrogen atmosphere was used (50 cm^3/min), with a heating rate of 10 $^\circ\text{C}/\text{min}$, sample mass of 10 mg, and temperature programs in the range of 25–800 $^\circ\text{C}$. The method previously reported in the literature was used for the quantitative analysis of the CA molecules (104).

The hydrodynamic size of the NPs in solution was measured in DLS experiments using a Malvern zetasizer NS 3601 at 25 $^\circ\text{C}$. The DLS measurements were performed on a diluted solution of the NPs (0.066 mg/mL), with a single scattering angle of 173 $^\circ$. The hydrodynamic size of the synthesized samples was further analyzed using a phosphate buffer with a pH of 7.4 (PB 7.4) and that with a high salt concentration and a pH of 7.4 (PBS 7.4), which were prepared as previously reported (105). The DLS sizes of the samples were expressed as Z-average values, and the polydispersity index (PDI_{DLS}) values were calculated using the cumulate method. Five measurements were performed for each sample. The surface zeta potential (ζ) of each sample was measured using the same machine at 25 $^\circ\text{C}$. The ζ value was also measured using the PB 7.4 as a solvent.

4.5 Relaxativity Measurements and MRI Weighted Images

Four aqueous dilutions with different nanoparticle concentrations (between 0 and 0.25 mM Fe) were prepared for each sample. To conduct measurements in the Minispec (1.41 T), 200 μL of each water-dispersed sample was prepared in a relaxometer tube. The Fe concentrations of the solutions were calculated using an inductively coupled plasma-atomic emission spectroscopy (ICP-AES) analysis.

For the phantom measurements, samples at 100 and 200 μM were dissolved in 200 μL of water in 300 μL tubes. All of the MR images of the phantoms were acquired using a 256 \times 252 image matrix, a 60 \times 60 mm FOV, three slices with a slice thickness of 1 mm,

and a 1 mm slice gap. For the T2-weighted imaging, a fast spin echo (FSE) sequence with the following parameters was used: TE = 11 ms, TR = 12,000 ms, and NA = 32. For the T1-weighted imaging, an FSE sequence with the following parameters was used: TE = 11 ms, TR = 720 ms, and NA = 32.

5. RESULTS AND DISCUSSION

5.1 Synthesis and Magneto-fluid Response

Sonochemistry has been proven to be a powerful tool for preparing a wide range of materials, as presented in two reviews (59,60). The interesting feature of this methodology is that under ultrasound irradiation, the alternating acoustic waves create bubbles in an oscillating manner. These waves make the bubbles grow to a certain size and then collapse, releasing a concentrated burst of energy within a short time. The energy is so localized that the collapsing bubbles can quickly increase the temperature up to 5000 K and reach pressures as large as 1000 bar (13,59,106). These conditions are capable of speeding up chemical reactions (68). We believe that these events occurred during the synthesis and functionalization steps of the NPs reported here. Figure 12 (A) summarizes the timeline of all the events that occur and the possible physical mechanisms underlying the experimental stages of the NP synthesis and functionalization. The mechanism presented in Figure 12 (A) has been adapted from a previously reported route describing the sonochemical synthesis of hydroxyapatite NPs (107–109).

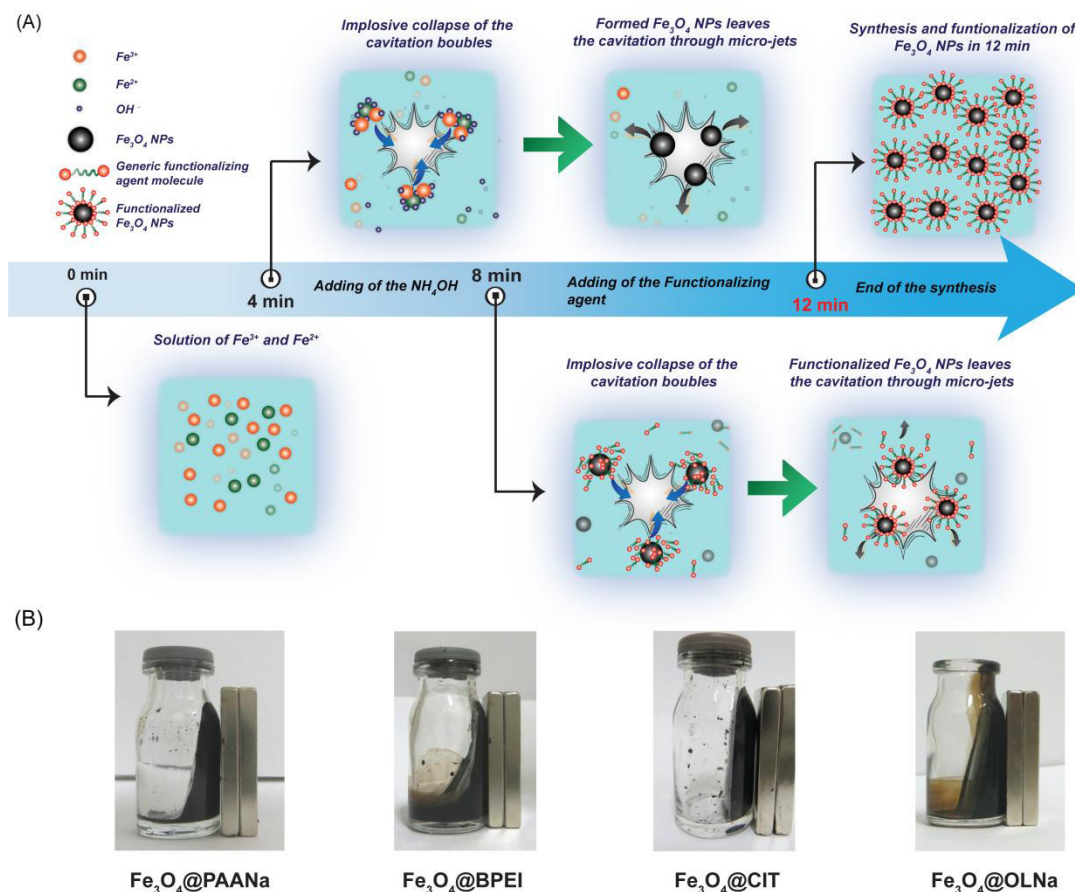
During the first 4 min of the synthesis, a mixture of Fe^{2+} and Fe^{3+} was sonicated to reach a temperature of ~ 60 °C, after which concentrated NH_4OH was added to the reaction medium. Then, ferrous, ferric, and hydroxide ions were adsorbed on the cavitation bubbles, followed by their implosive collapse. This event induced a collision between the ions at high temperatures and pressures, which subsequently led to the formation of Fe_3O_4 NPs (Figure 12 (A)). The reaction medium was kept under sonication for more than 4 min to allow the particles to grow to the desired size and crystallinity. At this time, the selected CA was added, and the reaction was left under sonication for an additional 4 min, which produced CA-functionalized Fe_3O_4 NPs (see Figure 12 (A)).

We believe that the sonochemical component was essential for the successful CA- Fe_3O_4 interaction and, consequently, for the achievement of the particle functionalization, in addition to the synthetic efficacy.

The presence of a CA during the nucleation of the Fe_3O_4 NPs hindered the NP growth, which led to amorphous MNPs and low M_s (110). Therefore, we decided to add the hydrophilic CAs (PAANa, CIT, and BPEI) after the NH_4OH solution. However, when the hydrophilic CAs were added, the Fe_3O_4 NPs still had enough surface energy to be successfully functionalized. Thus, this strategy made it possible to obtain NPs with excellent

magnetic properties and colloidal stability in aqueous solvents, which are two key factors for biological applications.

Figure 12– (A) Timeline of synthesis and functionalization of MNPs, sequence for addition of reactants, and proposed mechanism of sonochemical synthesis and functionalization of MNPs. (B) Magneto-fluid response of the samples herein synthesized.



Source: Present author

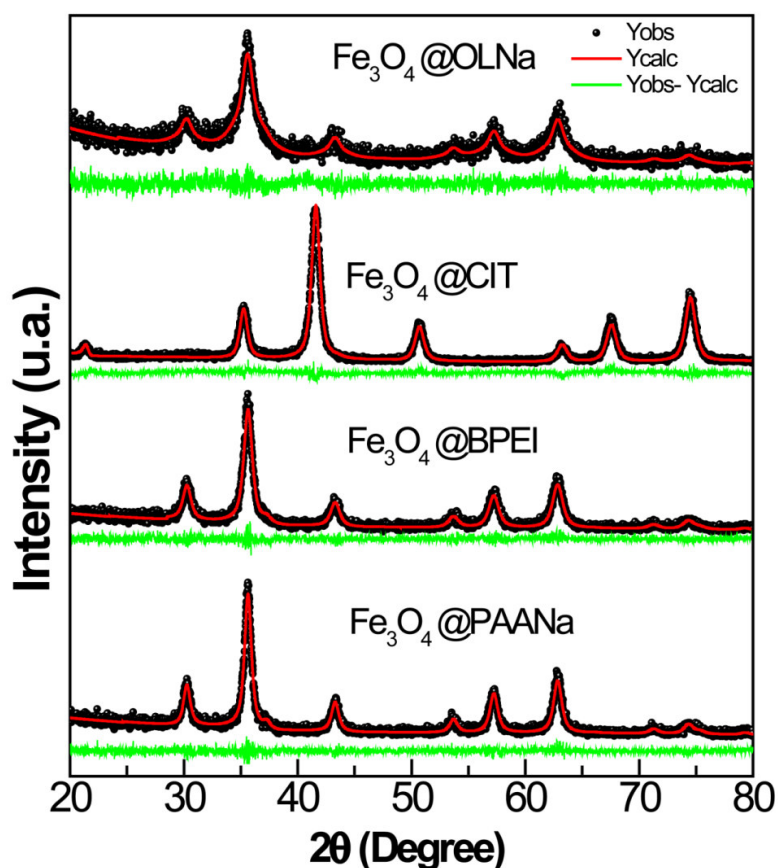
The colloidal stability of the synthesized NPs was first qualitatively evaluated by their magneto-fluid response, as shown in Figure 12 (B). The images show that the whole solution was attracted to the magnet, rather than simply the solid particles. Thus, we could confirm that the synthesized NPs possessed a magneto-fluid response, which is one of the characteristics of ferro-fluids and indicated that the functionalization was achieved (111).

5.2 Structural and Magnetic Characterizations

5.2.1 XRD

The lattice structure and composition of the NPs were evaluated using XRD combined with Rietveld structural refinement. The diffraction patterns of the prepared samples are shown in Figure 13. A Rietveld analysis was performed to acquire additional information about the structures of the synthesized samples. The results are summarized in Table 2. To express the quality of the refinement, the percentage of obtained errors (R_{WP}) and goodness of fit (S) are reported (Table 2). The data were found to be in the range of a refinement of good quality (112).

Figure 13 – XRD patterns of obtained NPs. The black dots and red line show the experimental and calculated data, respectively. The green line shows the difference between these two parameters.



Source: Present author

Table 2 – Parameters extracted from Rietveld refinement and average size of NPs calculated using TEM.

Sample	XRD				TEM	
	Lattice parameters (a) (Å)	Rwp (%)	S	Average crystallite size (nm)	Average particle size (nm)	PDI _{TEM}
Fe ₃ O ₄ @PAANa	8.372	15.41	0.87	12.7 ± 0.22	11 ± 3	0.293
Fe ₃ O ₄ @BPEI	8.374	15.18	0.89	10.2 ± 0.16	10 ± 3	0.280
Fe ₃ O ₄ @CIT	8.360	13.75	1.01	12.9 ± 0.2	11 ± 3	0,256
Fe ₃ O ₄ @OLNa	8.362	15.48	0.89	7.0 ± 0.09	9 ± 3	0.284

Source: Present author

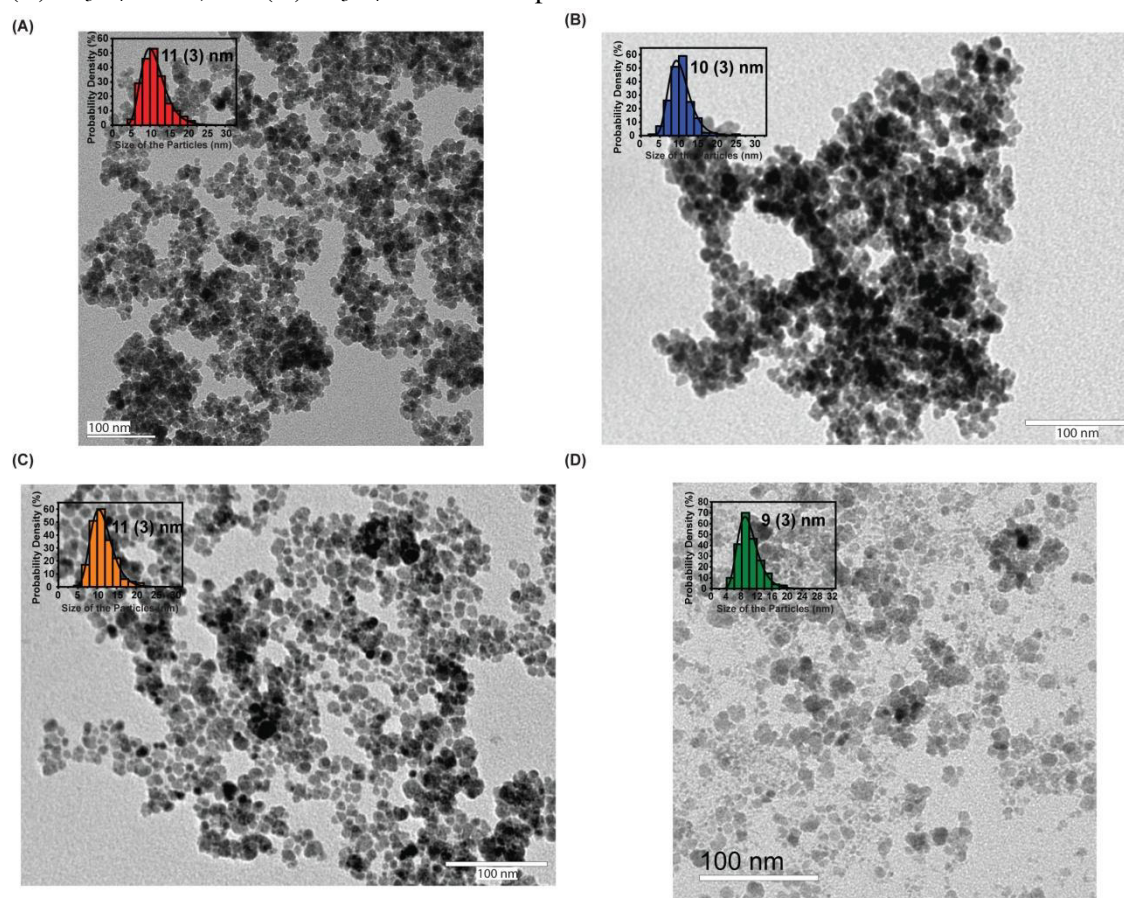
All of the diffraction peaks indicated that the core structures of the NPs were composed of a cubic inverse spinel structure Fd3m (ICSD code: 84611)(113), which is characteristic of Fe₃O₄. Moreover, the crystalline and nanosized components of the obtained samples are evidenced by the background and broad peaks of the patterns presented in Figure 13. Such features are attenuated in the pattern of the Fe₃O₄@OLNa sample (Figure 13), in which OLNa was added before the formation of Fe₃O₄ crystals. Therefore, it is reasonable to assume that the carboxylate groups of OLNa molecules tended to strongly chelate iron ions, thus slowing or hindering the growth of the particles, and leading to smaller and even amorphous NPs (110).

The cubic cell parameter (*a*) values for all the samples are in agreement with that of nanosized magnetite (27,114,115) (Table 2). However, *a* value changes were found for the NPs functionalized with different CAs. This indicates that the CA slightly affected the stoichiometry of the Fe₃O₄ NPs. Lu *et al.* reported similar results when evaluating the effects of the surfactants on the structure of Fe₃O₄ NPs (115). Furthermore, the crystallite sizes of the NPs were calculated using Scherrer's equation, and the values are shown in Table 2. These values range from 7.0 to 12.7 nm for the Fe₃O₄@OLNa to Fe₃O₄@CIT samples, respectively. The smallest crystallite size obtained for the Fe₃O₄@OLNa NPs was confirmed by its XRD pattern and the manner that the synthesis proceeded.

5.2.2 TEM

The morphology and structure of the NPs were evaluated using TEM. The micrographs and size-distribution curves of the $\text{Fe}_3\text{O}_4@$ PAANa, $\text{Fe}_3\text{O}_4@$ BPEI, $\text{Fe}_3\text{O}_4@$ CIT, and $\text{Fe}_3\text{O}_4@$ OLNa samples are shown in Figure 14. Additionally, the average diameters of the NPs are listed in Table 2. The TEM micrographs show that the synthesized NPs possessed a sphere-like morphology, which is expected when the precipitation of Fe_3O_4 NPs is performed using iron salts and ammonium hydroxide (36,116). The average size of the $\text{Fe}_3\text{O}_4@$ PAANa, $\text{Fe}_3\text{O}_4@$ BPEI, $\text{Fe}_3\text{O}_4@$ CIT, and $\text{Fe}_3\text{O}_4@$ OLNa samples were 11 ± 3 , 10 ± 3 , 11 ± 3 , and 9 ± 3 nm, respectively, which were close to the values calculated using XRD (Table 2). Furthermore, the sonochemistry approach proposed in this work produced NPs with a narrow size-curve distribution, as evidenced by the PDI_{TEM} values (Table 2). This characteristic is particularly significant in relation to their biological application as a contrast agent (117).

Figure 14 – TEM micrographs and size-distribution curves of (A) $\text{Fe}_3\text{O}_4@$ PAANa, (B) $\text{Fe}_3\text{O}_4@$ BPEI, (C) $\text{Fe}_3\text{O}_4@$ CIT, and (D) $\text{Fe}_3\text{O}_4@$ OLNa samples.



Source: Present author

5.2.3 Mössbauer spectroscopy

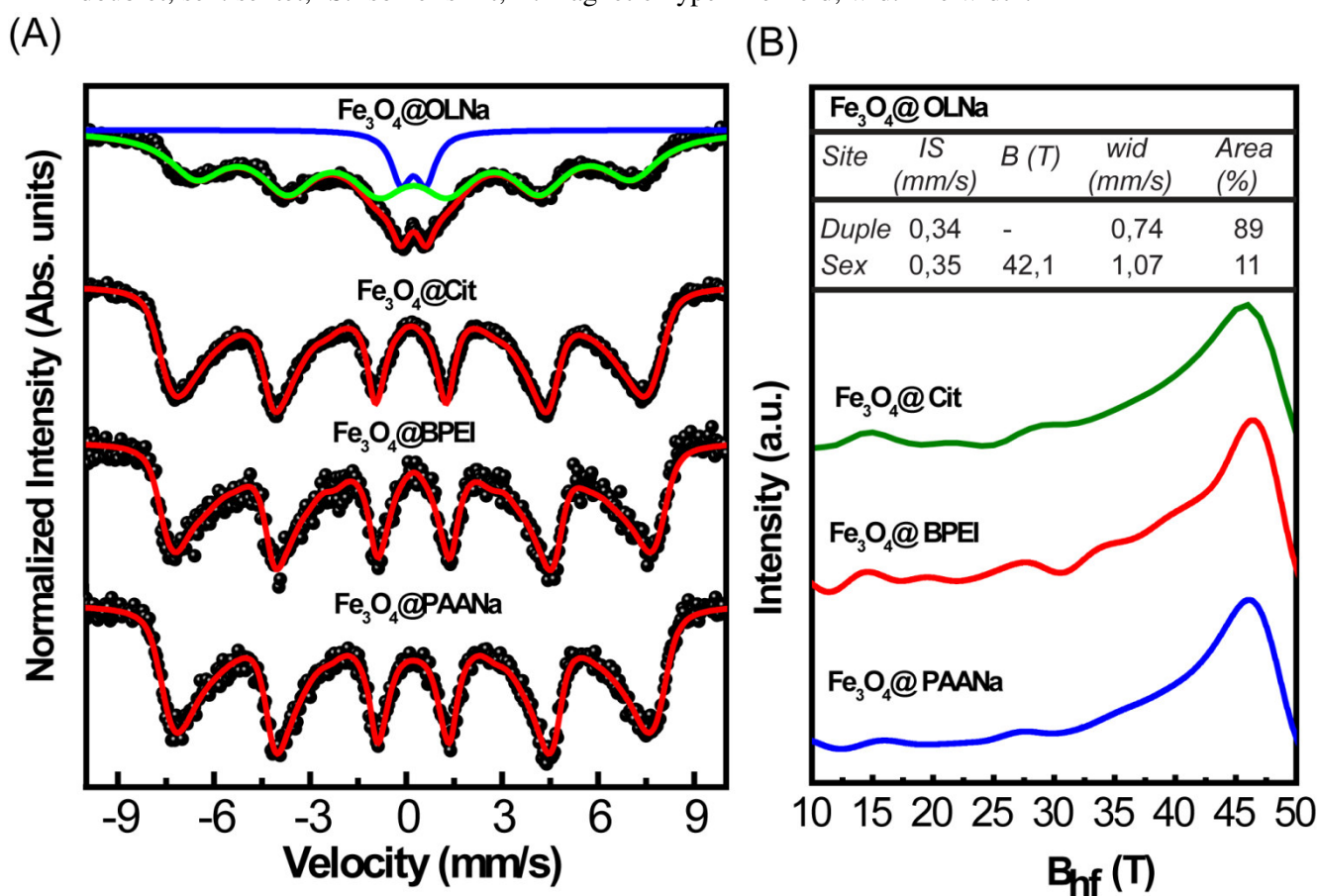
MS has been extensively used to study iron-containing materials because the MS spectra contain information about the structure, including the electronic and magnetic properties of the studied material (118). The MS spectra of all the samples are shown in Figure 15 (A). The $\text{Fe}_3\text{O}_4@PAANa$, $\text{Fe}_3\text{O}_4@BPEI$, and $\text{Fe}_3\text{O}_4@CIT$ samples showed broadened ferrimagnetic sextets. Therefore, a magnetic hyperfine field distribution was used to fit the measured spectra. This distribution is shown in Figure 15 (B). On the other hand, the $\text{Fe}_3\text{O}_4@OLNa$ sample showed a well-resolved paramagnetic doublet and ferrimagnetic sextet. Thus, a distribution of the hyperfine parameters by site was chosen (Figure 15 (A, B)).

First, it is important to mention that the MS spectrum of the bulk Fe_3O_4 at room temperature was composed of two well-resolved ferri- or ferromagnetic sextets, which corresponded to Fe^{3+} in tetrahedral sites and Fe^{3+} and Fe^{2+} on octahedral sites. When the size of the particles decreased, the sextets exhibited broadened lines as a result of the presence of superparamagnetic fluctuations (119). A further decrease in the size of the particles led to a change in the MS spectrum. Specifically, the broad sextet became a paramagnetic doublet, which is characteristic of superparamagnetic nanoparticles (120). Therefore, we believe that the $\text{Fe}_3\text{O}_4@PAANa$, $\text{Fe}_3\text{O}_4@BPEI$, and $\text{Fe}_3\text{O}_4@CIT$ samples were in the transition to the superparamagnetic regime during the measurement in the MS experiment. Moreover, the profiles of the spectra of these particles were similar to those reported in the literature for 8–20 nm Fe_3O_4 NPs (56,115,118,119,121), which were in perfect agreement with the dimensions of the particles grown in this study as determined via XRD and TEM.

Conversely, because of the clear presence of a doublet in the MS spectrum, it is possible to assert that most of the population of particles in the $\text{Fe}_3\text{O}_4@OLNa$ sample were in a superparamagnetic regime (Figure 15 (A, B)). This was corroborated by the area of the calculated doublet (89%), which was greater than that of the sextet (11%), as shown in the top region of Figure 15 (B). The sextet could be assigned to a smaller fraction of particles, which were larger and evidently in the transition between the ferrimagnetic and superparamagnetic regimes. However, some authors have affirmed that this sextet might be an indication of the presence of supra-structures assembled by dipolar interactions (122). Additionally, based on the smaller size of the NPs observed by XRD and TEM, the existence of a paramagnetic doublet in the MS spectrum for the $\text{Fe}_3\text{O}_4@OLNa$ sample could be expected. The other calculated hyperfine parameters included the isomer shift (IS) and line width of the doublet,

which had values of 0.34 mm/s and 0.74 mm/s, respectively, along with those for the sextet, which were determined to be 0.35 mm/s and 1.07 mm/s, respectively. In addition, the hyperfine field for the sextet was found to be 42.1 T. These values were in agreement with those for the 6 nm Fe_3O_4 NPs reported by Mikhaylova *et al.* (123).

Figure 15 – (A) MS spectra of synthesized samples. The black dots and red lines represent the experimental and calculated data, respectively. Furthermore, for the Fe_3O_4 @OLNa sample, the green and blue lines are the site distributions for the populations of NPs under ferri- and superparamagnetic regimes, respectively. (B) The image shows the hyperfine field distribution curves of each sample. The table at the top of the image summarizes the data extracted from the site distribution. Duple: doublet; sex: sextet; IS: isomer shift; B: magnetic hyperfine field; wid: line width.

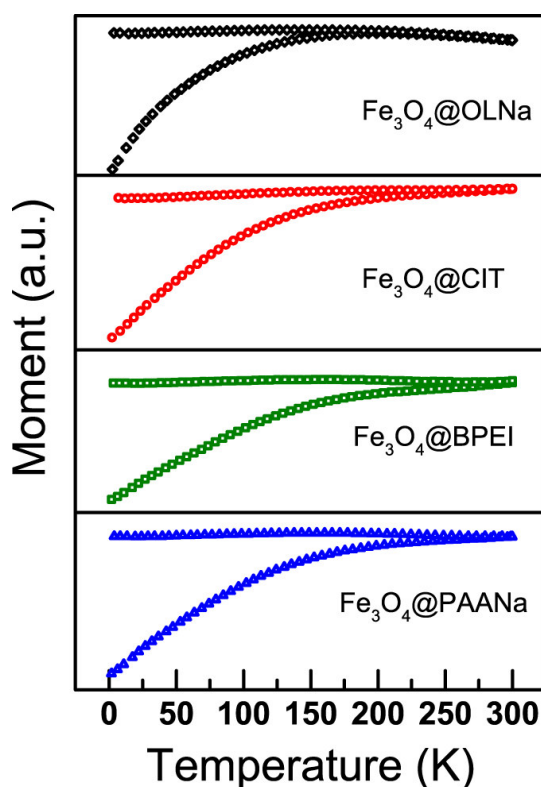


Source: Present author

5.2.4 Magnetic measurements

The magnetic features of the synthesized NPs were determined through the ZFC and FC curves, which are shown for all the functionalized samples in Figure 16. Evidence of the strong magnetic dipolar particle interaction can be seen in the flat profile of the FC curves (116). This behavior is more accentuated for the $\text{Fe}_3\text{O}_4@PAANa$, $\text{Fe}_3\text{O}_4@BPEI$, and $\text{Fe}_3\text{O}_4@CIT$ samples, which possess large particle sizes and crystallinities, as evidenced by the XRD and TEM results. The ZFC curves for these samples do not have maximums, indicating that the superparamagnetic blocking temperatures (T_B) for these samples are greater than 300 K (116). In contrast, the ZFC curve for the $\text{Fe}_3\text{O}_4@OLNa$ sample has a maximum of 196 K, which corresponds to its T_B . These results are in agreement with the Stoner–Wohlfarth theory (124), which states that $T_B = KV/25k_B$, where K is the effective magnetic anisotropy constant, V is the volume of the NPs, and k_B is the Boltzmann constant. The agreement with this theory is a result of the smaller diameters for $\text{Fe}_3\text{O}_4@OLNa$ (Table 2). Thus, according to the FC and ZFC curves, among the synthesized samples, the only one that possesses a T_B below room temperature is $\text{Fe}_3\text{O}_4@OLNa$, in agreement with the MS results (Figure 15).

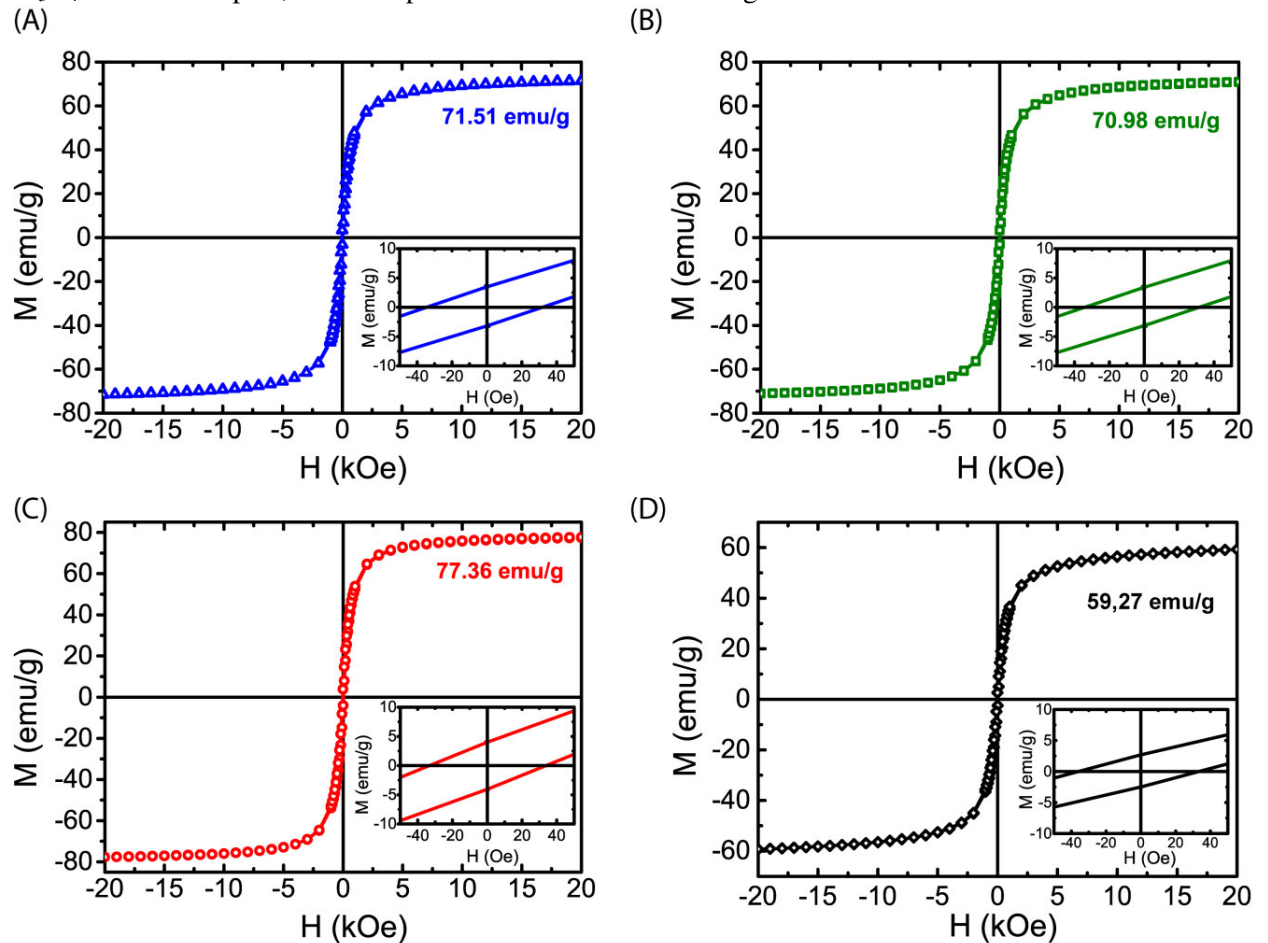
Figure 16 – ZFC and FC magnetization curves for functionalized NPs prepared in this work.



Source: Present author

The magnetic hysteresis loops of the synthesized samples at 300 K are shown in Figure 17 A–D. The low-field regions of the curves are shown in the insets, which reveal small hysteresis loops. Using these data made it possible to calculate the M_s , remnant magnetization (M_r), and coercivity field (H_C) values. For the $\text{Fe}_3\text{O}_4@PAANa$, $\text{Fe}_3\text{O}_4@BPEI$, $\text{Fe}_3\text{O}_4@CIT$, and $\text{Fe}_3\text{O}_4@OLNa$ samples, the M_s values were 71.51, 70.98, 77.36, and 59.27 emu/g, respectively. The M_r values were 3.45, 3.43, 3.96, and 2.70 emu/g, respectively. The H_C values were 34.27, 33.9, 33.21, and 35.26 Oe, respectively. Clearly the M_s values for our samples were smaller than the bulk value (92 emu/g). This was due to the existence of a surface spin disorder layer, which substantially decreased the M_s value for particles with nanometer dimensions (125).

Figure 17 – VSM curves of (A) $\text{Fe}_3\text{O}_4@PAANa$, (B) $\text{Fe}_3\text{O}_4@BPEI$, (C) $\text{Fe}_3\text{O}_4@CIT$, and (D) $\text{Fe}_3\text{O}_4@OLNa$ samples; insets: expanded views of low-field regions.



Source: Present author

Interestingly, the H_C values for all the samples were very close, even for the $\text{Fe}_3\text{O}_4@\text{OLNa}$ sample, which had a T_B below room temperature, duplet in the MS spectra, and smaller mean particle diameter than the other synthesized samples. Thus, it was expected to have a smaller H_C value. This difference might have been a result of the intrinsic contribution of the experimental machine. Therefore, we believe that the absence of maximums in the ZFC curves for the $\text{Fe}_3\text{O}_4@\text{PAANa}$, $\text{Fe}_3\text{O}_4@\text{BPEI}$, and $\text{Fe}_3\text{O}_4@\text{CIT}$ samples was a result of the strong dependence of T_B on the particle diameter (proportional to D^3) (126).

Our samples certainly possessed large M_s values relative to other functionalized or non-functionalized Fe_3O_4 NPs with comparable or larger core sizes synthesized using different protocols (58,117,127–131). For instance, Wu *et al.* obtained 10.9 nm CIT-coated Fe_3O_4 NPs with an M_s value of 52.38 emu/g using a hydrothermal method (117). Furthermore, Calatayud *et al.* used an oxidative hydrolysis method to prepare PAANa- and BPEI-coated Fe_3O_4 NPs with diameters of 32 and 25 nm, respectively, and M_s values of 54.0 and 51.0 emu/g, respectively (128).

The enhancement of the M_s values for our samples could be attributed to the presence of the CAs on the surface, which increased the crystallinity of the particles by binding the organic compound with Fe atoms at the surface (132). Thus, the successful functionalization of the Fe_3O_4 NPs (see Figure 18 in section 5.3.1) is a reasonable explanation for the large M_s values. However, this effect is more significant in NPs with sizes smaller than 10 nm (133). Thus, we assume that the effect of the CA did not play a major role in the M_s enhancement.

We believe that the major factor contributing to the remarkable M_s values was the ultrasonic irradiation used in the synthesis of the NPs. As previously mentioned, the implosive collapse of the cavitation bubbles generated high energy levels, which increased the reaction rates, leading to NPs with higher crystallinity and consequently greater M_s values. It is important to remember that the M_s value significantly affects the transverse relaxativity of an MRI contrast agent. It is worth mentioning that one of the problems with surface coating MNPs is the reduction of their magnetism due to the presence of non-magnetic compounds (98). This drawback was overcome using the methodology proposed in this work to obtain coated NPs with excellent magnetic properties.

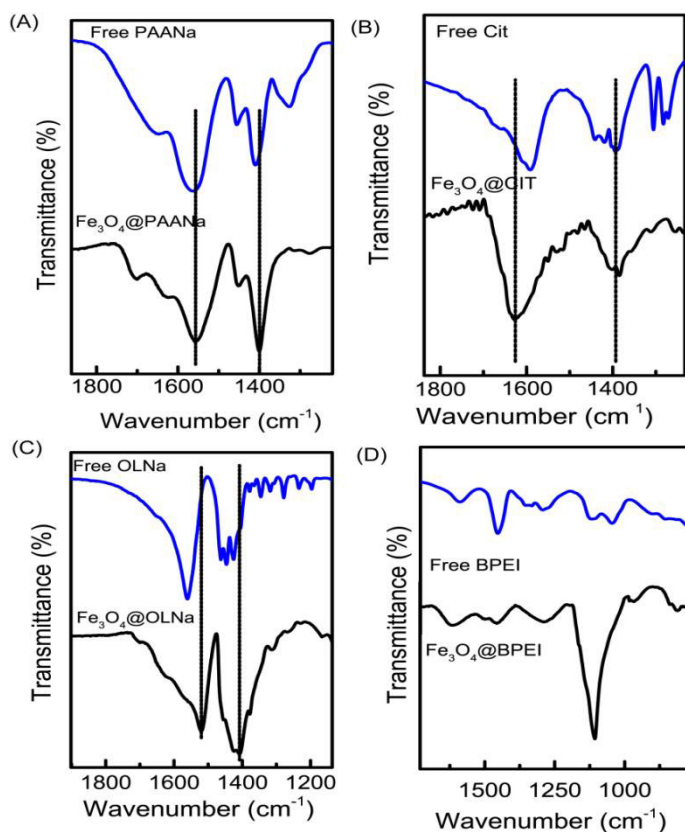
5.3 Coating

In this work, FTIR and TGA were used to study the passivating layer of the functionalized NPs. FTIR was used to evaluate the effectiveness of the sonochemistry approach in functionalizing Fe_3O_4 with PAANa, CIT, BPEI, and OLNa. TGA was used to determine the exact amount of CA molecules present on the Fe_3O_4 NP surface.

5.3.1 FTIR

Figure 18 (A–D) shows the FTIR spectra of the functionalized samples and free CA molecules. For the sake of clarity, only the wavenumber range of interest is presented. The full spectra of the functionalized samples, free CAs, and non-functionalized Fe_3O_4 can be found in appendix 1. All of the functionalized samples revealed two bands between 400 and 800 cm^{-1} attributed to the stretching of the Fe–O bond in tetrahedral and octahedral sites (113). The other bands are characteristics of the CA ligands.

Figure 18 – FT-IR spectra of (A) Fe_3O_4 @PAANa, (B) Fe_3O_4 @CIT, (C) Fe_3O_4 @OLNa, and (D) Fe_3O_4 @BPEI samples. For each sample, the spectra of the functionalized NPs and free CA molecules are shown.



Source: Present author

Regardless of the type of ligand, in all three cases (PAANa, CIT, and OLNa), the anchoring of the CA onto the magnetic core occurred through carboxylate groups. Therefore, the spectra of these three samples mainly show two vibrational modes in the regions of 1300–1500 cm^{-1} and 1550–1700 cm^{-1} , which are related to the symmetric (ν_{SyCO}) and asymmetric (ν_{assyCO}) C–O stretching modes, respectively (Figure 18 (A–C)). Moreover, the wavenumbers of these bands changed after the functionalization as a result of the interaction with the Fe_3O_4 surface (134).

The carboxylic acid (or carboxylate) groups can bind oxide surfaces through "outer-sphere interaction" and/or "inner-sphere interaction" (135). In the first case, this interaction occurred through the H-bond with the –OH groups present on the surface of the oxides (135). In contrast, in the second case, the interaction took place via coordination bonds between the metal and –COOH (or carboxylate) groups (135).

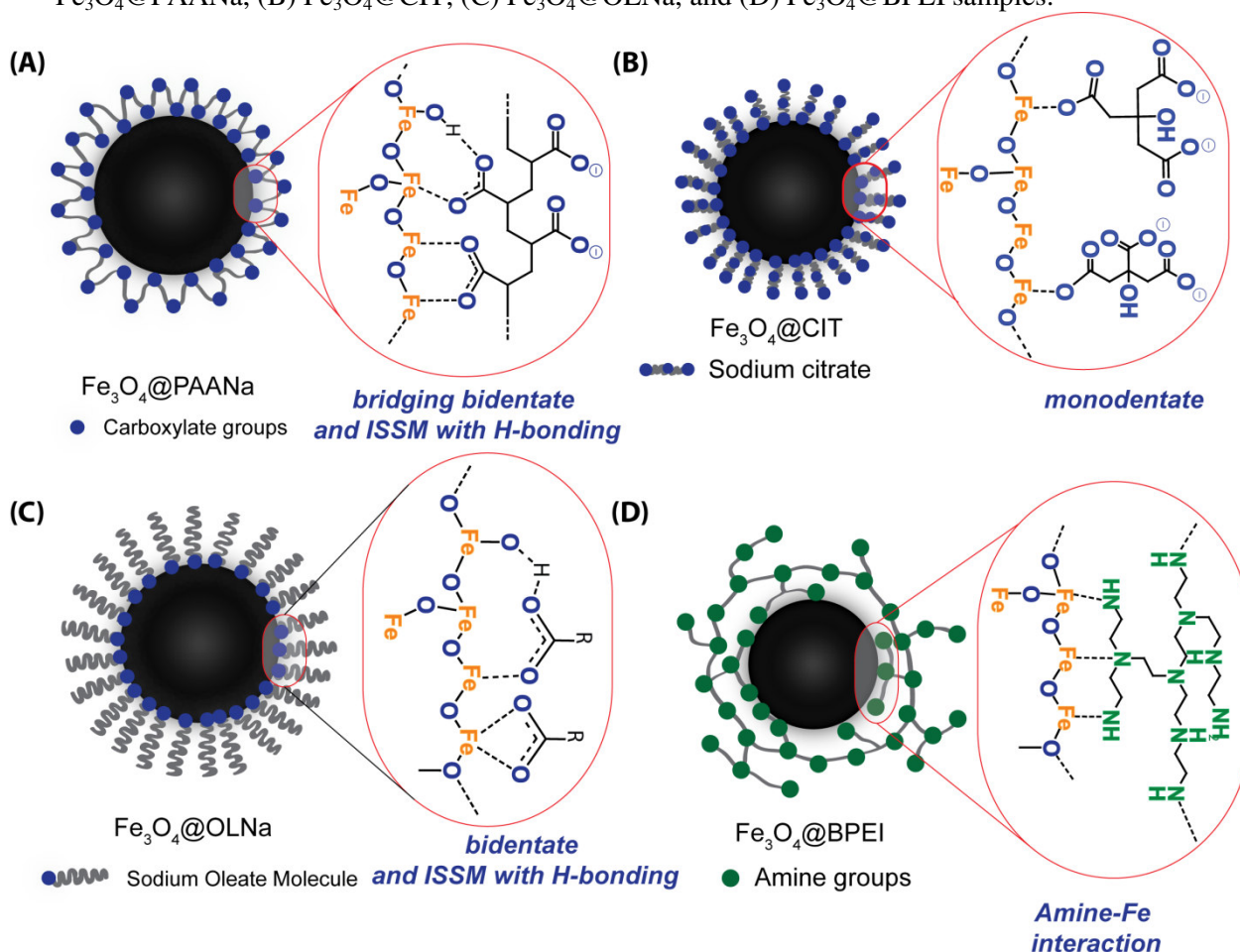
Traditionally, the splitting ($\Delta_{\nu\text{CO}}$) between the ν_{SyCO} and ν_{assyCO} vibrational modes is employed to specify the interaction configuration of carboxylate groups in surface oxides (134,136–140). This method states that monodentate binding occurs if $\Delta_{\nu\text{CO}} > 200 \text{ cm}^{-1}$, whereas bidentate binding occurs when $\Delta_{\nu\text{CO}} < 110 \text{ cm}^{-1}$, and a bridging bidentate better describes the carboxylate-metal coordination when $140 < \Delta_{\nu\text{CO}} < 200 \text{ cm}^{-1}$ (137,139,141,142). This approach is based on the $\Delta_{\nu\text{CO}}$ values for the bulks of several coordination compounds, the structures of which were confirmed by XRD (143). Hence, an extrapolation must be performed to apply this approach to functionalized NPs. However, in the work of Lens *et al.*, the $\Delta_{\nu\text{CO}}$ correlation approach agreed with quantum-chemical calculations for the functionalization of ZnO NPs (139).

For our samples, the $\Delta_{\nu\text{CO}}$ values were 158, 243, and 97 cm^{-1} for $\text{Fe}_3\text{O}_4@$ PAANa, $\text{Fe}_3\text{O}_4@$ CIT, and $\text{Fe}_3\text{O}_4@$ OLNa, respectively. These values indicated that the types of interaction in the synthesized samples were the bridging bidentate, monodentate, and bidentate, respectively, as illustrated in Figure 19 (A–C).

However, Chernyshova *et al.* performed a comprehensive spectroscopic and theoretical study that found numerous drawbacks for the $\Delta_{\nu\text{CO}}$ correlation approach (144). The authors reported that fatty acids adsorbed onto iron oxides as a mixture of an inner-sphere monodentate mononuclear (ISSM) complex with H-bonded second carboxylate oxygen and an outer-sphere complex (OS hydration-shared complex). In our case, we could not exclude their findings, but a theoretical study must be performed to confirm the exact interaction that

occurred in our NPs, which was not the purpose of this work. A fact that we can correlate with our results is the authors' attribution of a shoulder below 1720 cm^{-1} and above 1696 cm^{-1} to an ISSM complex with H-bonded second carboxylate oxygen ($\text{C}=\text{O}\cdots\text{H}$). This band is seen in the $\text{Fe}_3\text{O}_4@\text{PAANa}$ and $\text{Fe}_3\text{O}_4@\text{OLNa}$ samples at 1706 cm^{-1} and 1702 cm^{-1} , respectively.

Figure 19 – Model of interactions between CA molecules and Fe ions of IONPs in (A) $\text{Fe}_3\text{O}_4@\text{PAANa}$, (B) $\text{Fe}_3\text{O}_4@\text{CIT}$, (C) $\text{Fe}_3\text{O}_4@\text{OLNa}$, and (D) $\text{Fe}_3\text{O}_4@\text{BPEI}$ samples.



Source: Present author

In summary, based on our FTIR results, we deduce that the PAANa, CIT, and OLNa are bound with Fe_3O_4 through the bridging bidentate, monodentate, and bridging forms, respectively (see Figure 19 (A–C)). Moreover, for the $\text{Fe}_3\text{O}_4@\text{PAANa}$ and $\text{Fe}_3\text{O}_4@\text{OLNa}$ samples, the ISSM complex with H-bonded second carboxylate oxygen is also expected, as shown in Figure 19 (A and C).

The analysis of the $\text{Fe}_3\text{O}_4@\text{BPEI}$ sample showed different results because the BPEI was anchored to the Fe_3O_4 through amine groups. The spectrum of $\text{Fe}_3\text{O}_4@\text{BPEI}$ is shown in Figure 18 (D). For this sample, the vibrational mode at 1106 cm^{-1} can be

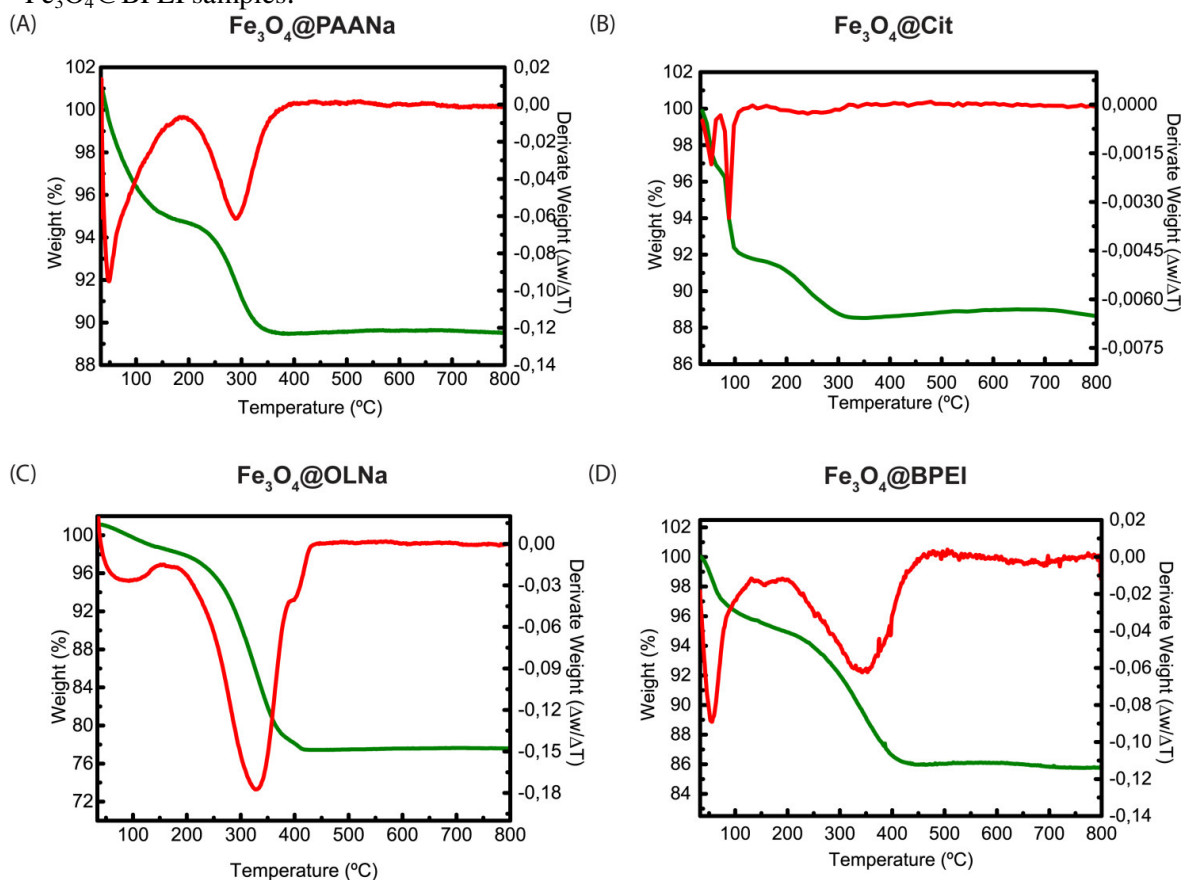
highlighted. This band is related to the C–N stretching (145) and is not found with the same intensity and shape in the spectrum of free BPEI (Figure 18 (D)). Additionally, Bennett *et al.* (146,147) reported that ammine and alkyamine complexes with iron possess a very strong vibrational mode in the region near 1150 cm^{-1} , which was also seen in the spectrum of the $\text{Fe}_3\text{O}_4\text{@BPEI}$ sample. Thus, the increase in the C–N stretching indicates that a chemical interaction occurred between the BPEI and Fe cations present in Fe_3O_4 structure. In order to further confirm this, we measured the FTIR spectrum of a mixture of iron cations (Fe^{2+} and Fe^{3+}) and BPEI, as shown in appendix 2. The spectrum of this mixture also presented a band in the region of 1110 cm^{-1} , just as in the spectrum of the functionalized NPs. Therefore, we could affirm that the interaction between the amino groups of BPEI and Fe_3O_4 occurred through inner sphere coordination, as shown in Figure 19 (D).

Thus, based on our FTIR results, we can only make assumptions about the interactions that occurred between the CA and Fe_3O_4 , as shown in Figure 19. However, we can state that the sonochemistry approach provided sufficient conditions to establish a coordination interaction between the CA and Fe_3O_4 , because of the high energy induced by the implosive collapse of the cavitation bubbles.

5.3.2 TGA

The amount of CAs on the surface of the Fe_3O_4 was assessed using TGA. All of the TGA data are shown in Figure 20 (A–D). The TGA data for the free CAs are shown in appendix 3. All of the samples had similar weight loss profiles for two events. The first was in the range of $37\text{--}190\text{ }^\circ\text{C}$ and was the result of the desorption of physically adsorbed water. The second, and more significant, was observed at temperatures higher than $200\text{ }^\circ\text{C}$, and was the result of the thermal decomposition of the CA molecules. The second event was used to calculate the amount of CA. The values for the $\text{Fe}_3\text{O}_4\text{@PAANa}$, $\text{Fe}_3\text{O}_4\text{@CIT}$, $\text{Fe}_3\text{O}_4\text{@OLNa}$, and $\text{Fe}_3\text{O}_4\text{@BPEI}$ samples were 10.55, 15.72, 29.3, and 10.07%, respectively. Furthermore, the presence of a single event due to the decomposition of the organic matter suggests that the functionalized NPs possessed no weakly bound CA molecules (148). This feature is required for biological applications, because the free CA can induce side effects in patients (33).

Figure 20 – TGA and DTG data for (A) $\text{Fe}_3\text{O}_4@PAANa$, (B) $\text{Fe}_3\text{O}_4@CIT$, (C) $\text{Fe}_3\text{O}_4@OLNa$, and (D) $\text{Fe}_3\text{O}_4@BPEI$ samples.



Source: Present author

It is worth mentioning that the synthesis and functionalization could be performed using co-precipitation, hydrothermal, microwave, and thermal decomposition methodologies. We compared our TGA results for the $\text{Fe}_3\text{O}_4@PAANa$ and $\text{Fe}_3\text{O}_4@BPEI$ samples with those reported in the literature (128,129,145,149–151). The weight loss profile in the referenced papers presented more than one event attributed to the thermal decomposition of organic matter, which indicated the presence of weakly bound molecules on the surface of the NPs. It is worth mentioning that in these referenced publications, the TGA experiments were also performed in a N_2 atmosphere using a heating rate equal to or higher than $10\text{ }^\circ\text{C}/\text{min}$. Thus, our method has an advantage over these methods, because a homogeneous monolayer coating was achieved on the surface of Fe_3O_4 in just 12 min, which reduced the toxicity of these NPs (152).

Therefore, our FTIR and TGA results confirmed that the functionalization was successfully achieved in just 12 min through the sonochemistry approach and using simplified purification steps.

5.4 Colloidal Properties

The properties of a solution of the synthesized NPs were studied using DLS measurements. These experiments were performed just for the samples with colloidal stability in aqueous solvents, Fe₃O₄@PAANa, Fe₃O₄@CIT, and Fe₃O₄@BPEI, as listed in Table 3. The hydrodynamic sizes of Fe₃O₄@PAANa, Fe₃O₄@BPEI, and Fe₃O₄@CIT in water are 89.4, 131.7, 120.2 nm, respectively (Table 3). The sizes of these NPs are much greater than the XRD and TEM sizes, because the NPs tended to agglomerate in aqueous solutions, forming clusters, as reported in the literature (116,153). DLS measurements were also performed for aqueous solutions of the free CAs, in order to exclude the folding performed by the PAANa and BPEI (appendices 4 and 5). Moreover, the polydispersity index (PDI) values for the tested samples in water were 0.079, 0.060, and 0.094 for Fe₃O₄@PAANa, Fe₃O₄@BPEI, and Fe₃O₄@CIT, respectively. These values indicated that the hydrodynamic sizes of the synthesized NPs possessed high homogeneity (154), which is also one of the features required for biomedical applications (155).

Table 3 – Results from DLS experiments. The histograms for all the measurements are shown in appendices 6–12.

Sample	Solvent	Z-average size (nm)	PDI	ζ
Fe ₃ O ₄ @PAANa	H ₂ O	89.4 ± 1.1	0.079 ± 0.03	-55.5 ± 8.6
	PB 7.4	131.7 ± 0.6	0.072 ± 0.003	-30.6 ± 1.8
	PBS 7.4	117.8 ± 0.2	0.111 ± 0.028	-
Fe ₃ O ₄ @BPEI	H ₂ O	109.1 ± 5.0	0.060 ± 0.018	+44.5 ± 6.0
Fe ₃ O ₄ @CIT	H ₂ O	120.2 ± 1.0	0.094 ± 0.010	-32.4 ± 0.8
	PB 7.4	119.6 ± 0.9	0.106 ± 0.010	-41.7 ± 4.2

Source: Present author

The zeta potential (ζ) is a measure of the magnitude of the electrostatic charge on the surface of NPs, and is a key characteristic to be analyzed in relation to the colloidal stability. Therefore, the ζ values of the Fe₃O₄@PAANa, Fe₃O₄@BPEI, and Fe₃O₄@CIT samples were evaluated, and the results are listed in Table 3. The Fe₃O₄@PAANa and Fe₃O₄@CIT samples had negative values because of the presence of carboxylate groups. On the other hand, a positive value was observed for Fe₃O₄@BPEI (+44.5 ± 6.04 mV), which was a result of the presence of amine groups at the surface of the NPs. This positive value also

came from the slightly acidic pH of the water used to prepare the suspensions, which protonated amino groups, creating a positive coating. It is worth mentioning that the borderline between stable and unstable suspensions is generally considered to be either +30 or -30 mV (156). Therefore, because the ζ values of the analyzed samples were not in this range, they could be considered to be colloiddally stable in terms of ζ .

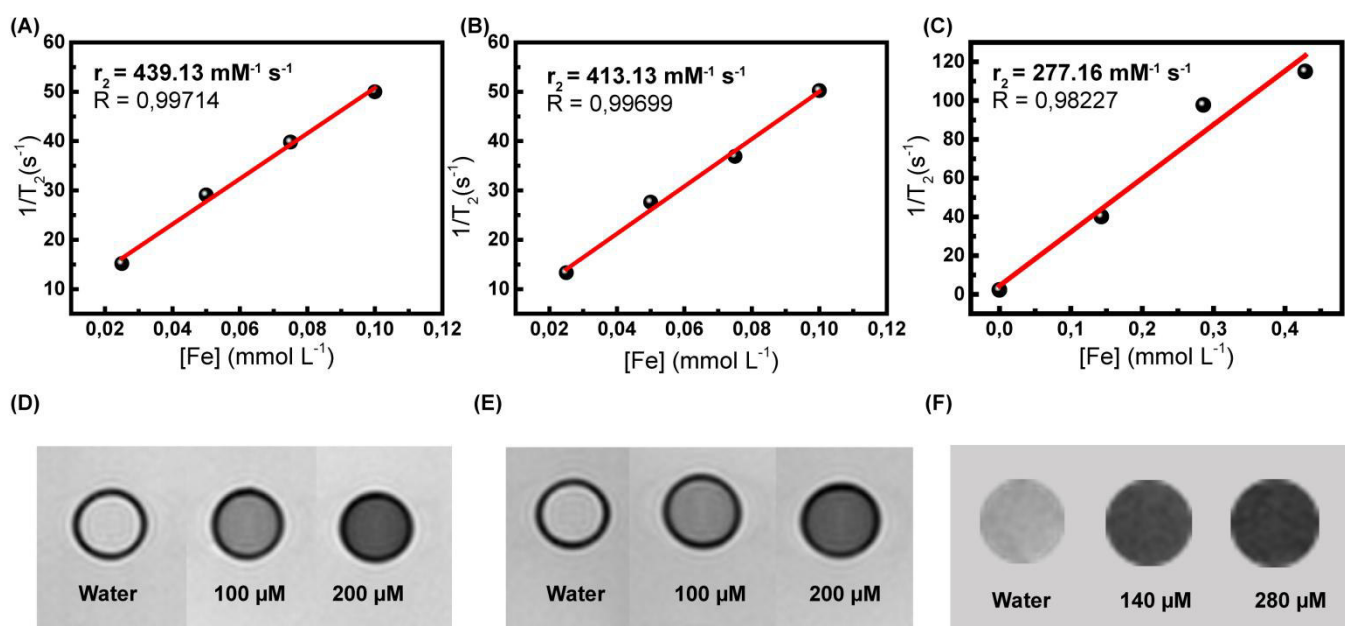
However, an absolute requirement for applying these suspensions in biomedicine is stability at the high ionic strengths of physiological solutions (33). With the exception of Fe₃O₄@PAANa, all of the samples failed to meet this requirement. In particular, in PBS (pH = 7.4) the particles started to rapidly agglomerate, reaching a Z-average size that was even larger than 1000 nm (data not shown). In contrast, the Fe₃O₄@PAANa sample displayed remarkable stability in PBS (pH = 7.4) and even in a medium with a high salt concentration. Only a slight increase in the Z-average size of this sample was evident in aqueous solvents, as listed in Table 3. Therefore, in terms of colloidal stability, the Fe₃O₄@PAANa sample was found to be suitable for biomedical applications.

5.5 MRI Properties

In this work, the potential application of the synthesized NPs as an MRI contrast agent was evaluated. For these experiments, just the samples with good colloidal stability in aqueous solvents were selected, which were Fe₃O₄@PAANa, Fe₃O₄@BPEI, and Fe₃O₄@CIT.

As previously mentioned, MNPs are traditionally T₂ contrast agents and ultra-small NPs, which was not the case in our study. For this reason, only the r_2 values will be discussed in this work. The r_2 values for the Fe₃O₄@PAANa, Fe₃O₄@BPEI, and Fe₃O₄@CIT samples were 439.13, 413.13, and 277.16 mM⁻¹ s⁻¹, respectively (Figure 21 and Table 4 entries 22–24). Figure 21 (D–F) shows the T₂ weighted MR images of the functionalized NPs produced in this work. It can be seen that an increase in the NP concentration generates darkened T₂ weighted images, showing the potential for applying the produced NPs as an MRI contrast agent.

Figure 21 – Magnetic R_2 relaxativity of (A) Fe_3O_4 @PAANa, (B) Fe_3O_4 @CIT, (C) Fe_3O_4 @BPEI samples. T_2 weighted images of aqueous suspensions of the (D) Fe_3O_4 @PAANa, (E) Fe_3O_4 @CIT, and (F) Fe_3O_4 @BPEI samples.



Source: Present author

Table 4 - Summary of previously reported MRI contrast agents based on Fe₃O₄ NPs prepared using traditional synthetic methodologies

Entry	Name	Magnetic core material	Core size ^a (nm)	Shell	Ms (emu/g)	r ₂ ^b (mM ⁻¹ s ⁻¹)	B ₀ (T) ^c	Synthetic Methodology	REF
1	Ferucarbotran (Resovist) ®	Fe ₃ O ₄	4	Carboxydextran	-	180	1.5	-	(157)
2	Ferumoxides (Feridex) ®	Fe ₃ O ₄ , γ-Fe ₂ O ₃	4,96	Dextran	-	120	1.5	-	(87)
3	Ferumoxtran (Combidex) ®	Fe ₃ O ₄	5.85	Dextran	-	128	3.0	-	(158)
4	Fe ₃ O ₄ -BPEI	Fe ₃ O ₄	17 ± 5	BPEI	-	156	-	Hydrothermal	(145)
5	Fe ₃ O ₄ -BPEI 2	Fe ₃ O ₄	12	BPEI	-	249	3.0	Thermal decomposition ^d	(125)
6	Fe ₃ O ₄ - PEG ^e -BPEI	Fe ₃ O ₄	10	PEG-BPEI	53	143	7	Thermal decomposition ^d	(159)
7	Fe ₃ O ₄ -PEI ^f	Fe ₃ O ₄	Size of the clusters: 200	PEI	70	124 ^g	1.5	Solvothermal	(160)
8	Fe ₃ O ₄ -Chitosan-PEI ^f	Fe ₃ O ₄	Micelles: 50–70; Core: 6	Chitosan-PEI	-	163	-	Thermal decomposition ^d	(161)
9	Fe ₃ O ₄ -CIT	Fe ₃ O ₄	6	CIT	58	102	3	Co-precipitation	(162).
10	Fe ₃ O ₄ -CIT 2	Fe ₃ O ₄	6	CIT	62	51.81	3	High-temperature salt hydrolysis followed by co-precipitation	(163)
11	Fe ₃ O ₄ -CIT 3	Fe ₃ O ₄	10.9	CIT	52	72.80	1.5	Hydrothermal	(117)

Table 4 – Continuation

12	Fe ₃ O ₄ -CIT 4	Fe ₃ O ₄	6	CIT	27	134	3	Grinding the precursors in a mortar	(164)
13	Fe ₃ O ₄ -CIT 5	Fe ₃ O ₄	10	CIT	-	156	1.5	Co-precipitation	(165)
14	Fe ₃ O ₄ -CIT 5	Fe ₃ O ₄	Size of the clusters: 200	CIT	53	360 ^g	1.5	Solvothermal	(160)
15	MnFe-CIT	Mn _{0.25} Fe _{0.75} Fe ₂ O ₄	8	CIT	62.4	237	1.5	Co-precipitation	(166)
16	MnFe-CTAB	MnFe ₂ O ₄	20	CTAB ^h	6	167	1.5	Thermal decomposition ^d	(167)
17	Fe ₃ O ₄ -DMSA	Fe ₃ O ₄	9	DMSA ⁱ	48	61	1.5	Thermal decomposition ^d	(168)
18	Fe ₃ O ₄ -DOPA-PEG	Fe ₃ O ₄	7	Dopamide-PEG	46	110	-	Thermal decomposition ^d	(169)
19	Fe ₃ O ₄ -PAA	Fe ₃ O ₄	8–10	PAA	56	105	3	Co-precipitation	(170)
20	Fe ₃ O ₄ -PAA 2	Fe ₃ O ₄	10	PAA	-	232	1.5	Co-precipitation	(165)
21	Fe ₃ O ₄ -PAANa	Fe ₃ O ₄	8	PAANa	-	206	0.47	Modified co-precipitation	(171)
22	Fe ₃ O ₄ @PAANa	Fe ₃ O ₄	11 ± 3	PAANa	70.7	439	1.41	Sonochemistry	This Work
23	Fe ₃ O ₄ @BPEI	Fe ₃ O ₄	10 ± 3	BPEI	70.2	277	1.41	Sonochemistry	This Work
24	Fe ₃ O ₄ @CIT	Fe ₃ O ₄	11 ± 3	CIT	76.8	413	1.41	Sonochemistry	This Work

^aCalculated by TEM or SEM; ^br₂: transverse relaxativity; ^cB₀: magnetic field strenght; ^dthermal decomposition was used to prepare the hydrophobic NPs followed by surface ligand exchange; ^epoly-ethylene glycol; ^fpolyethylenimine; ^g0.3% aqueous algarose gel was used as a solvent; ^hcetyl trimethylammonium bromide; ⁱDMSA: 2,3-dimercaptosuccinic acid

Source: Present author

In order to explain the greater values observed for PAANa and CIT compared to the BPEI-coated NPs, it is necessary to consider the influence of the coating layer of the contrast agent. The surface of the contrast agent affects the diffusion of the water molecules around the NPs. Water molecules need to be close to the magnetic core, so that they can be significantly influenced by the induced magnetic field of the contrast agent. Thus, the coating layer needs to interact with such molecules in order to increase their residence time around the agent (19). Therefore, a more hydrophilic coating will have a higher r_2 value (172,173). In this sense, we believe that the hydrophilicity played a key role in the better performance of the PAANa- and CIT-coated NPs compared to the BPEI-coated NPs (see Table 4, entries 22–24). This is reasonable because the carboxylate groups of PAANa and CIT provided a higher hydrophilicity than the amine groups of BPEI.

Table 4 (entries 1–21) lists the r_2 values found in the literature for commercial MNP-based contrast agents, as well as those prepared using the most traditional synthetic methodologies. It is evident that the r_2 values for the samples prepared in this work are higher than those for Resovist®, Feridex®, and Combidex® (Table 4, entries 1–3), which are commercial contrast agents.

Additionally, it is possible to note that MNPs functionalized with PAANa (or PAA), CIT, and BPEI (or PEI) have been synthesized and applied as MRI contrast agents, as listed in Table 4, entries 4–15 and 19–21. The NPs reported in these publications were prepared using the hydrothermal, co-precipitation, and thermal decomposition methods. The r_2 values of the BPEI- (or PEI-), CIT-, and PAANa- (or PAA-)based contrast agents had ranges of 107–249, 51–360, and 105–232 $\text{mM}^{-1}\text{s}^{-1}$, respectively. The r_2 values of the Fe_3O_4 @PAANa, Fe_3O_4 @BPEI, and Fe_3O_4 @CIT samples were higher by a factor of almost four. Further, it is worth mentioning that the samples synthesized in this work were prepared using inexpensive and non-toxic reactants, with easy operability and concise reaction times (12 min). These facts show the great potential of the proposed sonochemistry approach to prepare ferrofluids in a simple and elegant manner, while simultaneously obtaining high-quality materials.

6. CONCLUSIONS

In summary, the sonochemistry approach proposed in this work was used to directly prepare water-dispersible functionalized Fe_3O_4 NPs with excellent magnetic, colloidal, and relaxativity properties in a simple and rapid (12 min) manner. The coated NPs that were synthesized had Fe_3O_4 cores with diameters of 8–12 nm, which were in the transition to the superparamagnetism regime at room temperature. Moreover, the sonochemistry approach produced MNPs with tunable values of M_s , even after the overcoating with a non-magnetic material. The high energy induced by ultrasound irradiation enabled covalent interaction between the CA molecules and Fe_3O_4 , even though the time used in the synthesis was particularly short. Furthermore, the carboxylate- and amine-coated NPs showed great colloidal stability in water. Emphasis must be placed on the $\text{Fe}_3\text{O}_4@PAANa$ sample, which also exhibited colloidal stability under simulated physiological conditions. This is one of the most important requirements for *in vivo* applications. In addition, the MNPs obtained in this work displayed relaxativity properties greater than those of commercial contrast agents and agents obtained using other synthetic methods. Therefore, this study may open new avenues for the functionalization of MNPs with excellent physico-chemical properties for biological applications, facilitating the transition of MNPs to clinical treatment.

7. REFERENCES

- 1 Mathew, D.S.; Juang, R.-S. An overview of the structure and magnetism of spinel ferrite nanoparticles and their synthesis in microemulsions. **Chemical Engineering Journal**, v. 129, n. 1–3, p. 51–65, 2007.
- 2 Harris, V.G. Modern Microwave Ferrites. **IEEE Transactions on Magnetics**, v. 48, n. 3, p. 1075–1104, 2012.
- 3 Bragg, W.H. The structure of magnetite and the spinels. **Nature**, v. 95, p. 561, 1915.
- 4 Valenzuela, R. **Magnetic ceramics**. New York: Cambridge University Press, 1994.
- 5 Galvão, W.S.; Freire, R.M.; et al. Cubic superparamagnetic nanoparticles of NiFe₂O₄ via fast microwave heating. **Journal of Nanoparticle Research**, v. 16, n. 12, p. 2803, 2014.
- 6 Galvão, W.S.; Andrade Neto, D.A.; et al. Super-paramagnetic Nanoparticles with Spinel Structure: A Review of Synthesis and Biomedical Applications. **Solid State Phenomena**, v. 241, p. 139–176, 2015.
- 7 Graham, B.D.C.C.D. **Introduction to Magnetic Materials**. New Jersey: John Wiley & Sons, 2009.
- 8 Néel, L. Propriétés magnétiques des ferrites - ferrimagnétisme et antiferromagnétisme. **Annales de Physique**, v. 3, n. 2, p. 137–198, 1948.
- 9 Estelrich, J.; Escribano, E.; et al. Iron Oxide Nanoparticles for Magnetically-Guided and Magnetically-Responsive Drug Delivery. **International journal of molecular sciences**, v. 16, n. 4, p. 8070–8101, 2015.
- 10 Spaldin, N.A. **Magnetic Materials: Fundamentals and Applications**. Cambridge University Press, 2010.
- 11 Kolhatkar, A.; Jamison, A.; et al. Tuning the Magnetic Properties of Nanoparticles. **International Journal of Molecular Sciences**, v. 14, n. 8, p. 15977–16009, 2013.
- 12 **Magnetic Nanoparticles**. Weinheim: WILEY-VCH Verlag, 2009.
- 13 Wu, W.; Wu, Z.; et al. Recent progress on magnetic iron oxide nanoparticles: synthesis, surface functional strategies and biomedical applications. **Science and Technology of Advanced Materials**, v. 16, n. 2, p. 23501, 2015.
- 14 Cao, S.-W.; Zhu, Y.-J.; et al. Hierarchically Nanostructured Magnetic Hollow Spheres of Fe₃O₄ and γ -Fe₂O₃: Preparation and Potential Application in Drug Delivery. **Journal of Physical Chemistry C**, v. 112, n. 6, p. 1851–1856, 2008.
- 15 Laurent, S.; Forge, D.; et al. Magnetic iron oxide nanoparticles: Synthesis, stabilization, vectorization, physicochemical characterizations, and biological applications. **Chemical Reviews**, v. 108, n. 6, p. 2064–2110, 2008.
- 16 Li, W.-M.M.; Chen, S.-Y.Y.; et al. In situ doxorubicin-CaP shell formation on amphiphilic gelatin-iron oxide core as a multifunctional drug delivery system with improved

cytocompatibility, pH-responsive drug release and MR imaging. **Acta Biomaterialia**, v. 9, n. 2, p. 5360–5368, 2013.

17 Lee, E.S.; Gao, Z.; et al. Recent progress in tumor pH targeting nanotechnology. **Journal of controlled release : official journal of the Controlled Release Society**, v. 132, n. 3, p. 164–70, 2008.

18 Li, W.-M.; Chen, S.-Y.; et al. In situ doxorubicin-CaP shell formation on amphiphilic gelatin-iron oxide core as a multifunctional drug delivery system with improved cytocompatibility, pH-responsive drug release and MR imaging. **Acta biomaterialia**, v. 9, n. 2, p. 5360–8, 2013.

19 Lee, N.; Hyeon, T. Designed synthesis of uniformly sized iron oxide nanoparticles for efficient magnetic resonance imaging contrast agents. **Chem. Soc. Rev.**, v. 41, n. 7, p. 2575–2589, 2012.

20 Brown, R.W.; Cheng, Y.-C.N.; et al. **Magnetic resonance imaging: physical principles and sequence design**. John Wiley & Sons, 2014.

21 Kozłowska, D.; Foran, P.; et al. Molecular and magnetic resonance imaging: The value of immunoliposomes. **Advanced Drug Delivery Reviews**, v. 61, n. 15, p. 1402–1411, 2009.

22 Shin, T.; Choi, Y.; et al. Recent advances in magnetic nanoparticle-based multi-modal imaging. **Chemical Society Reviews**, v. 44, p. 4501–4516, 2015.

23 Peng, X.-H.; Qian, X.; et al. Targeted magnetic iron oxide nanoparticles for tumor imaging and therapy. **International journal of nanomedicine**, v. 3, n. 3, p. 311–321, 2008.

24 Yue-Jian, C.; Juan, T.; et al. Synthesis, self-assembly, and characterization of PEG-coated iron oxide nanoparticles as potential MRI contrast agent. **Drug development and industrial pharmacy**, v. 36, n. 10, p. 1235–1244, 2010.

25 Chow, A.M.; Chan, K.W.Y.; et al. Enhancement of gas-filled microbubble R2* by iron oxide nanoparticles for MRI. **Magnetic resonance in medicine : official journal of the Society of Magnetic Resonance in Medicine / Society of Magnetic Resonance in Medicine**, v. 63, n. 1, p. 224–9, 2010.

26 Jun, Y.-W.; Huh, Y.-M.; et al. Nanoscale size effect of magnetic nanocrystals and their utilization for cancer diagnosis via magnetic resonance imaging. **Journal of the American Chemical Society**, v. 127, n. 16, p. 5732–5733, 2005.

27 Kim, B.H.; Lee, N.; et al. Large-Scale Synthesis of Uniform and Extremely Small-Sized Iron Oxide Nanoparticles for High-Resolution T-1 Magnetic Resonance Imaging Contrast Agents. **Journal of the American Chemical Society**, v. 133, p. 12624–12631, 2011.

28 Thomas, L.A.; Dekker, L.; et al. Carboxylic acid-stabilised iron oxide nanoparticles for use in magnetic hyperthermia. **Journal of Materials Chemistry**, v. 19, n. 36, p. 6529, 2009.

29 Dobson, Q.A.P. and J.C. and S.K.J. and J. Applications of magnetic nanoparticles in biomedicine. **Journal of Physics D: Applied Physics**, v. 36, n. 13, p. R167, 2003.

30 Laurent, S.; Dutz, S.; et al. Magnetic fluid hyperthermia: Focus on superparamagnetic iron oxide nanoparticles. **Advances in Colloid and Interface Science**, v. 166, n. 1–2, p. 8–23, 2011.

- 31 Corato, R. Di; Espinosa, A.; et al. Magnetic hyperthermia efficiency in the cellular environment for different nanoparticle designs. **Biomaterials**, v. 35, n. 24, p. 6400–6411, 2014.
- 32 Rabias, I.; Tsitrouli, D.; et al. Rapid magnetic heating treatment by highly charged maghemite nanoparticles on Wistar rats exocranial glioma tumors at microliter volume. **Biomicrofluidics**, v. 4, n. 2, p. 1–8, 2010.
- 33 Amstad, E.; Textor, M.; et al. Stabilization and functionalization of iron oxide nanoparticles for biomedical applications. **Nanoscale**, v. 3, n. 7, p. 2819, 2011.
- 34 Hola, K.; Markova, Z.; et al. Tailored functionalization of iron oxide nanoparticles for MRI, drug delivery, magnetic separation and immobilization of biosubstances. **Biotechnology Advances**, v. 33, n. 6, Part 2, p. 1162–1176, 2015.
- 35 Kooti, M.; Matturi, L. Microwave- Assisted Fabrication of γ -Fe₂O₃ Nanoparticles from Tris (acetylacetonato) Iron (III). **International Nano Letters**, v. 1, n. 1, p. 38–42, 2011.
- 36 Salunkhe, a. B.; Khot, V.M.; et al. Synthesis and magnetostructural studies of amine functionalized superparamagnetic iron oxide nanoparticles. **RSC Advances**, v. 5, p. 18420–18428, 2015.
- 37 Roth, H.-C.; Schwaminger, S.P.; et al. Influencing factors in the CO-precipitation process of superparamagnetic iron oxide nano particles: A model based study. **Journal of Magnetism and Magnetic Materials**, v. 377, p. 81–89, 2015.
- 38 Massart, R. Preparation of aqueous magnetic liquids in alkaline and acidic media. **Magnetics, IEEE Transactions on**, v. 17, n. 2, p. 1247–1248, 1981.
- 39 Suh, S.K.; Yuet, K.; et al. Synthesis of Nonspherical Superparamagnetic Particles: In Situ Coprecipitation of Magnetic Nanoparticles in Microgels Prepared by Stop-Flow Lithography. **Journal of the American Chemical Society**, v. 134, n. 17, p. 7337–7343, 2012.
- 40 Ravikumar, C.; Bandyopadhyaya, R. Mechanistic Study on Magnetite Nanoparticle Formation by Thermal Decomposition and Coprecipitation Routes. **The Journal of Physical Chemistry C**, v. 115, n. 5, p. 1380–1387, 2011.
- 41 Yan, K.; Li, P.; et al. Recent advances in multifunctional magnetic nanoparticles and applications to biomedical diagnosis and treatment. **RSC Advances**, v. 3, n. 27, p. 10598–10618, 2013.
- 42 Freire, R.M.; Freitas, P.G.C.; et al. Effect of solvent composition on the structural and magnetic properties of MnZn ferrite nanoparticles obtained by hydrothermal synthesis. **Microfluidics and Nanofluidics**, v. 17, n. 1, p. 233–244, 2013.
- 43 Wu, W.; Xiao, X.; et al. Large-Scale and Controlled Synthesis of Iron Oxide Magnetic Short Nanotubes: Shape Evolution, Growth Mechanism, and Magnetic Properties. **The Journal of Physical Chemistry C**, v. 114, n. 39, p. 16092–16103, 2010.
- 44 LaMer, V.K.; Dinegar, R.H. Theory, Production and Mechanism of Formation of Monodispersed Hydrosols. **Journal of the American Chemical Society**, v. 72, n. 11, p. 4847–4854, 1950.

- 45 Murray, C.B.; Kagan, C.R.; et al. Synthesis and characterization of monodisperse nanocrystals and close-packed nanocrystal assemblies. **Annual Review of Materials Science**, v. 30, p. 545–610, 2000.
- 46 Frey, N.A.; Peng, S.; et al. Magnetic nanoparticles: synthesis, functionalization, and applications in bioimaging and magnetic energy storage. **Chemical Society Reviews**, v. 38, n. 9, p. 2532–2542, 2009.
- 47 Sun, S.; Zeng, H.; et al. Monodisperse MFe₂O₄ (M = Fe, Co, Mn) Nanoparticles. **Journal of the American Chemical Society**, v. 126, n. 1, p. 273–279, 2004.
- 48 Woo, K.; Hong, J.; et al. Easy Synthesis and Magnetic Properties of Iron Oxide Nanoparticles. **Chemistry of Materials**, v. 16, n. 14, p. 2814–2818, 2004.
- 49 Wang, Y.; Zhu, Z.; et al. One-pot reaction to synthesize superparamagnetic iron oxide nanoparticles by adding phenol as reducing agent and stabilizer. **Journal of Nanoparticle Research**, v. 14, n. 4, p. 1–7, 2012.
- 50 Bronstein, L.M.; Huang, X.; et al. Influence of Iron Oleate Complex Structure on Iron Oxide Nanoparticle Formation. **Chemistry of Materials**, v. 19, n. 15, p. 3624–3632, 2007.
- 51 Rockenberger, J.; Scher, E.C.; et al. A New Nonhydrolytic Single-Precursor Approach to Surfactant-Capped Nanocrystals of Transition Metal Oxides. **Journal of the American Chemical Society**, v. 121, n. 49, p. 11595–11596, 1999.
- 52 Liang, X.; Wang, X.; et al. Synthesis of Nearly Monodisperse Iron Oxide and Oxyhydroxide Nanocrystals. **Advanced Functional Materials**, v. 16, n. 14, p. 1805–1813, 2006.
- 53 Hu, M.; Jiang, J.-S.; et al. Hierarchical magnetic iron (iii) oxides prepared by solid-state thermal decomposition of coordination polymers. **RSC Advances**, v. 2, n. 11, p. 4782–4786, 2012.
- 54 Hu, M.; Jiang, J.-S.; et al. Prussian blue microcrystals prepared by selective etching and their conversion to mesoporous magnetic iron(iii) oxides. **Chem. Commun.**, v. 46, n. 7, p. 1133–1135, 2010.
- 55 Asuha, S.; Zhao, S.; et al. One step synthesis of maghemite nanoparticles by direct thermal decomposition of Fe–urea complex and their properties. **Journal of Alloys and Compounds**, v. 472, n. 1–2, p. L23–L25, 2009.
- 56 Amara, D.; Margel, S. Solventless thermal decomposition of ferrocene as a new approach for the synthesis of porous superparamagnetic and ferromagnetic composite microspheres of narrow size distribution. **J. Mater. Chem.**, v. 21, n. 39, p. 15764–15772, 2011.
- 57 Maity, D.; Choo, S.-G.; et al. Synthesis of magnetite nanoparticles via a solvent-free thermal decomposition route. **Journal of Magnetism and Magnetic Materials**, v. 321, n. 9, p. 1256–1259, 2009.
- 58 Li, Z.; Sun, Q.; et al. Preparation of water-soluble magnetite nanocrystals from hydrated ferric salts in 2-pyrrolidone: mechanism leading to Fe₃O₄. **Angewandte Chemie (International ed. in English)**, v. 44, n. 1, p. 123–6, 2004.

- 59 Bang, J.H.; Suslick, K.S. Applications of ultrasound to the synthesis of nanostructured materials. **Advanced Materials**, v. 22, n. 10, p. 1039–1059, 2010.
- 60 Xu, H.; Zeiger, B.W.; et al. Sonochemical synthesis of nanomaterials. **Chem. Soc. Rev.**, v. 42, n. 7, p. 2555–2567, 2013.
- 61 Mason, T.J. **Advances in sonochemistry**. Elsevier, 1996.
- 62 Suslick, K.S. Sonochemistry. **Science (New York, N.Y.)**, v. 247, n. 4949, p. 1439–1445, 1990.
- 63 Freire, T.M.; Dutra, L.M.U.; et al. Fast ultrasound assisted synthesis of chitosan-based magnetite nanocomposites as a modified electrode sensor. **Carbohydrate Polymers**, v. 151, p. 760–769, 2016.
- 64 Vijayakumar, R.; Kolytyn, Y.; et al. Sonochemical synthesis and characterization of pure nanometer-sized Fe₃O₄ particles. **Materials Science and Engineering: A**, v. 286, p. 101–105, 2000.
- 65 Abu Mukh-Qasem, R.; Gedanken, A. Sonochemical synthesis of stable hydrosol of Fe₃O₄ nanoparticles. **Journal of Colloid and Interface Science**, v. 284, p. 489–494, 2005.
- 66 Morel, A.-L.; Nikitenko, S.I.; et al. Sonochemical Approach to the Synthesis of Fe₃O₄@SiO₂ Core–Shell Nanoparticles with Tunable Properties. **ACS Nano**, v. 2, n. 5, p. 847–856, 2008.
- 67 Mizukoshi, Y.; Shuto, T.; et al. Preparation of superparamagnetic magnetite nanoparticles by reverse precipitation method: Contribution of sonochemically generated oxidants. **Ultrasonics Sonochemistry**, v. 16, n. 4, p. 525–531, 2009.
- 68 Theerdhala, S.; Bahadur, D.; et al. Sonochemical stabilization of ultrafine colloidal biocompatible magnetite nanoparticles using amino acid, l-arginine, for possible bio applications. **Ultrasonics Sonochemistry**, v. 17, n. 4, p. 730–737, 2010.
- 69 Cheng, J.P.; Ma, R.; et al. Rapid growth of magnetite nanoplates by ultrasonic irradiation at low temperature. **Ultrasonics sonochemistry**, v. 18, n. 5, p. 1038–42, 2011.
- 70 Wu, S.; Sun, A.; et al. Fe₃O₄ magnetic nanoparticles synthesis from tailings by ultrasonic chemical co-precipitation. **Materials Letters**, v. 65, n. 12, p. 1882–1884, 2011.
- 71 Nazrul Islam, M.; Phong, L. Van; et al. A facile route to sonochemical synthesis of magnetic iron oxide (Fe₃O₄) nanoparticles. **Thin Solid Films**, v. 519, n. 23, p. 8277–8279, 2011.
- 72 Marchegiani, G.; Imperatori, P.; et al. Sonochemical synthesis of versatile hydrophilic magnetite nanoparticles. **Ultrasonics sonochemistry**, v. 19, n. 4, p. 877–82, 2012.
- 73 Zhang, S.; Zhang, Y.; et al. Sonochemical formation of iron oxide nanoparticles in ionic liquids for magnetic liquid marble. **Physical chemistry chemical physics: PCCP**, v. 14, n. 15, p. 5132–8, 2012.
- 74 Abbas, M.; Takahashi, M.; et al. Facile sonochemical synthesis of high-moment magnetite (Fe₃O₄) nanocube. **Journal of Nanoparticle Research**, v. 15, n. 1, p. 1–12, 2012.
- 75 Zhu, S.; Guo, J.; et al. Sonochemical fabrication of Fe₃O₄ nanoparticles on reduced

- graphene oxide for biosensors. **Ultrasonics Sonochemistry**, v. 20, n. 3, p. 872–880, 2013.
- 76 Martínez, H.; D'Onofrio, L.; et al. Mössbauer study of a Fe₃O₄/PMMA nanocomposite synthesized by sonochemistry. **Hyperfine Interactions**, v. 224, n. 1–3, p. 99–107, 2014.
- 77 Dolores, R.; Raquel, S.; et al. Sonochemical synthesis of iron oxide nanoparticles loaded with folate and cisplatin: Effect of ultrasonic frequency. **Ultrasonics Sonochemistry**, v. 23, n. 0, p. 391–398, 2015.
- 78 Szpak, A.; Fiejdasz, S.; et al. T1-T2 Dual-modal MRI contrast agents based on superparamagnetic iron oxide nanoparticles with surface attached gadolinium complexes. **Journal of nanoparticle research : an interdisciplinary forum for nanoscale science and technology**, v. 16, n. 11, p. 2678, 2014.
- 79 Kandasamy, G.; Maity, D. Recent advances in superparamagnetic iron oxide nanoparticles (SPIONs) for in vitro and in vivo cancer nanotheranostics. **International Journal of Pharmaceutics**, v. 496, n. 2, p. 191–218, 2015.
- 80 Ulbrich, K.; Holá, K.; et al. Targeted Drug Delivery with Polymers and Magnetic Nanoparticles: Covalent and Noncovalent Approaches, Release Control, and Clinical Studies. **Chemical Reviews**, v. 116, n. 9, p. 5338–5431, 2016.
- 81 Yildiz, I.; Applications of magnetic nanoparticles in biomedical separation and purification. **Nanotechnology Reviews** v. 5, n.3, p. 331–340, 2016.
- 82 Beik, J.; Abed, Z.; et al. Nanotechnology in hyperthermia cancer therapy: From fundamental principles to advanced applications. **Journal of Controlled Release**, v. 235, p. 205–221, 2016.
- 83 Goodfellow, F.T.; Simchick, G.A.; et al. Tracking and Quantification of Magnetically Labeled Stem Cells Using Magnetic Resonance Imaging. **Advanced Functional Materials** v. 26, n. 22, p. 3899–3915, 2016.
- 84 Gao, Z.; Ma, T.; et al. Small is Smarter: Nano MRI Contrast Agents - Advantages and Recent Achievements. **Small**, v. 12, n. 5, p. 556–576, 2016.
- 85 Peng, E.; Wang, F.; et al. Nanostructured magnetic nanocomposites as MRI contrast agents. **J. Mater. Chem. B**, v. 3, n. 11, p. 2241–2276, 2015.
- 86 Frisoni, G.B.; Fox, N.C.; et al. The clinical use of structural MRI in Alzheimer disease. **Nature reviews. Neurology**, v. 6, n. 2, p. 67–77, 2010.
- 87 Wang, Y.X.; Hussain, S.M.; et al. Superparamagnetic iron oxide contrast agents: physicochemical characteristics and applications in MR imaging. **Eur Radiol**, v. 11, n. 11, p. 2319–2331, 2001.
- 88 Na, H. Bin; Song, I.C.; et al. Inorganic nanoparticles for MRI contrast agents. **Advanced Materials**, v. 21, n. 21, p. 2133–2148, 2009.
- 89 Lee, N.; Yoo, D.; et al. Iron Oxide Based Nanoparticles for Multimodal Imaging and Magneto-responsive Therapy. **Chemical Reviews**, v. 115, n. 19, p. 10637–10689, 2015.
- 90 Qiao, R.; Yang, C.; et al. Superparamagnetic iron oxide nanoparticles : from preparations to in vivo MRI applications. **Journal Materials Chemistry**, v. 19, p. 6274–6293, 2009.

- 91 Winter, P.M.; Neubauer, A.M.; et al. Endothelial $\alpha\text{v}\beta\text{3}$ integrin-targeted fumagillin nanoparticles inhibit angiogenesis in atherosclerosis. **Arteriosclerosis, Thrombosis, and Vascular Biology**, v. 26, n. 9, p. 2103–2109, 2006.
- 92 Montet, X.; Montet-Abou, K.; et al. Nanoparticle imaging of integrins on tumor cells. **Neoplasia**, v. 8, n. 3, p. 214–222, 2006.
- 93 Nahrendorf, M.; Jaffer, F.A.; et al. Noninvasive vascular cell adhesion molecule-1 imaging identifies inflammatory activation of cells in atherosclerosis. **Circulation**, v. 114, n. 14, p. 1504–1511, 2006.
- 94 Zhao, Z.; Zhou, Z.; et al. Octapod iron oxide nanoparticles as high-performance T_2 contrast agents for magnetic resonance imaging. **Nature communications**, v. 4, p. 2266, 2013.
- 95 Tong, S.; Hou, S.; et al. Coating optimization of superparamagnetic iron oxide nanoparticles for high T_2 relaxivity. **Nano Letters**, v. 10, n. 11, p. 4607–4613, 2010.
- 96 Brooks, R.A.; Moyny, F.; et al. On T_2 -shortening by weakly magnetized particles: The chemical exchange model. **Magnetic Resonance in Medicine**, v. 45, n. 6, p. 1014–1020, 2001.
- 97 Gillis, P.; Moyny, F.; et al. On T_2 -shortening by strongly magnetized spheres: A partial refocusing model. **Magnetic Resonance in Medicine**, v. 47, n. 2, p. 257–263, 2002.
- 98 Stephen, Z.R.; Dayringer, C.J.; et al. Approach to Rapid Synthesis and Functionalization of Iron Oxide Nanoparticles for High Gene Transfection. **ACS Applied Materials & Interfaces**, v. 8, n. 10, p. 6320–6328, 2016.
- 99 Patil, A.B., Bhanage, B.M. Sonochemistry: A Greener Protocol for Nanoparticles Synthesis BT - Handbook of Nanoparticles. **Springer International Publishing**, p. 143–166, 2016.
- 100 Szpak, A.; Fiejdasz, S.; et al. T_1 - T_2 Dual-modal MRI contrast agents based on superparamagnetic iron oxide nanoparticles with surface attached gadolinium complexes. **Journal of Nanoparticle Research**, v. 16, n. 11, 2014.
- 101 Bleicher, L.; Sasaki, J.M.; et al. Development of graphical interface for the Rietveld refinement program DBWS. **Journal of Applied Crystallography**, v. 33, 2000.
- 102 Jin, X.; Chen, X.; et al. Effects of hydrothermal temperature and time on hydrothermal synthesis of colloidal hydroxyapatite nanorods in the presence of sodium citrate. **Journal of colloid and interface science**, v. 450, p. 151–8, 2015.
- 103 Tiunov, I.A.; Gorbachevskyy, M. V; et al. Synthesis of Large Uniform Gold and Core – Shell Gold – Silver Nanoparticles: Effect of Temperature Control. **Russian Journal of Physical Chemistry A**, v. 90, n. 1, p. 152–157, 2016.
- 104 Peniche, H.; Osorio, A.; et al. Preparation and characterization of superparamagnetic chitosan microspheres: Application as a support for the immobilization of tyrosinase. **Journal of Applied Polymer Science**, v. 98, n. 2, p. 651–657, 2005.
- 105 Phosphate-buffered saline (PBS). **Cold Spring Harbor Protocols**, v. 2006, n. 1, p. pdb.rec8247, 2006.

- 106 Wu, W.; He, Q.; et al. Magnetic Iron Oxide Nanoparticles: Synthesis and Surface Functionalization Strategies. **Nanoscale Research Letters**, v. 3, n. 11, p. 397–415, 2008.
- 107 Jevtić, M.; Mitrić, M.; et al. Crystal Structure of Hydroxyapatite Nanorods Synthesized by Sonochemical Homogeneous Precipitation. **Crystal Growth & Design**, v. 8, n. 7, p. 2217–2222, 2008.
- 108 Han, Y.; Wang, X.; et al. A simple route to prepare stable hydroxyapatite nanoparticles suspension. **Journal of Nanoparticle Research**, v. 11, n. 5, p. 1235–1240, 2009.
- 109 Sadat-Shojai, M.; Khorasani, M.T.; et al. Synthesis methods for nanosized hydroxyapatite with diverse structures. **Acta Biomaterialia**, v. 9, n. 8, p. 7591–7621, 2013.
- 110 Orozco-Henao, J.M.; Coral, D.F.; et al. Effects of Nanostructure and Dipolar Interactions on Magnetohyperthermia in Iron Oxide Nanoparticles. **The Journal of Physical Chemistry C**, v. 120, n. 23, p. 12796–12809, 2016.
- 111 Xu, S.; Yang, F.; et al. Uniform PEGylated PLGA Microcapsules with Embedded Fe₃O₄ Nanoparticles for US/MR Dual-Modality Imaging. **ACS applied materials & interfaces**, v. 7, n. 36, p. 20460–8, 2015.
- 112 Freire, R.M.; Ribeiro, T.S.; et al. MZnFe₂O₄ (M = Ni, Mn) cubic superparamagnetic nanoparticles obtained by hydrothermal synthesis. **Journal of Nanoparticle Research**, v. 15, n. 5, p. 1616, 2013.
- 113 Iyengar, S.J.; Joy, M.; et al. Magnetic, X-ray and Mössbauer studies on magnetite/maghemite core-shell nanostructures fabricated through an aqueous route. **RSC Advances**, v. 4, n. 110, p. 64919–64929, 2014.
- 114 Hong, J.H.; Kim, W.S.; et al. Exchange coupled magnetic nanocomposites of Sm(Co_{1-x}Fe_x)₅ / Fe₃O₄ with core/shell structure. **Solid State Communications**, v. 141, n. 10, p. 541–544, 2007.
- 115 Lu, T.; Wang, J.; et al. Surfactant effects on the microstructures of Fe₃O₄ nanoparticles synthesized by microemulsion method. **Colloids and Surfaces A: Physicochemical and Engineering Aspects**, v. 436, p. 675–683, 2013.
- 116 Kolen'ko, Y. V.; Bañobre-López, M.; et al. Large-Scale Synthesis of Colloidal Fe₃O₄ Nanoparticles Exhibiting High Heating Efficiency in Magnetic Hyperthermia. **The Journal of Physical Chemistry C**, v. 118, n. 16, p. 8691–8701, 2014.
- 117 Wu, L.; Yang, C.; et al. Facile one-pot synthesis of different surfactant-functionalized water-soluble Fe₃O₄ nanoparticles as magnetic resonance imaging contrast agents for melanoma tumors. **RSC Advances**, v. 5, n. 62, p. 50557–50564, 2015.
- 118 Witte, K.; Bodnar, W.; et al. A detailed study on the transition from the blocked to the superparamagnetic state of reduction-precipitated iron oxide nanoparticles. **Journal of Magnetism and Magnetic Materials**, v. 403, p. 103–113, 2016.
- 119 Daou, T.J.; Pourroy, G.; et al. Water soluble dendronized iron oxide nanoparticles. **Dalton transactions (Cambridge, England : 2003)**, n. 23, p. 4442–9, 2009.
- 120 Zélis, P.M.; Pasquevich, G. a; et al. Structural and magnetic study of zinc-doped magnetite nanoparticles and ferrofluids for hyperthermia applications. **Journal of Physics D:**

Applied Physics, v. 46, n. 12, p. 125006, 2013.

121 León-Félix, L.; Chaker, J.; et al. Synthesis and characterization of uncoated and gold-coated magnetite nanoparticles. **Hyperfine Interactions**, v. 224, n. 1–3, p. 179–188, 2014.

122 Bhattacharya, S.; Roychowdhury, A.; et al. Effect of biomimetic templates on the magneto-structural properties of Fe₃O₄ nanoparticles. **RSC Advances**, v. 5, n. 18, p. 13777–13786, 2015.

123 Mikhaylova, M.; Kim, D.K.; et al. Superparamagnetism of Magnetite Nanoparticles: Dependence on Surface Modification. **Langmuir**, v. 20, n. 6, p. 2472–2477, 2004.

124 Stoner, E.C.; Wohlfarth, E.P. A mechanism of magnetic hysteresis in heterogeneous alloys. **IEEE Transactions on Magnetics**, v. 27, n. 4, p. 3475–3518, 1991.

125 Mohapatra, J.; Mitra, A.; et al. Iron oxide nanorods as high-performance magnetic resonance imaging contrast agents. **Nanoscale**, v. 7, n. 20, p. 9174–84, 2015.

126 Lasheras, X.; Insausti, M.; et al. **Chemical Synthesis and Magnetic Properties of Monodisperse Nickel Ferrite Nanoparticles for Biomedical Applications**. 2016.

127 Hu, F.; Wei, L.; et al. Preparation of biocompatible magnetite nanocrystals for in vivo magnetic resonance detection of cancer. **Advanced Materials**, v. 18, n. 19, p. 2553–2556, 2006.

128 Calatayud, M.P.; Sanz, B.; et al. The effect of surface charge of functionalized Fe₃O₄ nanoparticles on protein adsorption and cell uptake. **Biomaterials**, v. 35, n. 24, p. 6389–99, 2014.

129 Li, J.; Hu, Y.; et al. Facile synthesis of folic acid-functionalized iron oxide nanoparticles with ultrahigh relaxivity for targeted tumor MR imaging. **J. Mater. Chem. B**, v. 3, n. 28, p. 5720–5730, 2015.

130 Wang, Y.; Xu, F.; et al. One-pot solvothermal synthesis of Fe₃O₄–PEI composite and its further modification with Au nanoparticles. **Journal of Nanoparticle Research**, v. 15, n. 1, p. 1338, 2012.

131 Daou, T.J.; Pourroy, G.; et al. Hydrothermal Synthesis of Monodisperse Magnetite Nanoparticles. **Chem. Mater.**, v. 18, n. 18, p. 4399–4404, 2006.

132 Guardia, P.; Labarta, A.; et al. Tuning the Size, the Shape, and the Magnetic Properties of Iron Oxide Nanoparticles. **The Journal of Physical Chemistry C**, v. 115, n. 2, p. 390–396, 2011.

133 Auffan, M.; Rose, J.; et al. Towards a definition of inorganic nanoparticles from an environmental, health and safety perspective. **Nat Nano**, v. 4, n. 10, p. 634–641, 2009.

134 Schwaminger, S.P.; García, P.F.; et al. Nature of Interactions of Amino Acids with Bare Magnetite Nanoparticles. **The Journal of Physical Chemistry C**, v. 119, n. 40, p. 23032–23041, 2015.

135 Pujari, S.P.; Scheres, L.; et al. Covalent surface modification of oxide surfaces. **Angewandte Chemie**, v. 53, n. 25, p. 6322–6356, 2014.

- 136 Deacon, G.B.; PHILLIPS, R.J. Relationships between the carbon-oxygen stretching frequencies of carboxylato complexes and the type of carboxylate coordination. **Coord. Chem. Rev.**, v. 33, n. 3, p. 227–250, 1980.
- 137 Jovanović, S.; Spreitzer, M.; et al. Effect of Oleic Acid Concentration on the Physicochemical Properties of Cobalt Ferrite Nanoparticles. **The Journal of Physical Chemistry C**, v. 118, n. 25, p. 13844–13856, 2014.
- 138 Brand, J. van den; Blajiev, O.; et al. Interaction of anhydride and carboxylic acid compounds with aluminum oxide surfaces studied using infrared reflection absorption spectroscopy. **Langmuir : the ACS journal of surfaces and colloids**, v. 20, n. 15, p. 6308–6317, 2004.
- 139 Lenz, A.; Selegård, L.; et al. ZnO nanoparticles functionalized with organic acids: An experimental and quantum-chemical study. **Journal of Physical Chemistry C**, v. 113, n. 40, p. 17332–17341, 2009.
- 140 Taheri, P., Wielant, J., et al. A comparison of the interfacial bonding properties of carboxylic acid functional groups on zinc and iron substrates. In: **Electrochimica Acta**. v.56.2011, p. 1904–1911.
- 141 Limaye, M. V.; Singh, S.B.; et al. High coercivity of oleic acid capped CoFe₂O₄ nanoparticles at room temperature. **Journal of Physical Chemistry B**, v. 113, n. 27, p. 9070–9076, 2009.
- 142 Baccile, N.; Noiville, R.; et al. Sophorolipids-functionalized iron oxide nanoparticles. **Physical Chemistry Chemical Physics**, v. 15, n. 5, p. 1606–20, 2013.
- 143 Nakamoto, K. Infrared and Raman Spectra of Inorganic and Coordination Compounds. In: **Handbook of Vibrational Spectroscopy**. John Wiley & Sons, Ltd, 2006,
- 144 Chernyshova, I. V.; Ponnurangam, S.; et al. Adsorption of fatty acids on iron (hydr)oxides from aqueous solutions. **Langmuir**, v. 27, n. 16, p. 10007–10018, 2011.
- 145 Cai, H.; An, X.; et al. Facile hydrothermal synthesis and surface functionalization of polyethyleneimine-coated iron oxide nanoparticles for biomedical applications. **ACS applied materials & interfaces**, v. 5, n. 5, p. 1722–31, 2013.
- 146 Sacconi, L.; Sabatini, A.; et al. Infrared Spectra from 80 to 2000 Cm⁻¹ of Some Metal-Ammine Complexes. **Inorganic Chemistry**, v. 3, n. 12, p. 1772–1774, 1964.
- 147 Bennett, A.M. a.; Foulds, G. a.; et al. ab. **Spectrochimica Acta Part A: Molecular Spectroscopy**, v. 46, n. 1, p. 13–22, 1990.
- 148 Shen, L.; Laibinis, P.E.; et al. Bilayer Surfactant Stabilized Magnetic Fluids: Synthesis and Interactions at Interfaces. **Langmuir**, v. 15, n. 2, p. 447–453, 1999.
- 149 Liu, S.; Lu, F.; et al. Microwave-assisted synthesis of a biocompatible polyacid-conjugated Fe₃O₄ superparamagnetic hybrid. **CrystEngComm**, v. 13, n. 7, p. 2425–2429, 2011.
- 150 Ling, M.M.; Wang, K.Y.; et al. Highly water-soluble magnetic nanoparticles as novel draw solutes in forward osmosis for water reuse. **Industrial and Engineering Chemistry Research**, v. 49, n. 12, p. 5869–5876, 2010.

- 151 Xuan, S.; Wang, Y.-X.J.; et al. Tuning the Grain Size and Particle Size of Superparamagnetic Fe₃O₄ Microparticles. **Chemistry of Materials**, v. 21, n. 21, p. 5079–5087, 2009.
- 152 Rahimi, M.; Yousef, M.; et al. Formulation and Characterization of a Covalently Coated Magnetic Nanogel. **Journal of nanoscience and nanotechnology**, v. 9, n. 7, p. 4128–4134, 2009.
- 153 Ditsch, A.; Laibinis, P.E.; et al. Controlled clustering and enhanced stability of polymer-coated magnetic nanoparticles. **Langmuir**, v. 21, n. 13, p. 6006–6018, 2005.
- 154 Gu, F.L. and K.-X.L. and W.J. and X.-B.Z. and Y.W. and Z.-W. Facile synthesis of monodisperse superparamagnetic Fe₃O₄/PMMA composite nanospheres with high magnetization. **Nanotechnology**, v. 22, n. 22, p. 225604, 2011.
- 155 Gao, J.; Gu, H.; et al. Multifunctional Magnetic Nanoparticles: Design, Synthesis, and Biomedical Applications. **Accounts of Chemical Research**, v. 42, n. 8, p. 1097–1107, 2009.
- 156 Hunter, R.J. **Zeta potential in colloid science: principles and applications**. Academic press, 2013.
- 157 Li, W.; Tutton, S.; et al. First-pass contrast-enhanced magnetic resonance angiography in humans using ferumoxytol, a novel ultrasmall superparamagnetic iron oxide (USPIO)-based blood pool agent. **Journal of Magnetic Resonance Imaging**, v. 21, n. 1, p. 46–52, 2005.
- 158 Simon, G.H.; Bauer, J.; et al. T1 and T2 relaxivity of intracellular and extracellular USPIO at 1.5T and 3T clinical MR scanning. **European Radiology**, v. 16, n. 3, p. 738–745, 2006.
- 159 Wang, J.; Zhang, B.; et al. One-pot synthesis of water-soluble superparamagnetic iron oxide nanoparticles and their MRI contrast effects in the mouse brains. **Materials Science and Engineering: C**, v. 48, p. 416–423, 2015.
- 160 Xu, F.; Cheng, C.; et al. Superparamagnetic magnetite nanocrystal clusters: a sensitive tool for MR cellular imaging. **Nanotechnology**, v. 20, n. 40, p. 405102, 2009.
- 161 Wang, C.; Ravi, S.; et al. Dual-purpose magnetic micelles for MRI and gene delivery. **Journal of Controlled Release**, v. 163, n. 1, p. 82–92, 2012.
- 162 Saraswathy, A.; Nazeer, S.S.; et al. Citrate coated iron oxide nanoparticles with enhanced relaxivity for in vivo magnetic resonance imaging of liver fibrosis. **Colloids and surfaces. B, Biointerfaces**, v. 117C, p. 216–224, 2014.
- 163 Srivastava, S.; Awasthi, R.; et al. Innovative synthesis of citrate-coated superparamagnetic Fe₃O₄ nanoparticles and its preliminary applications. **Journal of Colloid and Interface Science**, v. 359, n. 1, p. 104–111, 2011.
- 164 Wang, Z.; Zhao, L.; et al. Water-soluble amorphous iron oxide nanoparticles synthesized by a quickly pestling and nontoxic method at room temperature as MRI contrast agents. **Chemical Engineering Journal**, v. 235, p. 231–235, 2014.
- 165 Jedlovszky-Hajdú, A.; Tombácz, E.; et al. Carboxylated magnetic nanoparticles as MRI contrast agents: Relaxation measurements at different field strengths. **Journal of Magnetism**

and Magnetic Materials, v. 324, n. 19, p. 3173–3180, 2012.

166 Ereath Beeran, A.; Nazeer, S.S.; et al. An aqueous method for the controlled manganese (Mn^{2+}) substitution in superparamagnetic iron oxide nanoparticles for contrast enhancement in MRI. **Physical Chemistry Chemical Physics**, v. 17, n. 6, p. 4609–4619, 2015.

167 Yang, G.; He, F.; et al. A cheap and facile route to synthesize monodisperse magnetic nanocrystals and their application as MRI agents. **Dalton Trans**, v. 44, n. 1, p. 247–253, 2015.

168 Song, M.; Zhang, Y.; et al. Influence of morphology and surface exchange reaction on magnetic properties of monodisperse magnetite nanoparticles. **Colloids and Surfaces A: Physicochemical and Engineering Aspects**, v. 408, p. 114–121, 2012.

169 Smolensky, E.D.; Park, H.-Y.E.; et al. Surface functionalization of magnetic iron oxide nanoparticles for MRI applications - effect of anchoring group and ligand exchange protocol. **Contrast media & molecular imaging**, v. 6, n. 4, p. 189–99,

170 Gupta, J.; Mohapatra, J.; et al. A pH-responsive folate conjugated magnetic nanoparticle for targeted chemo-thermal therapy and MRI diagnosis. **Dalton Transactions**, v. 45, n. 6, p. 2454–2461, 2016.

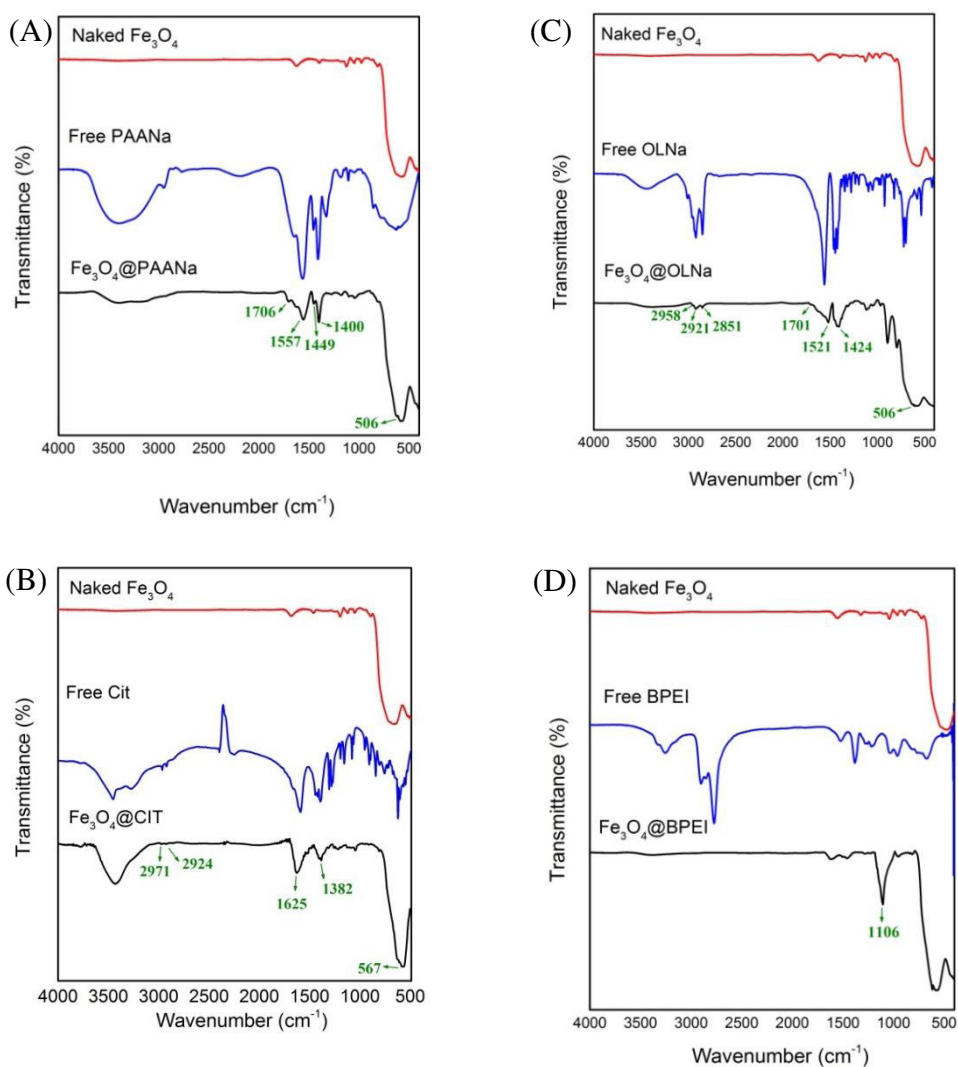
171 Santra, S.; Kaittanis, C.; et al. Drug/dye-loaded, multifunctional iron oxide nanoparticles for combined targeted cancer therapy and dual optical/magnetic resonance imaging. **Small (Weinheim an der Bergstrasse, Germany)**, v. 5, n. 16, p. 1862–8, 2009.

172 Huang, C.-C.; Chuang, K.-Y.; et al. Size-control synthesis of structure deficient truncated octahedral $Fe_3-\delta O_4$ nanoparticles: high magnetization magnetites as effective hepatic contrast agents. **Journal of Materials Chemistry**, v. 21, n. 20, p. 7472, 2011.

173 Duan, H.; Kuang, M.; et al. Reexamining the effects of particle size and surface chemistry on the magnetic properties of iron oxide nanocrystals: New insights into spin disorder and proton relaxivity. **Journal of Physical Chemistry C**, v. 112, p. 8127–8131, 2008.

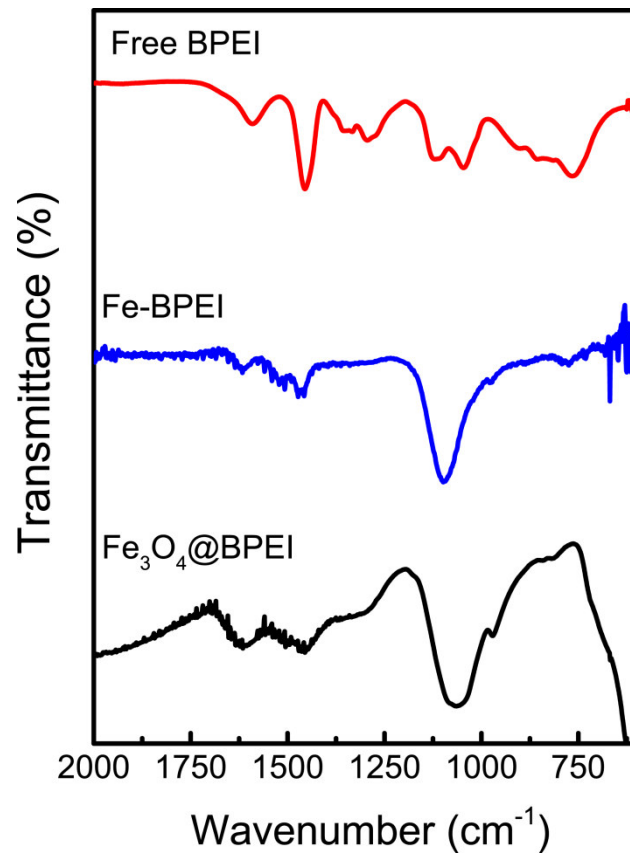
Appendix 1

Wide wavenumber range FT-IR spectra of the samples (A) Fe_3O_4 @PAANa, (B) Fe_3O_4 @CIT, (C) Fe_3O_4 @OLNa and (D) Fe_3O_4 @BPEI. For each sample there is a spectra of the non-functionalized Fe_3O_4 NPs, free capping agent and the functionalized NPs.



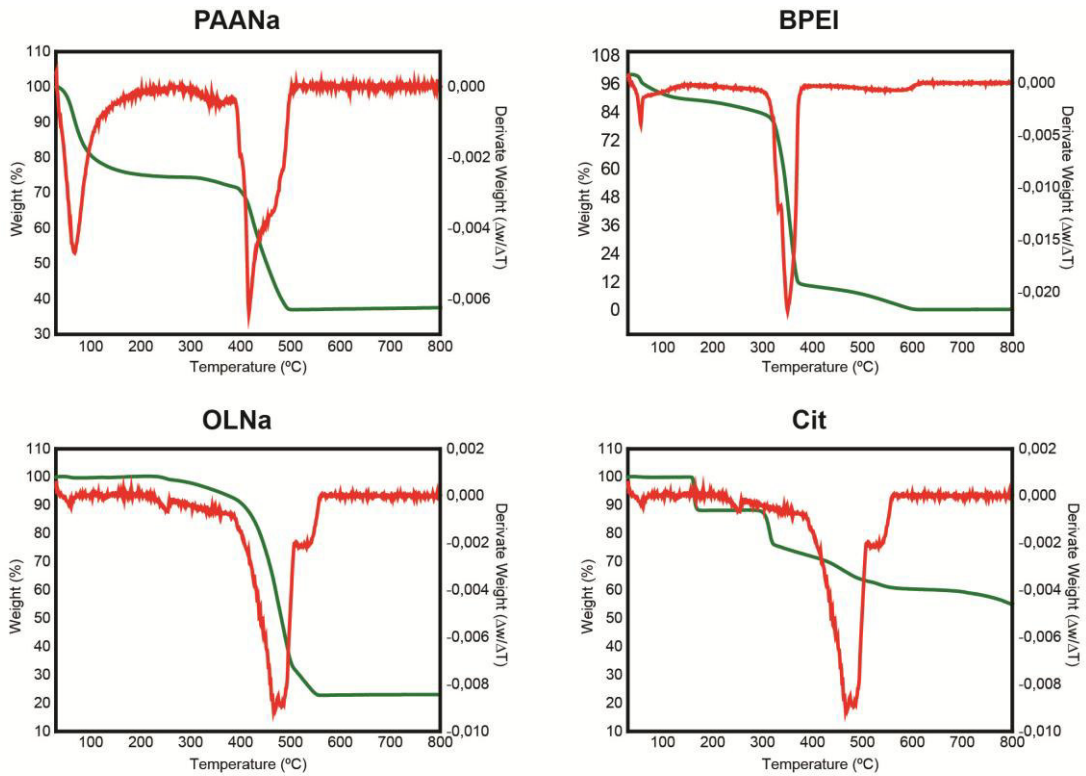
Appendix 2

FT-IR spectra of the free BPEI, the mixture of Fe^{2+} and Fe^{3+} cations with BPEI and the functionalized NPs of Fe_3O_4 with BPEI.



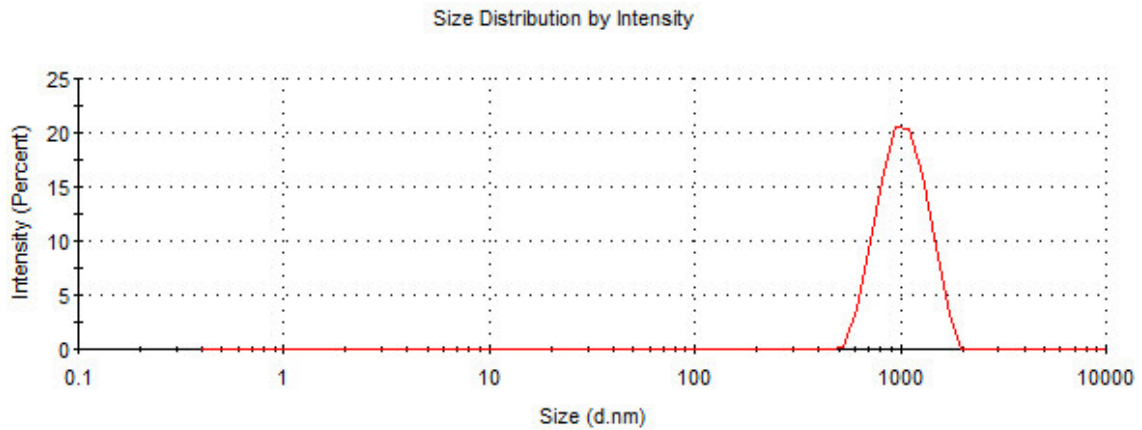
Appendix 3

TG and DTG curves for the free capping agents.



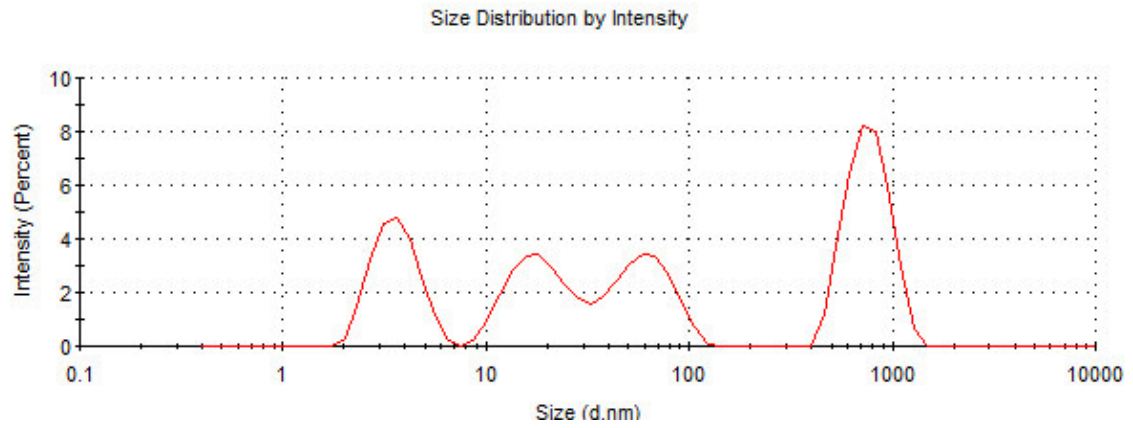
Appendix 4

Size distribution by intensity of PAANa aqueous solution.



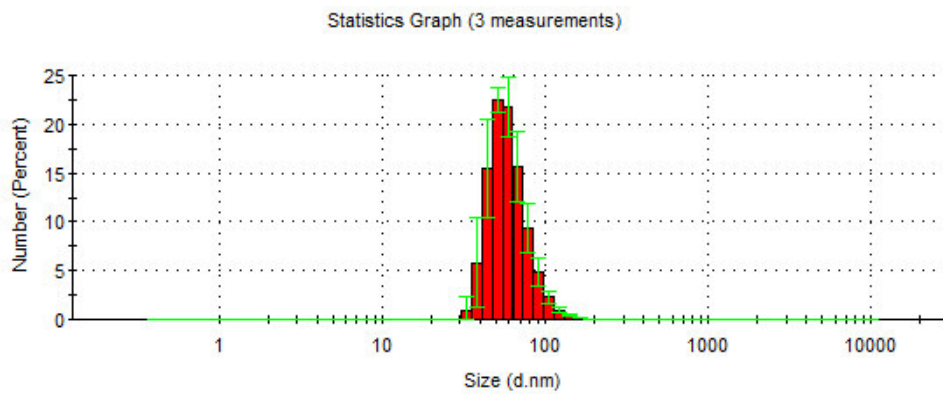
Appendix 5

Size distribution by intensity of BPEI aqueous solution



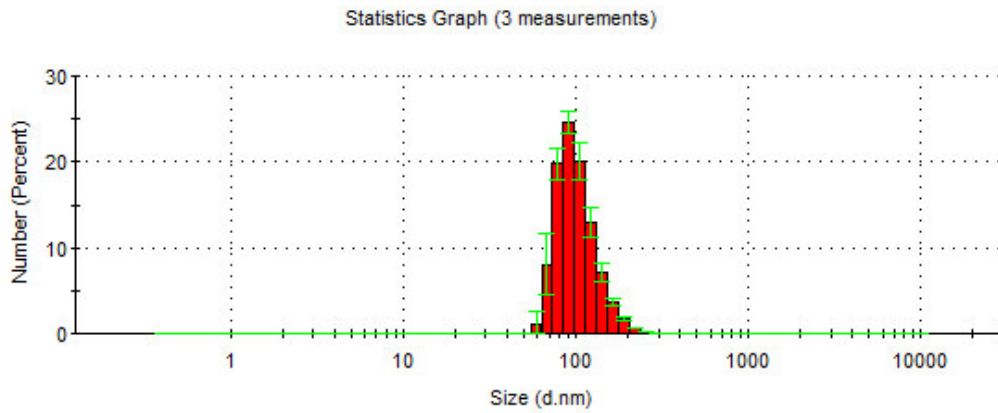
Appendix 6

Distribution size curve of DLS measurements for the sample $\text{Fe}_3\text{O}_4@PAANa$ in water.



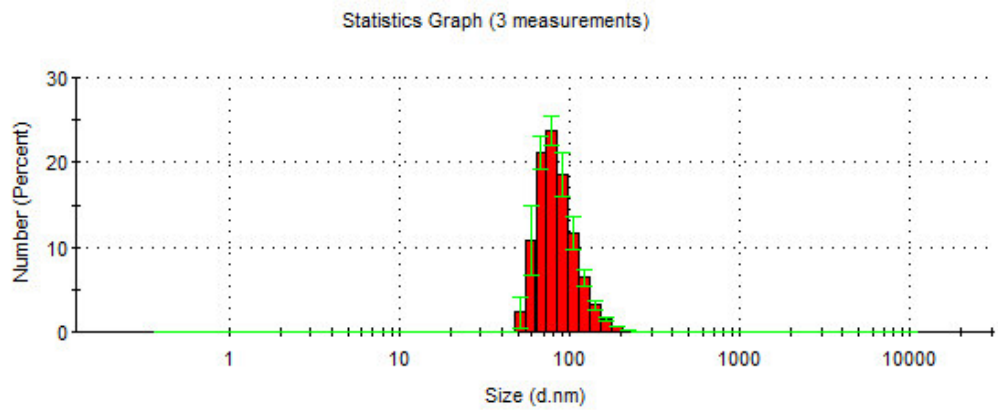
Appendix 7

Distribution size curve of DLS measurements for the sample $\text{Fe}_3\text{O}_4@\text{BPEI}$ in water.



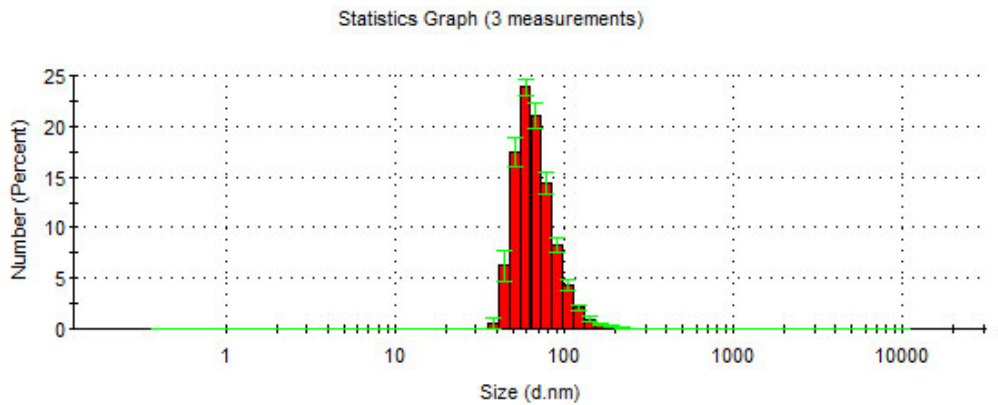
Appendix 8

Distribution size curve of DLS measurements for the sample $\text{Fe}_3\text{O}_4@\text{PAANa}$ in PB.



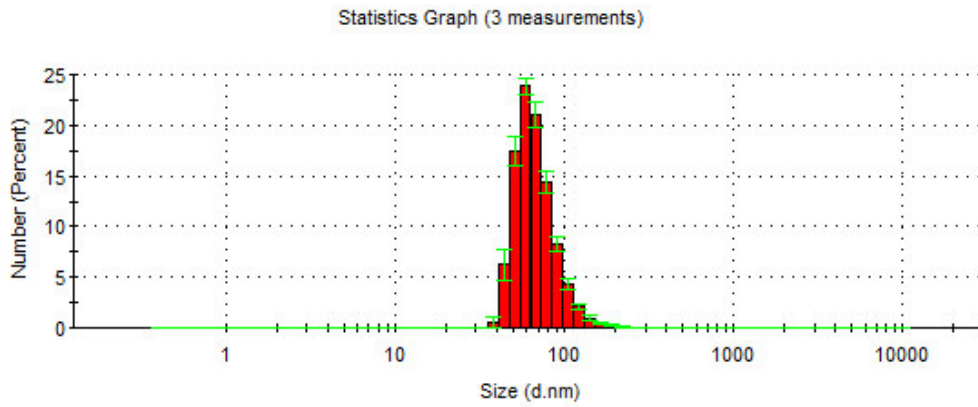
Appendix 9

Distribution size curve of DLS measurements for the sample $\text{Fe}_3\text{O}_4@\text{PAANa}$ in PBS



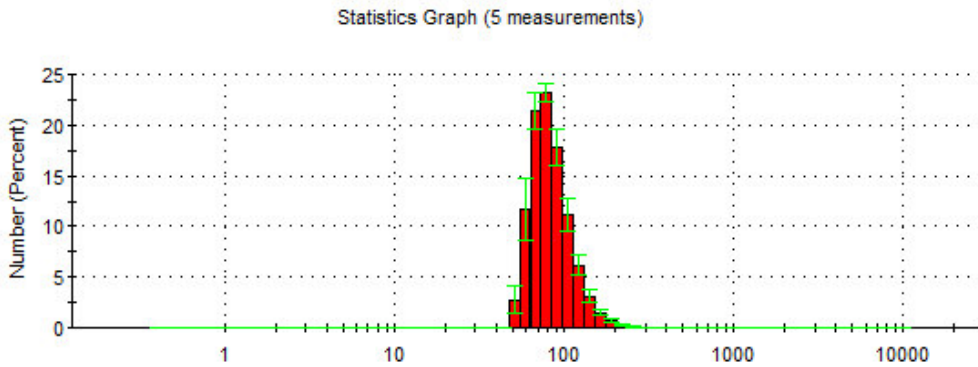
Appendix 10

Distribution size curve of DLS measurements for the sample Fe₃O₄@PAANa in PBS



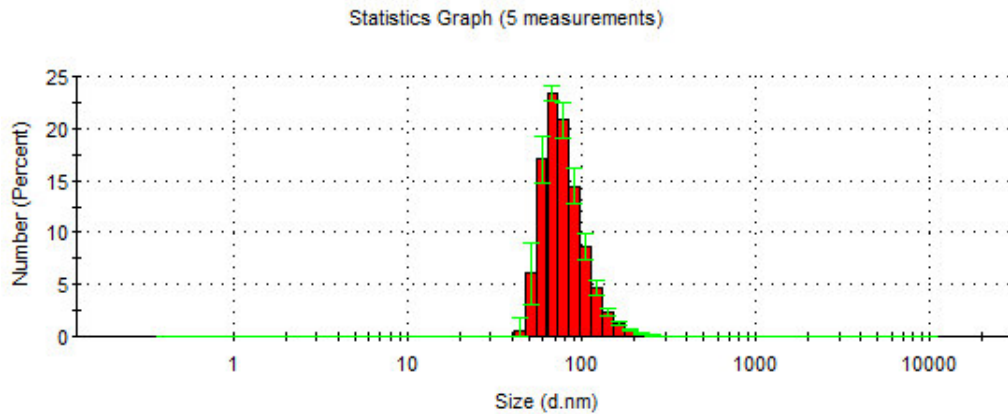
Appendix 11

Distribution size curve of DLS measurements for the sample Fe₃O₄@CIT in water



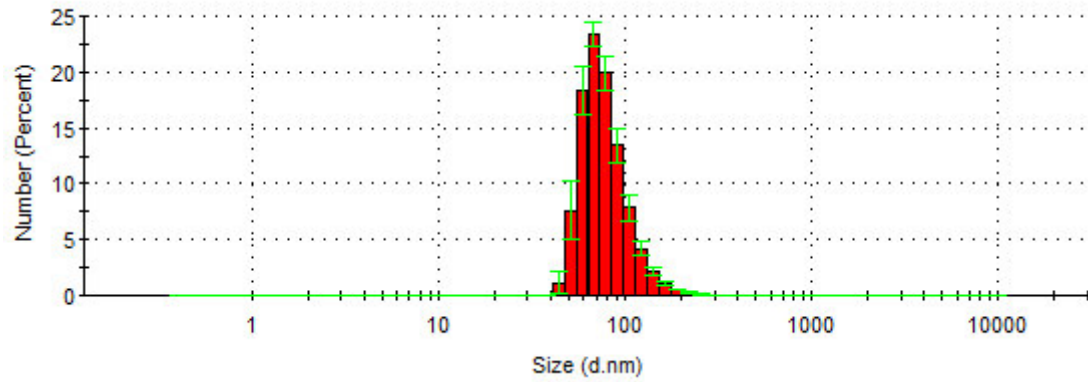
Appendix 12

Distribution size curve of DLS measurements for the sample Fe₃O₄@CIT in PBS



Appendix 13

Distribution size curve of DLS measurements for the sample $\text{Fe}_3\text{O}_4@\text{OLNa}$ in water



Appendix 14

Distribution size curve of DLS measurements for the sample $\text{Fe}_3\text{O}_4@\text{OLNa}$ in PBS

